Studies on ultrafast dynamics in correlated electron systems with time- and angle-resolved photoemission spectroscopy

Dissertation

zur Erlangung des Doktorgrades

an der Fakultät für Mathematik, Informatik und Naturwissenschaften

Fachbereich Physik

der Universität Hamburg

vorgelegt von

MICHAEL HEBER

HAMBURG

Januar 2024

Gutachter der Dissertation:	Prof. Dr. Kai Rossnagel Prof. Dr. Franz X. Kärtner
Zusammensetzung der Prüfungskommission:	Prof. Dr. Daniela Pfannkuche Prof. Dr. Kai Rossnagel Prof. Dr. Franz X. Kärtner Prof. Dr. Markus Gühr Dr. Michael Martins
Vorsitzende der Prüfungskommission:	Prof. Dr. Daniela Pfannkuche
Datum der Disputation:	25.06.2024
Vorsitzender des Fach-Promotionsausschusses Physik:	Prof. Dr. Markus Drescher
Leiter des Fachbereichs Physik:	Prof. Dr. Wolfgang J. Parak
Dekan der Fakultät MIN:	Prof. Dr.-Ing. Norbert Ritter

Eidesstattliche Versicherung / Declaration on oath

Hiermit versichere ich an Eides statt, die vorliegende Dissertationsschrift selbst verfasst und keine anderen als die angegebenen Hilfsmittel und Quellen benutzt zu haben.

Die eingereichte schriftliche Fassung entspricht der auf dem elektronischen Speichermedium.

Die Dissertation wurde in der vorgelegten oder einer ähnlichen Form nicht schon einmal in einem früheren Promotionsverfahren angenommen oder als ungenügend beurteilt.

Hamburg, den 5.2.2024

Michael Heber

Zusammenfassung

Die winkelaufgelöste Photoemissionsspektroskopie (ARPES) ist eine effektive Methode zur Untersuchung der elektronischen Bandstruktur von kondensierter Materie. Durch die Pump-Probe-Technik kann ARPES um eine zeitliche Komponente erweitert werden, wodurch die Elektronendynamik auf einer Femtosekunden-Zeitskala beobachtet werden kann. Laserquellen für hohe Harmonische (HHG) und Freie-Elektronen-Laser (FEL) erzeugen extrem ultraviolette (EUV) oder Röntgenpulse mit einer zeitlichen Breite von 100 fs oder weniger. Bei der Erzeugung hoher Harmonischer wird sichtbare oder infrarote Laserstrahlung in EUV umgewandelt, während beim FEL relativistische Elektronen in einem alternierenden magnetischen Feld kohärente Synchrotronstrahlung emittieren. FLASH (Free electron LASer Hamburg) ist ein FEL mit hoher Pulswiederholrate, welcher Photonenenergien bis in den weichen Röntgenbereich liefert. Für zeitaufgelöste (tr-) ARPES-Messungen sind Elektronenspektrometer mit hoher Detektionseffizienz unerlässlich, da die Wiederholrate der Pump- und Probequelle oft einschränkend wirkt. Hierfür sind daher Flugzeit-Photoelektronenspektrometer mit einem 3D-Detektionsschema am besten geeignet. Das Weitwinkel-Photoelektronenspektrometer WESPE und das Impulsmikroskop HEXTOF basieren auf der Flugzeittechnik und wurden speziell für die PG2-Beamline bei FLASH entwickelt. Diese Arbeit präsentiert zeitaufgelöste Untersuchungen von drei unterschiedlichen Quantenmaterialien.

Das HEXTOF Impulsmikroskop wird häufig in Verbindung mit einer HHG-Quelle eingesetzt. In der ersten wissenschaftlichen Anwendung dieser Arbeit wird eine Monolage Graphen auf Iridium(111) untersucht, um das Potenzial dieses Versuchsaufbaus im HHG-Labor abzuschätzen. Dabei konnte eine Zeitauflösung von unter 100 fs erzielt werden und das Detektorbild deckt im reziproken Raum mehr als die erste Brillouin-Zone ab. Die multispektrale Natur des HHG-Spektrums ermöglicht die Messung von k_z-abhängigen ARPES-Signalen, welche zur Rekonstruktion eines Tomogramms der Fermi-Oberfläche von Iridium verwendet wurden.

Der Dirac-Kegel ist nicht ausschließlich ein Merkmal von Graphen, sondern tritt auch als charakteristisches Merkmal des Oberflächenzustands von topologischen Isolatoren auf, welche in einem weiteren Kapitel untersucht werden. Obwohl topologische Isolatoren in der Tiefe des Materials nicht elektrisch leitfähig sind, verfügen sie an der Oberfläche über einen faszinierenden leitenden topologischen Zustand. Mit Hilfe des HEXTOF-Aufbaus haben wir den topologischen Isolator Bismutselenid (Bi_2Se_3) untersucht und tr-ARPES-Daten sowohl für den topologischen Oberflächenzustand als auch für die Rumpfniveaus Bi 4*d* und Se 3*d* aufgezeichnet. Ziel unserer Studie war es, die

Elektronendynamik bei hohem Pumpfluss innerhalb des topologischen Oberflächenzustands zu erforschen und die Robustheit des Zustands selbst zu untersuchen. Unsere Experimente haben gezeigt, dass der topologische Oberflächenzustand selbst bei hohen Pumpflüssen, die zu einer Oberflächenablation führen, intakt bleibt und seine Dynamik ihre Eigenschaften beibehält.

Die letzte Experimentreihe in dieser Arbeit beschäftigt sich mit einem schweren fermionischen System, bei dem $4f$- und $5f$-Elektronen mit Leitungsbandelektronen wechselwirken und Quasiteilchen in der Bandstruktur bilden. Thuliumselenied (TmSe) ist ein schweres Fermionensystem mit „mixed-valence“ Charakter der Tm-Ionen. Die Tm-$4f$-Elektronen hybridisieren mit den Elektronen im Leitungsband, was zur Bildung eines Multipletts im PES-Spektrum nahe des Ferminiveaus führt. Wenn TmSe mit Tellur dotiert wird, dehnt sich das Gitter aus, was einen Übergang vom „mixed-valence“ Zustand zu einem überwiegend divalenten Zustand bewirkt. Die Dynamik des $^3H_6$-Multiplett Peaks zeigt eine Abhängigkeit von der Te-Konzentration. Im „mixed-valence“ Zustand wird eine verzögerte, langanhaltende Dynamik beobachtet.

Diese Arbeit demonstriert nicht nur, wie vielseitig und leistungsfähig tr-ARPES für die Erforschung von Quantenmaterie im Allgemeinen ist, sondern zeigt auch explizit, dass die jüngsten Entwicklungen in der Impulsmikroskopie-Instrumentierung eine breite Palette von Anforderungen erfüllen können und den Weg zu einem „one fits all“-Design ebnen, das neben der Zeit- und Winkel- auch die Spin-Auflösung umfasst.

Abstract

Angle-resolved photoemission spectroscopy (ARPES) is a potent technique for studying the electronic band structure of condensed matter. The use of the pump-probe technique extends ARPES into the time domain, allowing the electron dynamics to be observed on an ultrafast timescale. High harmonic generation (HHG) sources and free electron lasers (FELs) generate extreme ultraviolet (EUV) or X-ray pulses that have a temporal width of 100 fs or less. HHG converts optical or infrared laser radiation into the EUV, whereas in the FEL, relativistic electrons emit coherent synchrotron radiation in an alternating magnetic field. The FEL FLASH (Free electron LASer Hamburg) is a high-repetition-rate FEL that extends the photon energy into the soft X-ray range. Electron spectrometers with high detection efficiency are essential because the repetition rate of the pump and probe source frequently constrains time-resolved (tr-)ARPES measurements. Therefore, time-of-flight photoelectron spectrometers with a 3D detection scheme are best suited for this purpose. The tr-ARPES setups, the wide-angle photoelectron spectrometer WESPE and the momentum microscope HEXTOF, are based on the time-of-flight technique and designed for the plane grating beamline PG2 at FLASH. In this thesis I present the time resolved studies on three different quantum materials.

Frequently, the momentum microscope is also paired with a HHG source. In the first scientific application of this thesis, a sample of pristine graphene on iridium(111) is investigated to evaluate the potential of this laboratory-based experimental setup. The results demonstrate a sub-100 fs time resolution and a field of view larger than the first Brillouin zone. The multispectral nature of the HHG spectrum enables measurement of k_z-dependent ARPES signal which were used to reconstruct a tomogram of the Fermi surface of iridium.

The Dirac cone is not a unique feature of Graphene. It also appears as a characteristic feature of the surface state of topological insulators, which were investigated in the second experiment chapter. Despite being insulating in the bulk, topological insulators possess an intriguing conducting topological state at the surface. The topological insulator bismuth selenide (Bi_2Se_3) was investigated using the HEXTOF setup. Tr-ARPES data was obtained for the topological surface state, and tr-XPS data was obtained for the Bi 4*d* and Se 3*d* core levels. Our study aimed to explore the electron dynamics at high pump fluences within the topological surface state, as well as to examine the robustness of the state itself. Even at fluences that result in surface ablation, our experiments have demonstrated that the topological surface state remains intact, and its dynamics maintain their characteristics.

The last scientific case in this thesis deals with a heavy fermionic system, where $4f$ and $5f$ electrons interact with conduction band electrons, forming quasi-particles in the band structure. Thulium selenide (TmSe) is a heavy fermionic system with mixed valence character on the Tm site. The Tm $4f$ electrons hybridize with the electrons in the conduction band, resulting in the formation of a heavy fermion multiplet in the PES spectra near the Fermi level. When TmSe is doped with tellurium, the lattice expands, causing a transition from the mixed valence state to a predominantly divalent state. The dynamics of the $^3H_6$ multiplet peak shows a dependence on the Te concentration. In the mixed valence state, a delayed long-lasting dynamic is observed.

This thesis not only demonstrates how versatile and powerful tr-ARPES is for the study of condensed/quantum matter in general, but also explicitly shows that recent developments in momentum microscope instrumentation can satisfy a wide range of needs, paving the way to a “one fits all”-design which includes besides time and angle also spin resolution.

Contents

1 Introduction

Quantum materials are a vast group of condensed matter whose macroscopic properties are primarily determined by the collective quantum mechanical behavior of their electrons. Their key features necessitate a complex quantum mechanical description and cannot be adequately modeled with a single-particle semiclassical approach. For instance, quantum materials include several classes of materials, such as superconductors, strongly correlated electronic systems, graphene, topological materials, or trivial ferromagnetic materials [1]. All of these characteristics leave their distinct fingerprint in the electronic band structure.

The standard method to determine the electronic structure of solid materials is angle-resolved photoemission spectroscopy (ARPES) [2–5]. Due to the photoelectric effect, materials that are illuminated with monochromatic ultraviolet or X-ray radiation will emit electrons. These photoelectrons are measured as a function of electron kinetic energy and emission angle, which can be translated into the two components of the surface-parallel momentum (k_x, k_y). With the information of the photon energy, also the perpendicular component k_z and the energy relative to the Fermi level $(E - E_\mathrm{F})$ of the electron inside the material before the photoexcitation can be determined [6]. The measured intensity distribution resembles a portion of the electronic structure in the four-dimensional energy-momentum space [7].

Band structures and Fermi surfaces, together with momentum-dependent band renormalization and lifetime effects, can be accessed directly [8–11]. Another intriguing application is orbital tomography, which allows for the reconstruction of real-space tomograms of molecular orbitals on crystal surfaces [12, 13]. The technique is known as ARPES or momentum microscopy, depending on whether emission angles or surface-parallel momentum components are imaged onto the detector [14–16]. The photoelectrons also carry spin information, and with a suitable detector, ARPES can access this information about the electronic structure.

The photon energy plays a crucial role in at least three different aspects in this energy-momentum imaging. Firstly, it determines the upper limit of detectable electron kinetic energy and three-dimensional (3D) momentum, thereby the volume of the probed portion in energy-momentum space [17]. Secondly, the surface-perpendicular momentum component k_z can be acquired by scanning of the photon energy, allowing for full 4D imaging of energy and momentum [7, 11, 18, 19]. Thirdly, the contrast of specific features in ARPES data can be improved by tuning the photon energy, using excitation resonances, variation in escape depth, or matrix-element effects [20, 21].

Another essential development of photoemission spectroscopy (PES) is time-resolved (tr-)ARPES or tr-momentum microscopy [22–24], in which time, or more precisely the time delay (t_{delay}) between femtosecond-scale pump and probe pulses, is added as a fifth measurement parameter. This technique evolved over the last two decades into a powerful ARPES modality to measure directly the dynamics of the excited electronic structure. It provides direct information on electronic dynamics at the fundamental time scales of electronic and atomic motion, especially on photoinduced transient changes of electronic states and their population [25–34].

tr-ARPES is now routinely performed with table-top laser sources and extreme ultraviolet (EUV) and X-ray free electron lasers (FELs). The laser sources make use of an up conversion of the photon energy by fourth harmonic generation in solids [35, 36] or higher harmonic generation (HHG) in gases [24, 37–51]. FELs generate the radiation by self-amplified spontaneous emission (SASE) of free electrons in undulators [22]. The corresponding probe photon energies of all of these sources for tr-ARPES range from the far UV to soft X-rays where a sweet spot currently is the intermediate EUV regime.

Due to the moderate repetition rate of most of the EUV sources time-of-flight (ToF) photoelectron spectrometers are beneficial. These spectrometers have a high transmission and detection efficiency which is necessary to reduce the measurement time for tr-ARPES. Two ToF based tr-ARPES setups were developed for use at the FEL FLASH (Free electron LASer Hamburg). Two setups are commonly used to measure dynamics in different energy levels. The first setup is used to measure core level dynamics, while the second setup, a momentum microscope, is mostly used to measure valence band dynamics. However, it can also measure atomic motion using core level photoelectron diffraction [22].

In this work we also demonstrate the capabilities of the momentum microscope in combination with a HHG source. For this purpose, a graphene layer on an iridium(111) crystal was investigated and the 3D Fermi surface of iridium was reconstructed. Graphene has a well-understood band structure in which electrons show a relativistic behavior at the K points of the Brillouin zone. The linear dispersion relation of the π-bands creates the characteristic Dirac cone at these points. We use the sample to determine the momentum, energy and time resolution.

Using the momentum microscope, we also studied the Dirac cone of the surface state of bismuth selenide (Bi_2Se_3), a topological insulator. Topological materials have a nontrivial band topology that generates and preserves the unique characteristics of the materials. The most commonly known subgroup is that of topological insulators. These insulators have a band gap similar to that of ordinary insulators, but due to strong spin-orbit coupling, some bands are inverted at the Fermi level. This results in a gapless Dirac surface state, which is protected by time-reversal symmetry and has a spin texture. Topological materials are considered to be a crucial element in unlocking the potential of quantum computing and spintronics [52, 53]. One of the prototypical 3D

topological insulators is Bi_2Se_3. Since only the surface of Bi_2Se_3 is conducting, excited electrons from the bulk and the surface exhibit dynamics on different time scales [54]. This work focuses on the dynamics induced by high fluences up to several $\frac{\mathrm{mJ}}{\mathrm{cm}^2}$ and the robustness of the surface state.

Another class of materials which is rich in unique electronic features are heavy-fermion materials. Heavy fermion materials are strongly correlated electronic systems with $4f$ and $5f$ electrons of rare-earth or actinide ions in a metallic surrounding. The f-electrons carry a magnetic moment. Due to the hybridization of the strongly localized f-electrons with the conduction band, heavy quasiparticles are formed. This leads, for example, to the Kondo effect, where the resistivity increases at low temperatures due to the scattering of the electrons at the magnetic impurities in the metal. In mixed-valence systems, the impurity ion shows the presence of two valences simultaneously. Recent research on a mixed-valence system focuses on the formation of exotic quasiparticles that are neutrally charged [55–59]. These mixed-valence systems require no superconducting state to form Majorana fermion quasiparticles [59]. Our tr-PES studies of the mixed-valence system thulium selenide (TmSe) focus on the dynamics of the Tm $4f$ electrons, which show a characteristic temporal evolution on a few picosecond time scale.

2 Photoemission spectroscopy and instrumentation

In this chapter I will give a brief introduction to tr-ARPES and the experimental instrumentation used in this thesis. PES is a well-established method for determining the electronic structure of solids, molecules and interfaces [2–5]. By combining PES with ultrafast light sources, dynamic processes in the electronic structure on an ultrafast (femtosecond) time scale can be investigated.

2.1 Photoemission spectroscopy

The basic principle of PES is the photoelectric effect, where a bound electron is excited into the continuum by absorbing a photon. The photoelectric effect was discovered by Hertz [60] and quantum mechanically described by Einstein [61]. PES methods exploit the fact that the kinetic energy E_{kin} of the emitted electron is determined by the photon energy $h\nu$, the binding energy of the electron E_{bind} and the work function Φ, which is defined as the difference between the Fermi level E_F and the vacuum level E_{vac}:

$$E_{kin} = h\nu - E_{bind} - \Phi. \tag{2.1}$$

A photon is probing the density of states by exciting a bound electron into the continuum, following Fermi's golden rule [5]. The transition probability w_{fi} is given by

$$w_{fi} = \frac{2\pi}{\hbar} \left| \left\langle \Psi_f^N \left| H_{int} \right| \Psi_i^N \right\rangle \right|^2 \delta \left(E_f^N - E_i^N - h\nu \right), \tag{2.2}$$

where Ψ_i^N and Ψ_f^N are the N-electron initial state and final state with the respective energies $E_i^N = E_i^{N-1} - E_{bind}$ and $E_f^N = E_f^{N-1} - E_{kin}$. The Hamilton operator can be approximated by the single photon interaction Hamiltonian $H_{int} = \frac{e}{2mc}\mathbf{Ap}$, where $\mathbf{p}$ is the electronic momentum operator, and $\mathbf{A}$ is the electromagnetic vector potential. For an excitation energy $h\nu < 1000\,\text{eV}$, PES is a surface sensitive method with a typical probing depth of about 2 nm in solids. The surface sensitivity is a result of the limited inelastic mean free path of the electrons in solids [62, 63]. Inelastically scattered electrons will contribute to the background of the spectrum. Detailed descriptions of PES can be found in Ref. [2] and Ref. [64].

In the scope of this work, we will focus on experiments with condensed matter samples probed with EUV and soft X-ray radiation.

2.1.1 Angle-resolved photoemission spectroscopy

If besides the kinetic energy also the emission angle of the photoelectron shall be measured, the technique is called ARPES. The two momentum components k_x and k_y parallel to the surface are conserved. The absolute value of the parallel momentum $k_{||}$ is directly related to the emission angle θ of the emitted photoelectron by

$$k_{||} = \sqrt{k_x^2 + k_y^2} = \sqrt{\frac{2mE_{kin}}{\hbar^2}} sin(\theta). \tag{2.3}$$

The energetic scheme of ARPES is illustrated in Figure 2.1, where an electron from the valence band is excited into the continuum and then recorded by the detector. Core level electrons usually have no energy dispersion, but due to scattering of the photoelectrons at the atoms in the sample, the intensity can vary as a function of parallel momentum [65, 66]. For a given kinetic energy the momentum is limited $k_{||,max} = \sqrt{\frac{2mE_{kin}}{\hbar^2}}$, resulting in a so-called event horizon.

Due to the broken translation symmetry at the surface, the perpendicular momentum $k_\perp$ is not conserved. However, in the nearly free electron approximation [67, 68], it is possible to approximate the perpendicular momentum $k_\perp$ [6]:

$$k_\perp = |\mathbf{k}_z| = \sqrt{\frac{2m^*}{\hbar^2}\left[E_{kin} + V_0^*\right] - k_{||}^2} = \sqrt{\frac{2m}{\hbar^2}\left[(E - E_\mathrm{F}) + h\nu + V_0\right] - \left(k_x^2 + k_y^2\right)}, \tag{2.4}$$

where V_0 is a constant, called the inner potential. If the inner potential is unknown, it can be determined with photon energy-dependent measurements. Hereby, one increases the photon energy to map the perpendicular momentum component $k_\perp$. When symmetry points of the Brillouin zone are found, the inner potential V_0 can be calculated back from their relative positions.

There are two common designs of electron spectrometers used in ARPES experiments, one using the hemispherical analyzer and the other based on the ToF spectrometer. Both will be discussed in more detail in Section 2.3.

2.1.2 Ultrafast time-resolved photoemission spectroscopy

tr-ARPES extends conventional ARPES into the time domain and allows us to get unique insights into the non-equilibrium properties of materials by tracking the spectral evolution of core levels and the valance band structure in time. Such electronic dynamics happen usually on the time scale of sub-femtoseconds to several picoseconds and can be resolved by performing ARPES in a pump-probe scheme.

A schematic illustration of a pump-probe experiment is shown in Figure 2.2. A pump pulse with a wavelength in the optical or infrared regime excites the electronic structure of the sample. The excited electronic density of states is then probed with a second

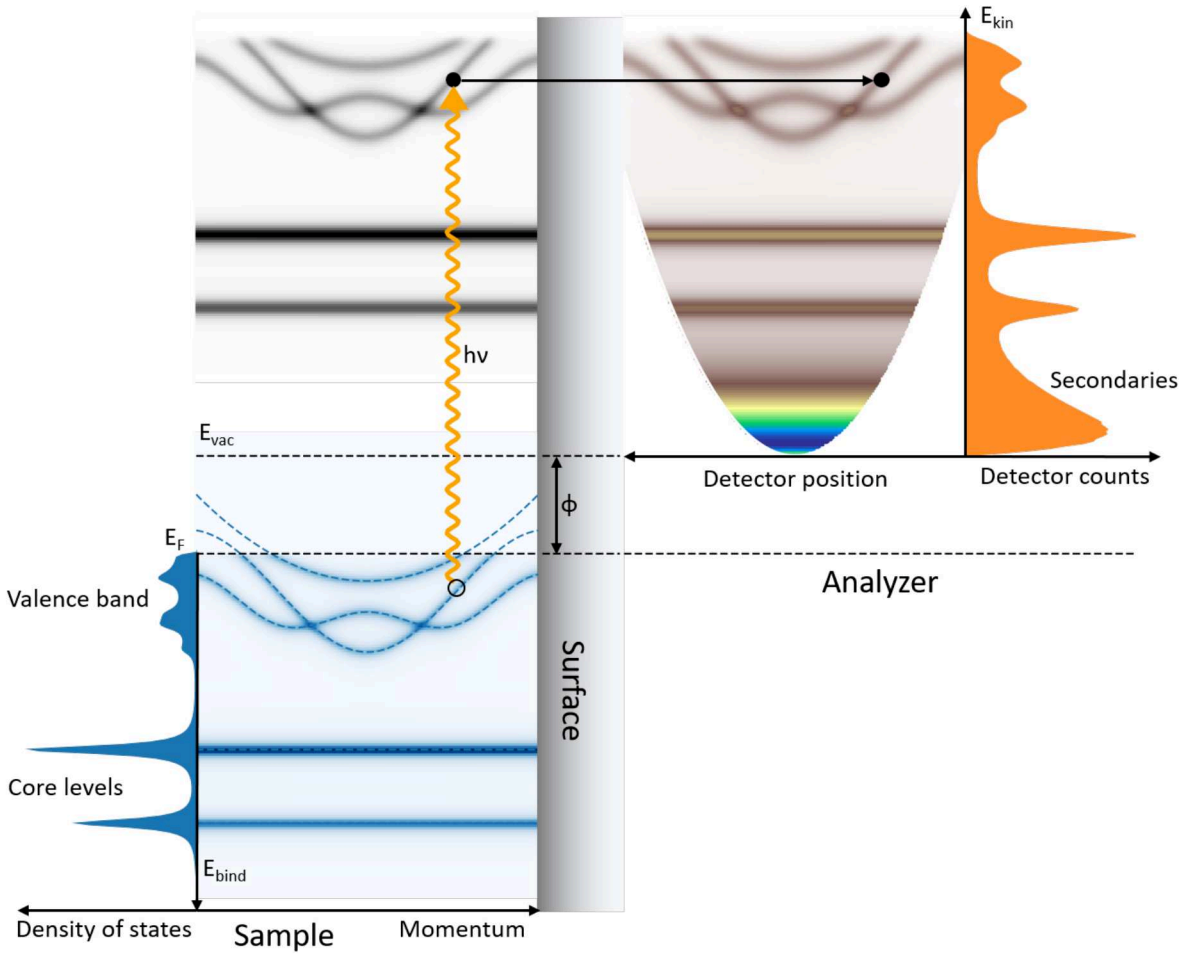

Figure 2.1: Energy scheme of photoelectron emission. Left half: The electronic states of the sample are depicted as a function of binding energy E_{bind} and the surface-parallel electron momentum. An electron from the valence band is excited into the continuum by a photon with the energy $h\nu$. Right half: The photoelectron is detected with the PES analyzer. Because energy and momentum are conserved, the initial binding energy and momentum of the electron can be recovered from the kinetic energy and the position on the detector. The inelastically scattered electrons will appear in the detector spectrum as a secondary background.

pulse with usually much higher photon energy, going towards the EUV and soft X-ray regime. By varying the delay time between the two pulses the relaxation dynamics can be recorded. It is important that the excited state relaxes back into the initial state before the next pump pulse excites the sample again. Thus, the relaxation time must be much faster than the time between two pump pulses.

The temporal length of both the pump and probe pulse has to be short enough to obtain an adequate time resolution. The typical temporal full width at half maximum (FWHM) in this work is in the range of 60 to 120 fs for each pulse. It can by assumed that there is no phase correlation between both pulses. Because several million pairs of pump-probe pulses are needed to acquire a spectrum in a good quality, the temporal jitter between the pulses will influence the time resolution too. The cause of jitter can be manifold, including synchronization issues, differences in path length due to thermal expansion, or imprecision in the delay stage. Thus, the overall time resolution is given by

$$\delta t = \sqrt{t_{pump}^2 + t_{probe}^2 + t_{jitter}^2}, \tag{2.5}$$

where t_{pump} and t_{probe} are the pulse length of the pump and the probe pulse, respectively, and t_{jitter} is the temporal jitter between both sources.

In a pump-probe experiment, multiple types of excitation are possible. Probably the most obvious transition is a direct optical excitation of electrons into unoccupied states, but also transitions via one or several intermediate states are possible. For pumping with visible or infrared light, usually only valence band electrons can be directly excited to unoccupied states. These excited electrons together with their holes can be described as primary hot carriers. As the primary hot carriers decay, they can also excite secondary hot carriers, which increases the total number of excited electrons but not the total energy. The energy distribution will quickly establish a Fermi-Dirac distribution again, but at much higher temperatures. Afterwards, the energy dissipates into other subsystems, such as phonons or spins, until each subsystem is thermalized. In the end, the heat is transferred into the bulk. The thermal capacity of the bulk can be assumed to be much larger than that of the pumped surface.

The photon energy of the pump pulse is typically lower than the work function of the sample. Direct exertion into the continuum is then only possible with a multi-photon process. This process is less likely than direct emission from the probe, but should not be neglected due to the typically high fluence of the pump pulse. In general, the electron emitted by a multi-photon process of the optical pump pulse are slow in comparison to most of the electrons emitted by the probe pulse.

2.1.3 Space-charge effects in photoemission spectroscopy

The high brightness of modern photon sources such as FELs can lead to unwanted space-charge effects in a PES experiment, limiting the energy and momentum reso-

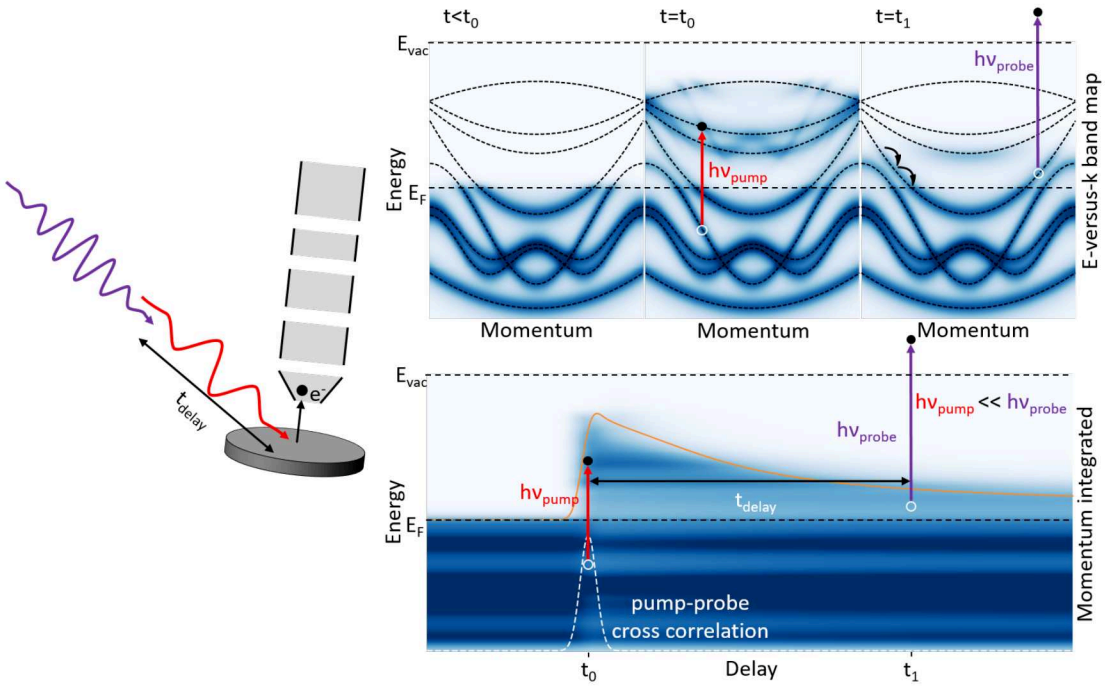

Figure 2.2: Left: Scheme of a pump-probe experiment setup with collinear pump and probe beams. Right: Illustration of the measured signal in a pump-probe experiment.The upper panels depict snapshots of the excited band structure in an energy-versus-momentum representation at different time steps. The bottom panel displays the same electronic-structure dynamics in a momentum-integrated energy-versus-delay representation. A pump pulse with photon energy $h\nu_{pump}$ at time t_0 excites a electron into unoccupied bands above the Fermi level E_F. The later arriving probe pulse with photon energy $h\nu_{probe}$ releases the excited electron into the continuum, which allows us to measure the excited electronic structure at the time t_1. The dynamics in the electronic structure is mapped by varying the time delay t_{delay} between both pulses. The orange curve shows the occupation of states above E_F as a function of time. The pump-probe cross correlation, which is indicated by the white dashed Gaussian shaped line, represents the time resolution of the experiment.

lution. Due to the high electron density of emitted electrons, the Coulomb repulsion between electrons cannot be neglected anymore. The bunch of emitted electrons will create an electric field, which is acting back on the electrons and modifies their kinetic energy and their momentum. This leads to shifts and broadening effects in the energy spectrum and smears out the momentum distribution [69, 70].

In general, all locations of high electron density are potential areas, where space-charge effects can occur. An obvious position of high electron density is close to the sample because the electrons are not yet dispersed by energy and the spot size on the sample is usually kept small to avoid aberrations of the electron optics. Space-charge can be a result of the high intensity of the EUV or X-ray probe pulse, but can also be introduced by the pump pulse.

The photocurrent increases as the photon energy rises due to the increase in the number of states that can be probed. As a consequence, also secondary processes like the Auger effect become more likely. Reducing then the intensity of the photon source to counter space-charge is always a tradeoff with the count rate on the detector. While the overall quantum efficiency increases with increasing photon energy, the cross section for a single electron state usually decreases. This is especially valid, if the focus of the measurement is on the fast electrons coming from lower bound states.

Because of the low photon energy, the pump pulse produces only slow electrons. A direct single photon excitation into the continuum is usually not possible because the photon energy $h\nu$ is lower than the work function Φ. However, a sufficiently high pump fluence can generate a large number of photoelectrons through multi-photon processes. The average number of photons required to emit an electron depends on the work function and the pump wavelength. Except for extreme cases, these electrons are part of the low kinetic energy spectrum and so not detected with the spectrometer. The space-charge effects of the pump pulse are affected by the pump-probe delay. Especially at temporal overlap, the interaction between the electrons from both pulses can be strong [71, 72].

Furthermore, at focus positions of the electron optics the electron density is increased. This can cause strong Coulomb interaction between the electrons of the pump and the probe pulse. In this case, the pump pulse arrives at the sample before the probe pulse, so that the fast electrons from the probe pulse and the slow electrons from the pump pulse pass the focus position at the same time. This type of space-charge effects is highly dependent on the settings of the optical elements [73].

Due to non-linearity and complexity, space-charge effects cannot easily be disentangled from the data. To counter space-charge effects, the intensity of the pump and the probe beam have to be reduced at least below the threshold where significant energy broadening begins to appear.

2.2 Extreme ultraviolet and soft X-ray radiation

A fundamental part of a PES experiment is the light source. The source should deliver monochromatic light and as can be seen from Equation 2.1, the photon energy must be suitable to emit a bound electron. The lower threshold of the photon energy is usually defined to overcome the work function with a single photon. As Equation 2.3 shows, the parallel momentum range increases with higher photon energies.

Electromagnetic radiation in the photon energy range between 10 to 121 eV is called extreme ultraviolet (EUV) and the range from 100 eV up to 5 keV soft X-ray. Many of the atomic resonances are located in this energy range. This leads to strong photon absorption in all types of condensed matter. The high cross section is beneficial for PES, but complicates the photon beam transport. Because no material is transparent the beam needs to be transported in vacuum and no transmission optics are available. Reflective optics are required, which are only effective under grazing incidence. Due to the strong absorption, their efficiency is still in the range of only 50%. To resolve dynamics much faster than the minimum detector exposure time ($\sim$1 µs), the pump-probe technique is required. Continuous and quasi-continuous sources like X-ray tubes and high repetition rate synchrotron storage rings are not suitable for this technique. For tr-PES the most common EUV sources are HHG sources [45], but also dedicated beamlines at synchrotron radiation sources, like storage rings with a special mode and FELs, are available.

2.2.1 Free-electron laser undulator radiation

Accelerated charged particles will emit electromagnetic radiation. In particle accelerators this behavior was experimentally observed for the first time in the 1940s [74]. The radiated power is at its maximum when the acceleration is perpendicular to the momentum of the charged particle. This implies that there is no energy gain or loss of the particle due to an external force, and the motion will be circular. Such a circular motion can be achieved with a homogeneous magnetic field of dipole magnets. For electrons the synchrotron radiation will be several orders of magnitude higher ($\sim (\frac{m_p}{m_e})^4 \approx 10^{13}$) than for protons or ions at the same kinetic energy. The emitted spectrum from a single dipole magnet is broad but strongly directed in the direction of electron movement due to the Lorentz transformation. Multiple electrons will radiate incoherently, so the intensity raises linearly with the number of electrons N_e [75].

To make better use of synchrotron radiation, undulators, a structure of alternating dipole magnets, are installed in electron accelerators. Due to interference effects a few specific wavelengths are enhanced, generating the typical undulator spectrum. Those wavelengths correspond to the Lorentz contracted undulator period length λ_u and their harmonics with some phase slippage factor. Also, in the ultrarelativistic case the electron slips behind the synchrotron radiation because of the longer path of the wiggling

motion. The wavelength for the n^{th} harmonics is given by

$$\lambda = \frac{\lambda_u}{2n\gamma^2}\left(1+\frac{K^2}{2}+\gamma^2\theta^2\right); \qquad n = 1,2,3,\ldots, \tag{2.6}$$

with the undulator parameter $K = \frac{\lambda_u eB}{2\pi m_0 \beta c}$, Lorentz factors β and γ and the emission angle θ. The bandwidth of each harmonic scales inversely with the number of periods n ($\frac{\delta\lambda}{\lambda} = \frac{1}{n}$) and the peak intensity of each harmonic scales quadratically.

Up to now we discussed coherent radiation of one specific electron at the multiple dipoles of an undulator. In a FEL a relativistic electron beam exchanges energy with the co-propagating coherent photon beam [75, 76]. Therefore, the electron velocity $\vec{v_e}$ must have a nonzero component parallel to the electric filed $\vec{E}$ of the photon beam. The energy transfer dW is given by

$$dW = -e\vec{E}\cdot\vec{v_e}\,dt. \tag{2.7}$$

The dot product is not vanishing for the sinusoidal electron motion in an undulator. The radiated emission can be described as stimulated emission. Note that the dot product in Equation 2.7 can be negative depending on the phase between the electric field and the electron motion. Only odd harmonics of the undulator radiation will have a fixed phase relation at all undulator periods, which then results in an overall gain at this wavelength. The radiated power P depends quadratically on the number of electrons N_e,

$$P(\lambda) = P_1(\lambda)N_e + P_1(\lambda)N_e(N_e-1)g^2(\lambda), \tag{2.8}$$

where P_1 is the single electron radiation power and g a nonzero factor, which increases with smaller emittance of the electron beam.

To start the energy exchange between the electron and the radiation field, the latter must be already present. The first option is to seed with an external light source with matching wavelength. For example, this external source can be laser- or HHG-systems. Another method is SASE, where at the front section of the undulator shot noise from the undulator radiation is used to seed quadratic power gain in the subsequent section. Because of the onset of shot noise in the undulator radiation, each shot will amplify slightly different modes. This causes fluctuation in wavelength and intensity. The summed-up spectrum of several shots will resemble the broader undulator spectrum, while each single shot can have much sharper energy distribution.

Most of the existing synchrotron sources are storage rings, where undulators are installed serially in multiple sections and can be run in parallel with the same electron bunch. For each undulator a beamline transports the photons to one or more experiments. Because a high quality of the electron beam is required, linear electron accelerator designs are used for EUV and X-ray FELs. If multiple undulators are in use at a FEL they are installed in parallel. Simultaneous operation of two undulators is only possible by switching the electron beam multiple times per second back and forth, which reduces the effective repetition rate.

2.2.2 The plane grating monochromator beamline at FLASH

FLASH (Free electron LASer Hamburg) is a SASE FEL with high gain. It is the first high repetition rate EUV and soft X-ray FEL in operation [77]. With the monochromized plane grating beamline PG2 it fits best the requirements for ultrafast tr-ARPES. [1]

FLASH is operated in the burst mode. A burst, a train of electron bunches, is injected into the accelerator at a repetition rate of 10 Hz. Each burst consists of up to 500 electron bunches. The bunches are separated by at least 1 ms in time. There are two undulators, FLASH I and FLASH II, each with several beamlines and end stations. In parallel operation of FLASH I and II, the train can be split into two parts. The first part is usually guided into the FLASH I undulator and the last bunches of the train to FLASH II. Each bunch generates synchrotron radiation in the undulator. FLASH I has a fixed gap undulator, which does not allow for any changes of the magnetic field strength of the undulator. The photon energy of the synchrotron radiation can only be varied by changing the kinetic energy of the electrons, which is a rather complex task. Photon energies from 30 eV to 300 eV are available in the fundamental of the undulator spectrum. Higher harmonics of the undulator radiation extend the range further into the soft X-ray regime. The harmonics can be selected easily by the monochromator.

The photon beam is guided with grazing X-ray optics to the different end stations or ports. One of the beamlines at FLASH I is the plane grating beamline PG2, which is an open port beamline and has no permanently fixed end station. This beamline uses a plane grating monochromator with different grating options [78, 79]. If a high photon energy or a high energy resolution is not required, the grating with 200 lines per mm is usually used due to its higher transmission. The monochromator is beneficial to define the photon energy bandwidth better and suppress the influence of the SASE fluctuations. The monochromator also allows to select the 3^{rd} or even the 5^{th} harmonic of the FEL radiation.

To complete the capabilities of the PG2 beamline a near infrared (NIR) laser for pump-probe experiments is installed. This laser provides pulses with 800 nm wavelength in the same burst pattern as FLASH, but only up to 400 pulses in one burst [80]. The beam is coupled-in collinearly to the FEL beam. To up-convert the pump pulse to 400 nm wavelength, a barium borate crystal is used to generate the second harmonic. The pulse energy is measured for each pulse with a pickup mirror and a diode. The laser was recently replaced by a fiber laser setup with slightly different characteristics. This laser can provide more pulses to cover the full bunch train of FLASH, and the pulses are shorter at a wavelength of 1030 nm [81].

[1] With new instrumentation for the soft X-ray beamline at European XFEL and the high repetition rate upgrade of SLAC for the LCLS II project, further PES end stations are upcoming.

2.2.3 High harmonic generation

The high harmonic up-conversion of short laser pulses allows us to build coherent light sources in table-top design [82]. These sources provide radiation in the EUV and soft X-ray regime [83]. The up-conversion is a highly nonlinear process, which requires lasers with high intensity ($\sim 10^{14}\ \frac{\mathrm{W}}{\mathrm{cm}^2}$) and pulses shorter than a picosecond. A short-pulse laser beam with high intensity is focused into a gas target. The spectrum shows a characteristic series of emission lines, which have photon energies of the odd multiples of the driving laser. The even harmonics are forbidden by parity conservation [84]. The intensity of the emission peaks decreases rapidly for the first harmonics. For higher harmonics several peaks follow on the same intensity level in the so-called plateau region, which ends at high photon energies with a sharp cutoff. For the first time HHG was observed in a noble gas target in the late 1980s [85, 86]. The interaction of light with atoms changes drastically with increasing intensity. The HHG spectrum is determined by the frequency and intensity of the driving laser instead of by transitions of the atoms. HHG spectra are characterized by emission peaks at odd multiples of the fundamental laser frequency, as well as the cutoff and the intensity plateau of the higher harmonics near the cutoff. The discovery of HHG in the gas phase called for a new theoretical explanation. A first numerical study matched the cutoff position and the plateau shape well [87]. Later a quantum analytical theory of the HHG process was developed by Kunlander [84].

An intuitive description of HHG from a plasma physics point of view was given by Corkum [88]. In this semiclassical model, the HHG process is split into three steps:

1. Multi-photon ionization of an atom by a tunneling process,
2. Propulsion of the liberated electron in the laser field,
3. Recombination of the electron with its ion.

In the first step an electron is liberated from its parent atom. The ionization cannot be explained by the photoelectric effect because the photon energy of the laser is far below the ionization threshold.

The intense laser light can be described in a classical way with an electromagnetic field. The laser field is a coherent superposition of the electromagnetic wave of each photon and creates a ponderomotive potential U_p for a charged particle. For an electron this is: $U_p = (eE/2m\omega)^2$ with the electrical field amplitude of the laser E, the laser frequency ω, the elementary charge e, and the electron mass m.

For the ionization there is on the one hand the laser pulse with its field and on the other hand the atoms which should be ionized. For simplicity, we assume just one atom and describe this by a parent ion with an electron in its Coulomb potential. Putting both the laser and the atom together, the electron will see the laser field in addition to the Coulomb potential. Of course, the field will also affect the parent ion. However,

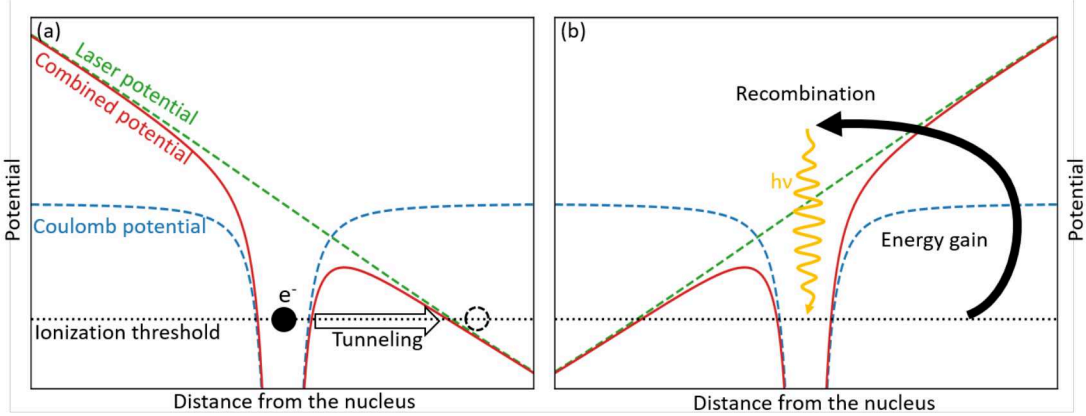

Figure 2.3: The effective potential (red), which the electron sees, is the superposition of the Coulomb potential (dashed blue) and the ponderomotive potential of the laser (dashed green). Left: At the particular laser phase, shown in the left plot, the electron sees a finite potential barrier on the right-hand side. Right: After half an oscillation period of the laser the slope of its potential is reversed and the picture is mirrored.

we can neglect the ponderomotive force acting on the ion since it is much heavier than the electron. Thus, the effective potential is the superposition of the Coulomb potential and that of the electric field of the laser (see Figure 2.3). Because the wavelength of the laser is much longer than the atom radius, the combined potential is more or less a skewed Coulomb potential modified by an extra slope which varies with time. The time dependency of the combined potential is much slower than the time for ionization. Therefore, the potential can be considered to be quasi-static during the ionization process. The electron sits on the ionization threshold level in the Coulomb dip of this quasi-static potential. For some phases of the laser the slope is steep enough to create a finite potential barrier on one side, as shown on the right side in Figure 2.3. For this quasi-static potential, the Schrödinger equation allows for a non-vanishing probability amplitude outside of the barrier. Thus, the electron can tunnel through this barrier with a certain probability and the atom is ionized.

In a classical picture, an electron outside of the Coulomb potential will be driven by the oscillating ponderomotive potential. Some electron trajectories return back to the nucleus, where a recombination is possible. The kinetic energy at recombination depends on the laser phase of ionization, with a maximum kinetic energy of $3.17\,U_p$. By recombination, photons can be emitted with the maximum possible energy of the sum of the ionization energy I_p and the maximal kinetic energy E_{kin} of the electron at the position of the nucleus [87, 89]:

$$h\nu_{max} = I_p + E_{kin,max} = I_p + 3.17U_p. \tag{2.9}$$

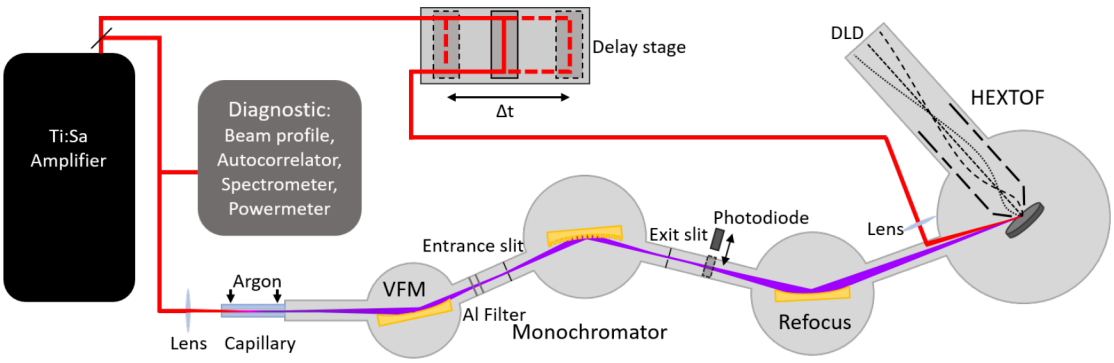

Figure 2.4: Schematic setup of the HHG source. The output of the Ti:Sa amplifier is split into two branches, the main and the pump branch. The main brunch is sent into the capillary where the EUV radiation is generated. The EUV radiation is transported with three grazing-incidence optics to the sample. The second EUV optic is the grating of the monochromator. The path length of the pump branch is adjustable to vary the delay between the pump and the probe pulse.

This maximal energy determines the cutoff of the spectra. This simplified picture does not explain the spectra fully [88]. Solving the time-dependent Schrödinger equation will show the harmonic character of the spectra.

2.2.4 The HHG light source

For laboratory-based measurements a HHG source was used with the momentum microscope. In this source, a NIR laser drives the HHG in a noble gas target. The radiation is focused into the microscope to emit photoelectrons. Figure 2.4 is a schematic depiction of the laboratory-based HHG source. In our case the setup is powered by a commercially available amplified titan sapphire laser from KMLabs: the Wyvern 1000. The amplifier provides ultrashort pulses with a wavelength of 790 nm at a repetition rate of 1 to 10 kHz. The pulses have a temporal length of about 50 fs and a pulse energy of up to 4.5 mJ. For the data obtained for this thesis, the setup was running at a repetition rate of 6 kHz. Its output is split into the main and the pump branch in a ratio of 3 to 1.

With only two transmissive optics, the main branch is optimized for short pulses. The NIR beam is guided into the capillary-based gas cell, a XUUS (eXtreme Ultraviolet Ultrafast Source) from KMLabs with slightly modified capillary holder. Here, the photon energy of the beam is up-converted by the HHG in a gas target. As target gas usually argon is used. The calculated cutoff energy is 48 eV, but the brightest harmonics are usually the 21^{st} (33.0 eV), 23^{rd} (36.1 eV) and 25^{st} (39.2 eV). A typical spectrum is shown in Figure 2.5.

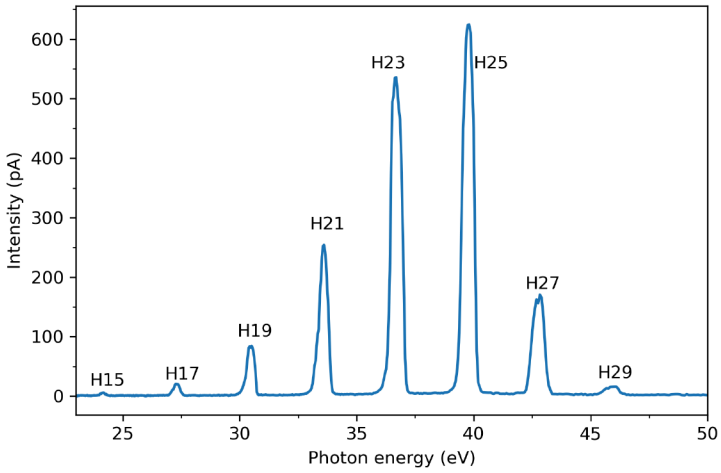

Figure 2.5: A typical HHG spectrum of the setup measured with a photodiode behind the monochromator. The 21st (H21), 23rd (H23) and 25th (H25) harmonic are preferentially generated.

The HHG radiation is transported by three grazing-incidence optical elements, the spherical vertical focus mirror (VFM), the toroidal monochromator grating and toroidal refocusing grating. The incidence planes of all three optical elements are horizontal. Contrary to its name, the VFM's main purpose is to focus the beam in horizontal direction on the entrance slit, to generate a vertically elongated footprint on the entrance slit. This allows to close the slit without losing too much intensity. The toroidal monochromator grating is projecting the beam from the entrance slit on the exit slit and selects the photon energy of the different harmonics. The last optical element is again a toroidal refocusing grating. Because its main task is to focus the beam on the sample, it is usually used in the 0th order like a mirror. This grating can be rotated 360° in the horizontal plane and is also used as a switching unit between two possible end stations. Both toroidal optics are symmetric in their horizontal and vertical focusing capabilities, if the incidence angle matches the design value. Because the VFM has asymmetric imaging properties, there will be a difference in the vertical and horizontal focus positions. This can be compensated by misaligning the refocusing grating to 16.2° instead of 17° incidence angle on purpose. The asymmetric beam propagation has the advantage of a small vertical diameter of the beam footprint on the sample. The position as well as the focal length of each of the three optical elements are listed in Table 2.1. Starting at the capillary, the beamline is enclosed and evacuated. The argon from the capillary is pumped by several stages of differential pumping.

	Vertical focus mirror	Monochromator	Refocusing grating
Position [mm]	580	1550	2820
Grazing angle [°]	11.8	19	16.2
Horizontal focal length [mm]	307	163	523
Vertical focal length [mm]	7335	160	563
Angular dispersion [mrad/nm]	-	0.993	0.581

Table 2.1: Position and optical properties of the three optical elements along the EUV beam path.

2.3 Photoelectron spectrometers

To collect the information from the photoelectrons in an efficient way, electron optics and a detector are needed. The electron trajectories are manipulated with electrostatic lenses and magnetic deflectors. Depending on the electron optics' setup, the energy, momentum and spatial distribution of the photoelectrons can be resolved. Today's state-of-the-art instruments incorporate either a hemispherical analyzer or a ToF spectrometer, which differ mainly in the method of energy selection (see Figure 2.6).

Hemispherical analyzers are well established for PES measurements. For energy selection, a radial electrostatic field is used to force the electrons into an elliptical orbit (compare to the Kepler problem [90]). The kinetic energy is selected by fixing the entrance and exit positions after half a revolution. Modern ARPES experiments are combined with a two-dimensional (2D) detector that can resolve, for example, the energy on the radial component and the parallel momentum with the azimuthal component. With additional optics in front of the detector, 2D momentum mapping for a fixed kinetic energy is also possible. Hemispherical analyzers can be operated with continuous light sources such as UV discharge lamps or X-ray tubes.

As the name implies, in a ToF spectrometer the kinetic energy is determined by the time the electrons travel through the spectrometer. This requires a pulsed light source with a well-defined starting point and a detector capable of measuring the time of arrival. In addition to the time of arrival of an electron, the point of arrival can also be detected in two dimensions with a delay line detector (DLD). This allows us to map the 3D electron distribution as a function of energy and either 2D momentum or 2D space at the same time. The direct measurement of three dimensions reduces the need to scan any parameter to measure the 2D band map and thus increases the electron transmission. The high electron transmission is very beneficial for FELs and HHG sources with a repetition rate in the lower kHz range to avoid long measurement times.

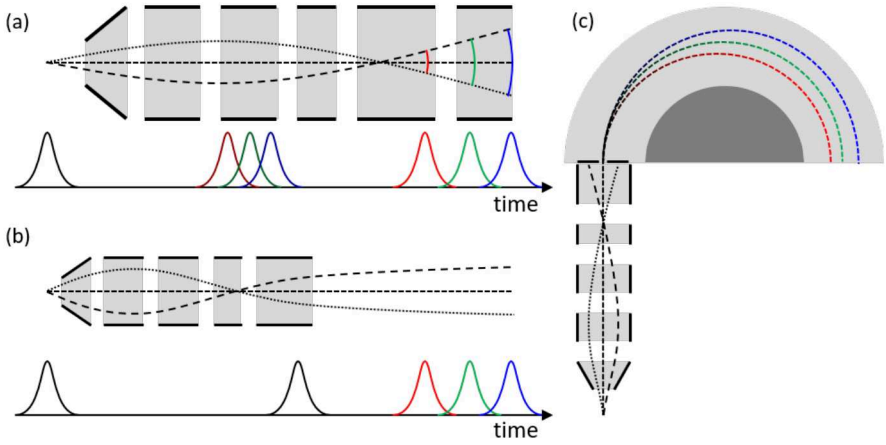

Figure 2.6: Overview over the general working principles of PES spectrometers. (a) Schematic of a ToF spectrometer as it is used in a commercial Themis Spectrometer. (b) Schematic of a momentum microscope with division in optical column in the front and the ToF drift tube for the energy separation. (c) Basic principle of a hemispherical analyzer.

2.3.1 The delay line detector

ToF PES spectrometers project a 2D band structure (k_x, k_y, E) onto the detector. This requires a detector capable of collecting 3D information, two spatial and the flight-time coordinate. The time resolution of the detector must be far below 1 ns, which is currently not achievable with solid-state detectors such as CCDs. DLDs are the detectors of choice because they meet the requirements. However, they have the disadvantage of being single-event detectors with some dead time.

DLDs have two or more long wires that meander across the hole detector area. A microchannel plate (MCP) is mounted on top to amplify the signal. To achieve the same spatial resolution in both x and y directions, a second delay line with perpendicular meanders is stacked on top of the first delay line. An electron hitting the detector is multiplied in the MCP and generates a charge in both delay lines at a specific location. The charge travels to both wire ends where the time is recorded with respect to a trigger signal. From the time pair, the arrival time and location of the electron on the detector can be measured (see Figur2.7). The difference of the signals can be assigned to the position, while their mean value refers to the arrival time of the electron. For reference, an external trigger is required. For a PES experiment, the trigger signal is synchronized to the photon source, otherwise the arrival time would be meaningless. DLDs are single-event detectors with a rather long dead time of 15 ns before the next electron can be detected. To overcome this single-event disadvantage, the detectors can be segmented [91]. Since the delay lines are also transparent to a certain extent, they can also be

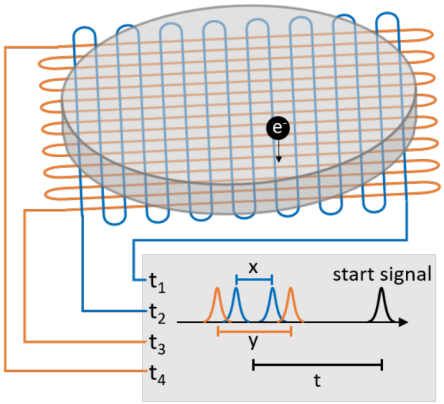

Figure 2.7: Electron detection scheme of a DLD. An electron is multiplied with the MCP in front of the detector. The amplified signal introduces a charge pulse in both delay lines, one for the x and one for the y coordinate. The charge is running to both ends of each delay line, where the time in reference to a start signal is measured. The difference of times at each end can be related to the x and y position, while the average will give the impact time.

stacked. This improves the detection efficiency and the coverage of the detector area, especially with segmented detectors.

2.3.2 The HEXTOF momentum microscope

A momentum microscope is an electron spectrometer for mapping the 2D parallel momentum distribution of electrons. Often these spectrometers are also capable of photoemission electron microscopy (PEEM) to measure real-space images. In recent years, these imaging capabilities in real and momentum space have been combined with a ToF section to add the kinetic energy as a third dimension. Such a ToF photoelectron spectrometer includes a column of electron optics at the front and a field-free drift section [16]. The separation of imaging section and energy-dispersive section [see Figure 2.6 (b)] reduces chromatic aberrations.

The electron optics uses the cathode lens technique to collect electrons emitted from all solid angles. At the front of the column of the electron optics, the cathode lens is at a high potential of up to several kV and extracts most of the electrons from the sample into the optical column. The electron beam is manipulated several times along the first part of the optical column, the upstream optics, to create a real-space image plane, the Gaussian image, and a reciprocal image plane, the momentum image. Then, in the downstream optics, the electron lenses are adjusted to select either the Gaussian or the momentum image and project the image onto the detector. In addition, apertures are installed in the upstream optics at the first momentum and Gaussian image planes to

confine the electron trajectories to the detector and reduce aberration effects. A smaller aperture in the Gaussian image plane will increase the momentum resolution, while a small aperture in the momentum image plane will increase the spatial resolution. In both cases, the energy resolution will also benefit. In addition, a region of interest can be selected, which is beneficial for small or inhomogeneous samples.

Due to the high voltage of the electron lenses, the kinetic energy in the optical column is primarily determined by these high potentials. Consequently, the flight time through this section is equally short for all electrons, and time dispersion can be neglected. This results in reduced chromatic aberrations. Good momentum resolution can be achieved over a range of several eV in binding energy depending on the size of the apertures. In particular, the higher the voltage at the extractor lens, the larger the field of view in momentum space. The settings are usually designed so that the slow electrons are in momentum or Gaussian focus on the detector. This guarantees the best possible energy resolution. To measure electrons from stronger bound states, the kinetic energy is retarded with a sample bias so that the kinetic energy at the detector matches the drift tube potential again.

The HEXTOF (High-Energy X-ray Time-Of-Fight) momentum microscope is designed as a semi-permanent tr-ARPES endstation of the PG2 beamline at FLASH [22]. The optical column of the PES spectrometer consists of 15 electrostatic lenses, a scheme of which is shown in Figure 2.8. Two apertures are installed in the upstream optics of the optical column. The first one, for the momentum image, is located at the position of the back focal plane and the second one is located at the first Gaussian image plane. Behind the optical column comes the drift section, where a 750 mm long drift tube is installed. The potential applied to the drift tube is of the order of a few volts, so that the electrons move much slower and their energy is dispersed over time. This potential is needed to move the slow electrons through this section before the fast electrons of the next pulse arrive. The electrons are detected by an eight-segment DLD (DLD6060-8s, Surface Concept) with two detector layers and four quadrants in each layer. To avoid gaps between the quadrants, the second layer is rotated by 45° with respect to the first layer. This allows the detection of multiple electrons per pulse, which is very advantageous for high intensity sources with medium repetition rates such as FELs. The diameter of the detector is 60 mm. The spectrometer has the capability to perform spin-resolved PES measurements. For this purpose, a spin filter crystal and a second ToF tube with detector can be installed at the end of the column of the electron optics. The spin filter crystal reflects the photoelectron spin selectively 90° upwards into the vertical ToF tube. Thus, it is sensitive to the horizontal inplane spin component.

A rendered image of the complete experimental setup is shown in Figure 2.9(a). In addition to the spectrometer, the setup is equipped with beam diagnostics, sample preparation tools, and sample transfer and storage capabilities. It consists of the main chamber with the spectrometer and the preparation chamber with load lock, sample storage

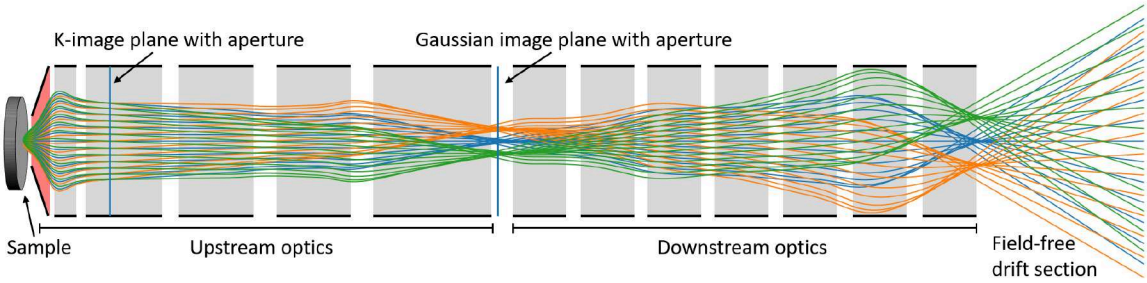

Figure 2.8: Scheme of the optical column of the HEXTOF spectrometer. The sample is located on the left. The electrons are pulled into the optical column by the extractor lens (red). On the right side the electrons enter the field free drift section, where the electrons are separated by kinetic energy. The detector is not shown here. It would be far on the right side.

magazine and preparation tools. The sample holder at the front of the spectrometer is mounted on a hexapod for precise adjustment of position and tilt. An open-cycle flow cryostat cools the sample holder with liquid nitrogen or helium to cryogenic temperatures below 100 K or 50 K, respectively. A retractable antenna and diode are installed at the beamline port of the main chamber to ensure spatial and temporal alignment of the pump and probe beams. By reading the antenna signal on an oscilloscope, the temporal delay between the two pulses can be determined with an accuracy of better than 40 ps and the delay stage can be adjusted accordingly. During the measurement, the preparation chamber can be separated from the main chamber by a valve so that a second sample can be prepared in parallel. For in-situ preparation, a sputter gun, an electron beam heating stage, a gas inlet system, and several connections for evaporators are available. A mass spectrometer and a low energy electron diffraction (LEED) device are installed for characterization. The complete setup is mounted on a four-way adjustable support frame to position the chamber according to the beamline requirements.

2.3.3 The WESPE endstation

Another semi-permanent endstation for the PG2 beamline is the WESPE (Wide angle Electron SPEctrometer) setup. It is designed for time-dependent angle-integrated core-level photoemission experiments at FLASH. It is equipped with two Themis 1000 ToF spectrometers, one at normal emission and the other at an angle of 71°. Both ToF spectrometers are manufactured by SPECS and can be used in parallel. For the experiment reported here, only the normal-emission ToF was used, which operates with a four-quadrant DLD. The FEL beam is incident at an angle of 55° to the sample normal. A hemispherical analyzer and X-ray tube are available for use in the laboratory without a pulsed EUV or X-ray source.

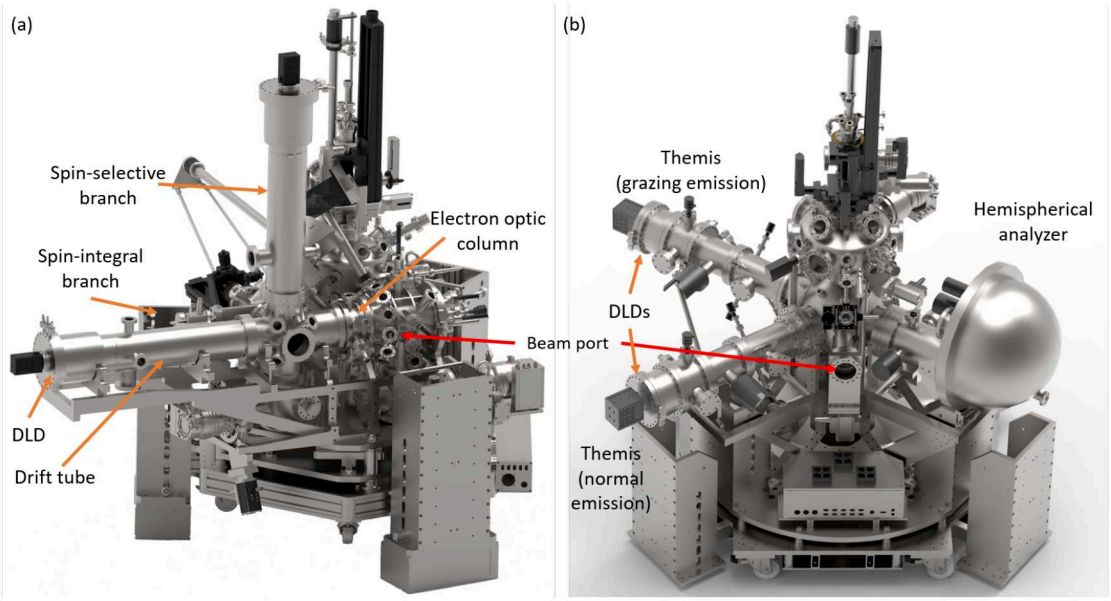

Figure 2.9: Rendered images of the two endstations for the PG2 beamline. (a) HEXTOF setup with installed spin branch. In front is the main chamber with the spectrometer to the left. (b) WESPE with two ToF spectrometers to the left and the hemispherical analyzer on the right. Courtesy of S. Gieschen and H. Meyer.

The Themis spectrometer does not use an extraction lens, and instead of a sample bias, a retardation voltage is used inside the spectrometer, similar to a hemispherical analyzer. This voltage slows down the electrons to select those of interest and suppress secondary electrons. Due to this design of the electron optics, the electrons are dispersed over the entire length from the sample to the detector. Due to chromatic aberrations, the energy calibration requires SIMION calculations for reference [92]. The energy calibration is described in some detail in Section 3.3.1 and in full detail in the PhD thesis of L. Wenthaus [92].

The vacuum chamber also has two sections, the main chamber at the bottom with all spectrometers installed and the preparation chamber above. A manipulator with the sample holder is installed on top to transfer the sample between the two chambers. The sample holder is mounted on an open cycle flow cryostat to cool the sample with liquid helium down to 9 K. Similar to the HEXTOF setup, the preparation chamber is equipped with tools for sample preparation and characterization as well as a load lock and additional ports for ancillary equipment.

3 Single-event data processing

3.1 Single-event data recording

Because DLDs are single-event detectors, all data can be stored in an event-based data frame. For each event, the detector records three values, the arrival time and the 2D position in x and y. The binning and integration are done during post-processing at the software level, which allows for corrections and flexibility. It also keeps the amount of stored data small, since no 3D detector data cube needs to be stored. Other properties, such as the position of the delay stage in a pump-probe experiment, can also be recorded. Since their readout is not intrinsically synchronized to the DLD detector, the pulse ID of the photon source is used. Each value of each channel is indexed with the pulse ID at the time of its readout.

At FLASH, data from the DLDs is integrated into the main data acquisition server (DAQ). In addition to the DLD information, the DAQ collects machine parameters of the FEL and the pump laser. The channels have different readout speeds. The fast ones provide information for every shot, while others provide only one value per train or less. Data acquisition for the momentum microscope in combination with the HHG source is similar, but with only a few additional channels.

To ensure comparability of each spectrum in a pump-probe measurement at different delays, the state at each delay must be comparable. Due to the SASE fluctuation, the FEL intensity is not stable and degradation due to aging effects can occur over long measurement times. One measure against unstable measurement conditions and degradation is a continuous delay scan, where the delay stage moves back and forth. Since each delay is measured many times, fluctuations are averaged out.

3.2 Single-event data processing

For the evaluation, the self-developed software framework HEXTOF-processor is used, which is available as a Python package [93]. This software reads the data into an electron-based data frame. This data frame consists of a table of all events recorded by the DLD. A column is added to the table for each channel and a row for each event. For channels with slow readout, it is assumed that all pulses before the next readout have a similar value, or the readout is an integrated value. The value of a readout is used for all pulses between two readouts. The software package also provides tools for conversion,

Figure 3.1: Scheme of the data structure and processing. On the left side raw data are depicted channel by channel and ordered by the pulse ID. The raw data are sorted into the electron data frame (right side). For channels with slow readout, a forward filling routine is filling intermediate pulse Ids. Additional channels can be calculated for example for the energy calibration.

calibration and filtering. The conversion is applied to the electron data frame where a new column with the converted data is added. The third tool is the multi-dimensional binning function to map the distribution of electrons over several dimensions [94].

Because of the discrete nature of digital data, binning artefacts can appear, especially when the sampling rate is only slightly higher than the width of a resolvable features in the spectrum. At the measurement, the analog signal needs to be converted into digital signal before it is sent to the DAQ. The continuous analog signal is converted into the discrete digital signal by sampling. The sampling rate defines the spacing between two values, which is usually equally spaced. The discrete values can cause binning artefacts in the data processing, especially when the binning steps are only a few sampling steps wide. If the binning steps are not a multiple of the sampling steps, the number of discrete values covered per binning step will alternate in regular intervals between two values. Mathematically, this phenomenon can be explained as interference between the sampling rate and binning frequency, resulting in a beat pattern. For instance, if the binning step size is 3.2 times larger than the sampling step size, every fifth bin will cover four discrete values, while the other four bins will only cover three values. To overcome this issue, each value can be randomly shifted by an offset. The offset distribution should be uniform with a spread equal to the sampling spacing.

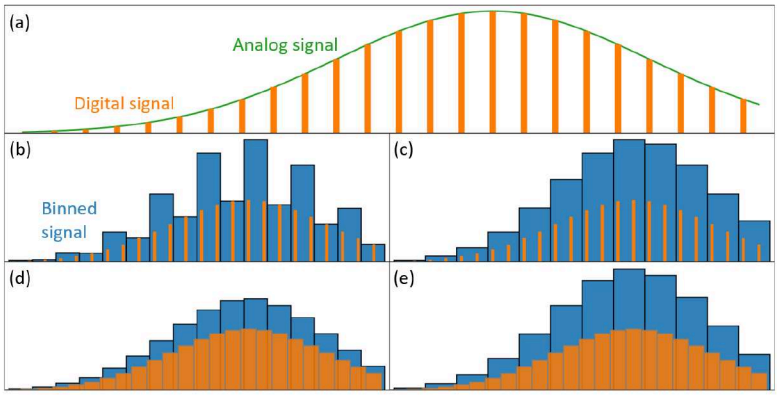

Figure 3.2: Simplified scheme to demonstrate the impact of binning artefacts. (a) An analog signal is digitized with a constant sampling rate. For data processing the digital signal is binned [see panel (b-e)]. In panel (b) binning step size is 1.5 times the sampling rate which results in a modulation of the signal. Every second bin contains two sampling steps while the others only one. In this example, the amplitude of the modulation has a similar size compared to the signal itself. The modulation will vanish if the binning step equals a multiple of the sampling step width, as shown in panel (d). (c,e) If the digital values are evenly spread out over the sampling step width, the modulation disappears, because some values are shared by two neighboring bins.

3.3 Data analysis

Due to fluctuations, the binned data might need to be normalized along a scanned axis. In a pump-probe scan, the changes in intensity can be accounted for by normalization. Unfortunately, there is currently no I_0-monitor available for a reliable measurement of the FEL fluence behind the monochromator. An indirect measurement of the FEL intensity is the count rate on the detector of the spectrometer. Assuming that the excitation by the pump pulse does not affect the total photoemission cross-section, the spectral weight of each delay can be used for normalization. Some of the measured parameters need to be converted into a meaningful quantity. The momentum field of view can be determined by measuring a known structure as reference with the same setting for the electron optics.

3.3.1 Energy calibration

As the binding energy is an important quantity for PES, the flight time should be converted into an energy axis. In the momentum microscope a simplified conversion is straightforward, because the drift tube for the energy dispersion is separated from the imaging optics. With the cathode lens design, the electron optics suppresses chromatic aberration. In the ToF section, we can assume that the electrons travel in a field-free space. The kinetic energy of an electron is given by the length l of the section and travel time through the section t_{ToF}:

$$E_{kin,ToF} = \frac{m_e v^2}{2} = \frac{m_e l^2}{2t_{ToF}^2}. \tag{3.1}$$

Because of the high extractor voltage at the cathode lens and the high potentials applied to the electron upstream optics, all electrons are moving fast and with nearly the same speed through the electron optics column. Thus, we can assume that all electrons enter the drift tube of the ToF section at the same time t_0. The difference to the arrival time t at the detector gives then the travel time $t_{ToF} = t - t_0$. Voltages applied to the sample V_{sample} and the ToF section V_{ToF} will retard the kinetic energy in the ToF section. The kinetic energy at the sample is given by

$$E_{kin,sample} = E_{kin,ToF} + V_{sample} - V_{ToF}. \tag{3.2}$$

The arrival time t on the DLD can be converted into binding energy of the electron by inserting Equations 2.1 and 3.1 into 3.2:

$$E_{bind} = h\nu - \frac{m_e l^2}{2(t-t_0)^2} - \Phi - V_{sample} + V_{ToF} = -\frac{m_e l^2}{2(t-t_0)^2} - E_0, \tag{3.3}$$

where E_0 is an energy offset, which is the sum of the photon energy, the work function, the sample bias, and the ToF-tube potential.

The time offset t_0 and, if unknown, the energy offset E_0 can be determined either by varying the sample bias or identifying multiple features of a reference spectrum with known binding energy. Varying the sample bias changes the kinetic energy of the electrons in the ToF tube. Hereby, several spectra are taken with different sample bias in the range of $\pm$10eV. This method typically results in greater precision at lower kinetic energies, but may sacrifice accuracy across a wider range of energies.

If a lager range of binding energy with high accuracy is required, chromatic aberration needs to be taken into account. The trajectories through the spectrometer differ slightly in length and, therefore, in flight time. For a more precise time-to-energy conversion the flight time is simulated as a function of detector position and kinetic energy. The ray tracing simulation tool SIMION was used to simulate various trajectories for this purpose. Relativistic effects are also considered in the simulation. This method is also used for converting raw data from the Themis spectrometer of the WESPE setup. This is necessary because the lenses are distributed over the full length of the spectrometer and the electrons disperse in energy while propagating through the lens structure. As a result, electrons with the same kinetic energy are hitting the detector at different times depending on their position on the detector.

3.3.2 Distortion correction and symmetrization

Imperfections in the electric fields of the electron lenses and other stray fields like the geomagnetic field will have an impact on the detector image. As a result, the image can be distorted, and the detector might be unevenly illuminated. In the photoemission process, also matrix-element effects can create complex anisotropic modifications to the intensity symmetry in the momentum image. With interpolation algorithms, binned data can be manipulated. Therefore, rotation symmetry arguments are exploited to determine the distortion. The actual position of landmarks is determined and related to their target position as it can be seen in Figure 3.3(a). With the help of the Python-based MPES software framework [95, 96], the transformation between actual positions and target positions is found. This transformation is then applied to all energy slices of the detector image [Figure 3.3(b)]. Symmetrizing the data helps to compensate for illumination issues.

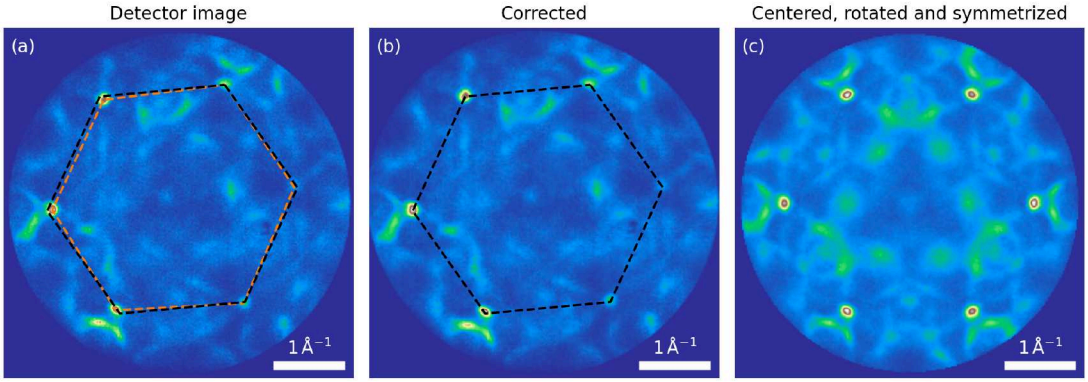

Figure 3.3: Momentum map of the Fermi surface of Graphene on Ir. The Dirac points of Graphene are used to correct for distortion. In panel (a) the raw detector image is shown. The actual positions of the Dirac points are connected with the orange lines. For reference, a regular hexagon is shown in black. (b) The same momentum map after the data set has been corrected for distortion. (c) The data are centered to the Γ position and symmetrized by a threefold symmetrization. The full image is also rotated, so that x and y coordinates correspond to the ΓK and the ΓM directions, respectively.

4 Graphene on iridium as a performance benchmark

This chapter deals with the measurement performance of the HEXTOF spectrometer combined with the HHG light source. The measurement quality of an experiment is not just given by the capabilities of the spectrometer, but also by the EUV light source. To characterize the performance of the setup, we investigated the electronic band structure of a graphene monolayer on Ir(111). But first, we will focus on the capabilities of the eight-segment DLD.

4.1 The eight-segment detector

To enhance the multicount capabilities, a novel eight-segment detector design was chosen. Because the segments are distributed in two layers of four quadrants, there is a rather large possibility that an electron will be detected in both layers. At the edge of two quadrants there is also the chance that an electron can be detected in both quadrants, because the detector areas are overlapping slightly. The double counting of an electron can be used to estimate the detector resolution.

Looking at the distribution of events on the detector per pulse as it is shown in Figure 4.1(a), one can see that double events are most likely. Also, four events at the same pulse are more likely than three or five. With higher average count rate, the distribution shifts to higher number of events per pulse. To understand this behavior, we take a closer look at the pulses with two recorded events. In Figure 4.2(b) the distribution of event pairs of the highest average count rate [green data in Figure 4.2(a)] as a function of the distance between the two counts on the detector is shown. For the majority of pairs, the events appear in close proximity to each other, with over 50 % of pairs being spaced by less than 5 pixels. However, there are also pairs that spread across the entire detector. Analyzing pairs of counts measured with the same detector layer, one can see that the distribution of widely spread events follows very closely the distribution of two uncorrelated counts. The event pairs that are strongly correlated are only found for pairs that have one count on each detector layer. This leads to the conclusion that those are double counts from the same electron, while the others are two single counts arise from two different electrons. The peak width of the double counts in the distribution gives us an estimate of the spatial detector resolution. The resulting FWHM of the peak is 10

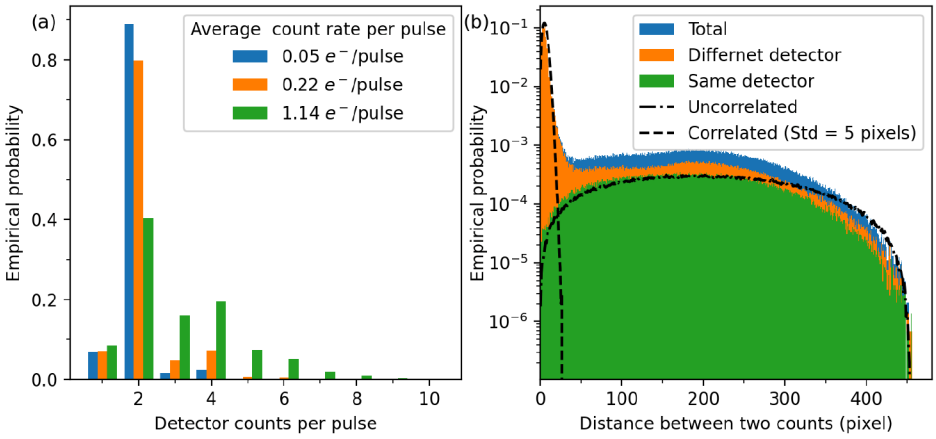

Figure 4.1: (a) The multi-hit distribution for different average count rates. Shown is the empirical probability that several events are counted for a single pulse. For all three count rates double events are most likely, but with higher count rate it is more likely to detect three or more events per pulse. (b) The spatial distribution of the distance between event pairs. The data are taken from the pulses with double events of highest count rate. The distribution of double events in a single detector layer (green) closely follows the calculated distribution of uncorrelated events (dash-dotted line). However, event pairs distributed between both layers (orange) exhibit an additional peak when the distance is small. This peak can be modeled with correlated electron events with a standard deviation of 5 pixels (dashed line).

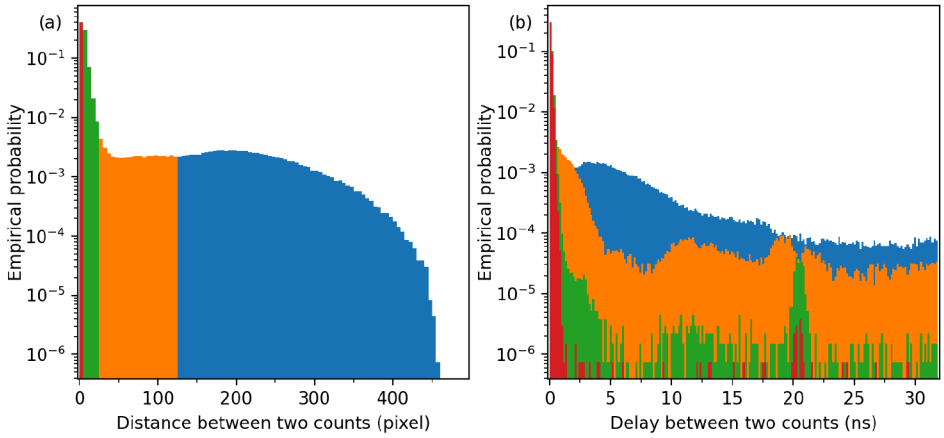

Figure 4.2: Spatially correlated events are also correlated in time. (a) The spatial distribution with color code for the pairs within 1σ in red, from 1 to 5σ in green and further out in orange and blue. (b) Temporal delay distribution of the double events sorted by the spatial distribution. The majority of spatially correlated events show minimal delays between pairs of events. Note that the event pairs presented in red are representing roughly 50% of all events pairs.

pixels. For lower average count rates, the correlated peak keeps its shape and only the uncorrelated background decreases.

As expected, those spatially correlated counts are correlated in the time domain as well. In Figure 4.2 we see that events which are spatially close on the detector are also very likely close in time. The peak of correlated events has in time a FWHM of 374 ps, which can be seen as the combined resolution of both detector layers. Assuming both layers to be aligned, the time resolution of the detector is 266 ps FWMH, which roughly translates into an energy resolution of 20 meV at a ToF-tube voltage of 10 eV to 100 meV at a ToF-tube voltage of 30 eV.

The resolution of the double counts is a combination of the resolution of a single quadrant and the misalignment of the two layers. In Figure 4.3(a) the spatial shift between the detector layers is shown as a function of the detector position. Each arrow is pointing from the position of counts in the first layer to the position in the second layer. Only events with a spatial separation of less than 25 pixels are taken into account, to ensure correlation of the events. Each arrow is representing multiple double counts appear at that position on the first layer. Because the two detector layers are rotated by 45° to each other, causing each quadrant to overlap with two quadrants of the other detector layer. As a result, the overlapping area is actually a 45° segment of the full detector, giving the impression of eight segments. In each of these segments, the shift between

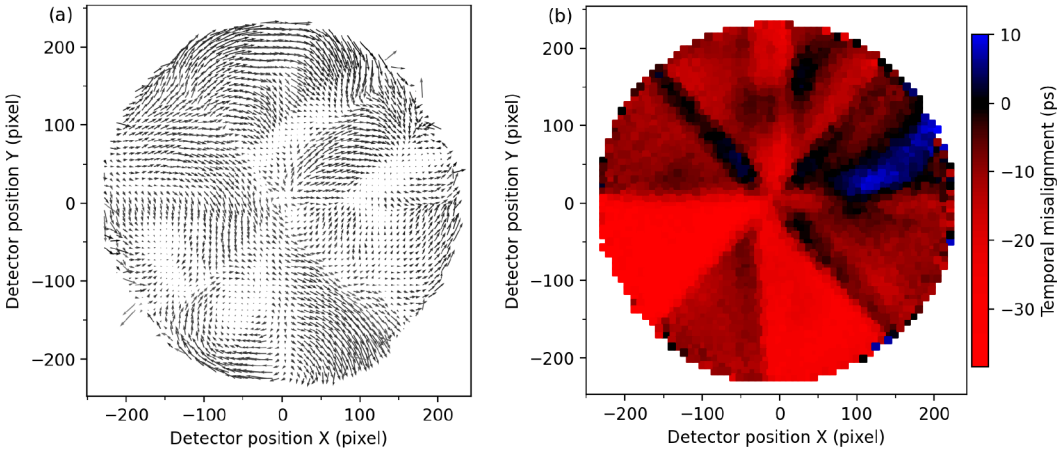

Figure 4.3: Misalignment of the two detector layers. The average difference between both layers will give an estimate of the mismatch. In (a) the spatial misalignment is shown. Each of the eight sectors (combination of quadrants in the upper and the lower detector layer) has its own characteristic. Note that the mismatch (arrow length) is enhanced by a factor of three. The temporal mismatch is presented in (b). Most of the detector area for the second layer is delayed by up to 50 ps. A similar pattern as in the spatial distribution can be seen.

the different quadrants has a strong general trend over the segment, but also inhomogeneities in length or direction appear, especially at the edges of most segments. In a similar manor, the temporal shift between the detector layers is shown in Figure 4.3(b) as a function of the detector position. Over most of the area, the temporal difference between the layers is only a few ps, but also the difference between maximum and minimum is with 50 ps much smaller than the overall temporal resolution of the detector with 266 ps. Correcting for the shift between the detector layers can increase the resolution. Additionally, taking the average of the event pairs of from a single electron can also improve the resolution by up to a factor of $\sqrt{2}$.

4.2 Graphene band structure

Although Landau predicted that 2D crystals of carbon will be thermodynamically unstable [97], the band structure of the 2D sp^2 hybridized carbon crystal was theoretically described more than 70 years ago [98, 99]. However, it was presumed that graphene can only exist as a 2D part of a 3D structure. When K. S. Novoselov and A. K. Geim proofed this wrong by exfoliation of a single layer of graphite [100], the interest in

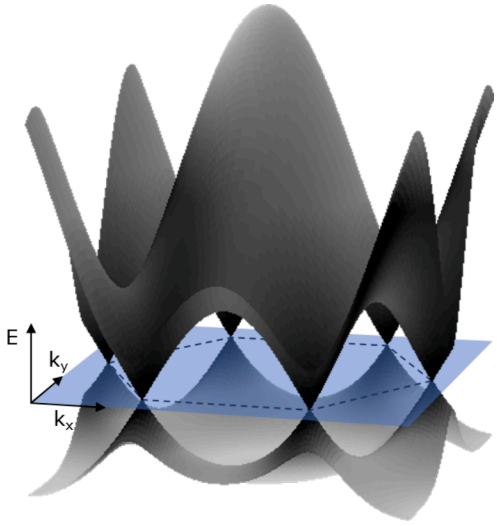

Figure 4.4: The band structure of the graphene π-band, calculated with the tight-binding model in the next nearest-neighbor approach. [98]

graphene skyrocketed since 2004 [101]. Over the last two decades, many properties of graphene are well understood and high-resolution data are available for comparison.

In graphene the carbon atoms are bond covalently. The sp^2 hybridized orbitals of carbon atoms form the three σ-bonds with a bond angle of 120°, which results in the honeycomb lattice of graphene. The π-bands are responsible for the unique features of the electronic structure, such as the Dirac cone, as shown in Figure 4.4. These bands are formed by the delocalization of electrons from the remaining p_z-orbitals across the lattice. The two π-bands can be identified as conduction band and valence band, respectively. At the Dirac points, the K points in the Brillouin zone, both bands touch each other. The band dispersion is in the vicinity of this point linear, which resembles an ultrarelativistic or massless particle. In this regime the quantum mechanics are described by the massless Dirac equation [98, 102–104].

Graphene is prone to grow on multiple carbon rich metal surfaces [105, 106]. We have grown graphene by thermal decomposition of ethylene gas on the Ir(111) surface. The preparation procedure involves first cleaning of Ir(111) by sputtering and oxygen treatment. Afterwards, graphene was grown with the chemical vapor deposition technique [107]. Due to a small mismatch in the lattice constant of graphene (2.45 Å) and the Ir(111) (2.715 Å) surface, a moiré superstructure occurs. Surface quality was checked by LEED.

The graphene on Ir sample provides excellent structural and electronic properties to benchmark the setup in the laboratory. Because graphene is a 2D material, there is no k_z dependence in the π-bands. With the characteristic features at the edge of the Brillouin zone, the momentum field of view and the momentum resolution can be determined.

Also, the fast dynamics are beneficial to determine time resolution. Graphene on Ir(111) is quite inert to surface contamination. The sample stays clean over several weeks in vacuum, even with the constant stream of argon at 3×10^{-9} mbar coming from the HHG source. All photoemission measurements were done at room temperature.

4.3 Measurement capabilities

As mentioned in Section 2.3.1, the DLD detector records the cubic band structure without the need of scanning any parameters. In Figure 4.5, a typical measurement of graphene on Ir(111) is presented, where four different cuts through the data cube are shown. The first panel (a) shows the momentum map at the fixed energy of the Fermi level, while the other three show the energy-momentum band dispersion of the π-band. Subplot (b) cuts through the K symmetry point in k_y direction, (c) and (d) are cutting through in k_x direction, through K-Γ-K' and through K-M-K' along the edge of the Brillouin zone, respectively. The field of view for this measurement is ± 2.4 Å which covers more than the first Brillouin zone of graphene on iridium. For the setting used here, 8 kV are applied to the extractor. Higher extractor voltages usually increase the field of view in momentum space and vice versa in the spatial mode.

4.4 Effective resolutions of the setup with the HHG source

Besides the detector, also the HHG source and the spectrometer have their contribution to the experimental energy, momentum, and temporal resolutions of the setup. Here, the energy and momentum resolutions are estimated from the graphene π-band crossing the Fermi level. The temporal cross-correlation of the pump and the probe pulses is retrieved from the temporal evolution of excited states from pristine iridium.

Figure 4.6 summarizes the energy, momentum, and time resolution of HEXTOF in combination with the HHG source. In Figure 4.6(a) the static ARPES measurement of the Dirac cone is shown, using a photon energy of 33 eV (21^{st} harmonic). The E–k photoemission intensity map shows the vicinity of the K point, from which we can extract the momentum distribution curve (MDC) at E_{F} (top panel) and an energy distribution curve (EDC) along the π-band. Therefore, multiple MDCs are fitted with the line profile of the π-band and the EDC is derived from the amplitude of the line profile energy distribution [109]. To determine the energy resolution, the EDC was fitted with a convolution of a Fermi-Dirac distribution function at room temperature and a Gaussian resolution function [Figure 4.6(a), right panel]. As a result, the total energy resolution has a FWHM of 96 ± 4 meV. The total energy resolution is a convolution of

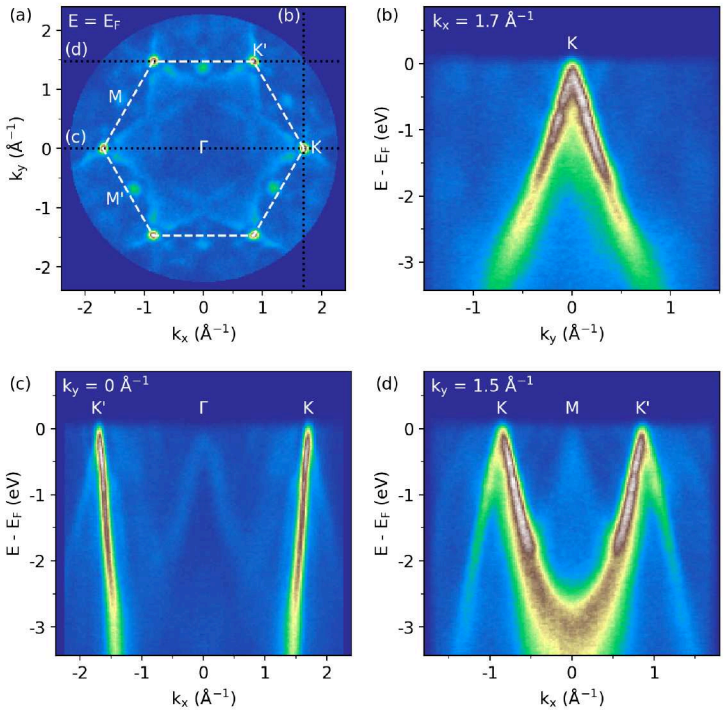

Figure 4.5: Four-dimensional (k_x-k_y-E-intensity) momentum microscopy data of graphene on pristine Ir(111) recorded at room temperature using the 27$^{\text{th}}$ harmonic ($h\nu = 42.4\,\text{eV}$). Shown are four cuts through the data stack. (a) Parallel momentum map (k_x-k_y) of the Fermi surface (energy integration window: $\Delta E = \pm 0.1\,\text{eV}$). The dirac point of graphene are visible at the K points of the Brillouin zone of graphene which is indicated as well as its high-symmetry points are. (b–d) E-versus-k band maps for different k linecuts through the K points. The linecuts are indicated by black dotted lines in (a) (momentum integration window: $\Delta k = \pm 0.07\,\text{Å}^{-1}$). Reprinted from [108]

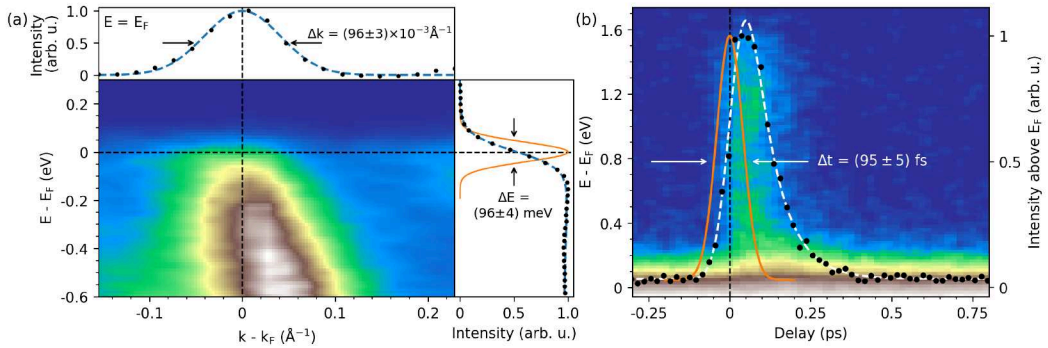

Figure 4.6: (a) Energy-versus-momentum photoemission intensity map of graphene/Ir(111) near the K point with a photon energy of 33.4 eV (21$^{\text{st}}$ harmonic; momentum integration window: $\Delta k = 0.13\,\text{Å}^{-1}$). Top panel: Momentum distribution curve (black dots) at E_F plus fit (blue dashed line). Right panel: Energy distribution curve (black dots) representing integrated MDC peak intensities plus fit (blue dashed line) and the resulting energy resolution (orange line). (b) Pump-probe photoemission data on Ir(111) taken with a pump wavelength of 800 nm (1.57 eV) and a probe photon energy of 36.1 eV (23$^{\text{rd}}$ harmonic). The full momentum-integrated energy-versus-delay photoemission intensity map at the Fermi level and the energy-integrated intensity transient (black dots) plus fit (white dashed line) are shown. The resulting time resolution is indicated by the orange line. Values for the Gaussian FWHM determined from the fits, corresponding to effective experimental resolutions, are indicated. Both measurements, for (a) and (b), are recorded at room temperature. Reprinted from [108]

the spectral bandwidth of the HHG source on the sample and the energy resolution of the spectrometer.

Due to the monochromator, the HHG beam is dispersed in energy in the vertical direction on the sample. The spatial selection by the field aperture of the momentum microscope can be interpreted as a virtual exit slit, which limits the spectral bandwidth in the field of view to about 90 meV. The electron spectrometer contributes with an estimated resolution of 30 meV. Depending on the harmonic, the effective energy resolution of the HHG source varies due to the photon energy dependence of the grating resolution for a fixed slit size. Over the entire usable spectral range of ≈24–46 eV, the energy resolution reduces from 80 to 135 meV, by using the field aperture, selecting an effective field of view of ≈70 μm in diameter on the sample.

As shown in the top panel of Figure 4.6(a), the MDC line fit of the π-band at E_F results in a Gaussian FWHM of $0.096 \pm 0.003\,\text{Å}^{-1}$. This includes the intrinsic π-band momentum width of $0.031\,\text{Å}^{-1}$ [110, 111]. After subtracting the intrinsic contribution,

the resulting effective momentum resolution is $0.091 \pm 0.003\,\text{Å}^{-1}$, which is influenced by imaging capabilities of the electron optics and detector resolution. Note that the effective momentum resolution could be overestimated because of the unknown difference in sample quality with respect to the referenced experiments in the literature [110, 111]. There are no noticeable changes of the momentum resolution, when other harmonics were selected.

To estimate the temporal resolution of a time-resolved experiment, we determine the cross-correlation between pump and probe pulses. To this end, the dynamics of the electronic structure of pristine Ir(111) were measured using the pump-probe photoemission technique. The sample was pumped with the fundamental of the Ti:Sa laser at a photon energy of 1.57 eV and a fluence of $2.42\,\frac{\text{mJ}}{\text{cm}^2}$. The 23^{rd} harmonic (36.1 eV) was used to probe the electron dynamics. Figure 4.6(b) presents an E–t_{delay} intensity map integrated over momentum. It depicts the electron dynamics close to t_0 with the transient generation and relaxation of hot electrons above E_{F}. By integrating the intensity over energies larger than E_{F}, the corresponding transient (black data points) is derived. This signal of the excited electrons was fitted with a constant decay rate model, including a step function for the photoexcitation and a Gaussian function to mimic the temporal width of the pulse. The resulting Gaussian FWHM is 95 ± 5 fs, giving an estimate of the temporal system response function. The pump pulse duration was estimated to be 67 ± 5 fs FWHM at the sample position. For this purpose, the initial pulse length of the laser was measured with the GRENOUILLE (Grating-Eliminated No-Nonsense Observation of Ultrafast Incident Laser Light E-fields) autocorrelator at the output of the amplifier. Temporal broadening of the pump pulse dispersion was included by calculating the dispersive effects for all transitive optics in the pump branch. Assuming that both the pump and probe pulses are uncorrelated, the duration of the probe pulse will, by chance, also be 67 ± 5 fs FWHM.

4.5 Multi-spectral capability

With the monochromator of the HHG source different harmonics can be selected and, therefore, the wavelength can be tuned in discrete steps. Figure 4.7 displays two typical EUV spectra of the HHG source as a function of the monochromator energy. The spectrum indicated by the black line is the calculated photon flux at the sample position. The signal was measured by an EUV-sensitive photodiode behind the exit slit of the monochromator (similar to Figure 2.5) and corrected for beamline transmission, including Al-filter transmission to block stray light of the driving laser. The second spectrum (red line) represents the electron count rate at the detector for the measurement of the graphene/Ir(111) band structure at the Fermi level. The sample bias is adjusted for each wavelength to keep the Fermi level in focus. This favors usually lower photon energies because less of the secondary electrons are cut away. The spectral width of the detector

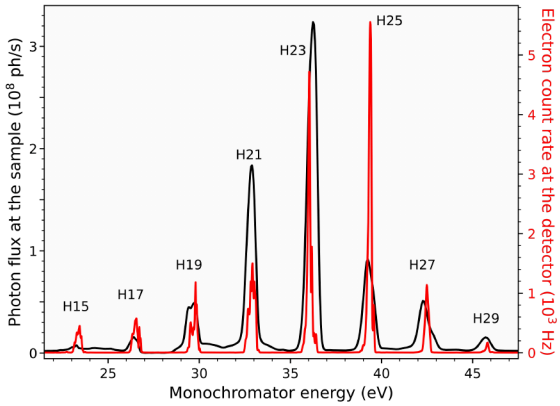

Figure 4.7: Higher harmonic spectra as given by photon flux (black line) and electron count rate on the DLD (red line). Spectra were measured by scanning the monochromator energy with an exit slit size adjusted to a corresponding monochromator resolution of 150 meV at the 23$^{\text{rd}}$ harmonic. The EUV intensity was measured with an EUV-sensitive photodiode behind the exit slit of the monochromator and with the momentum microscope from a graphene-covered Ir(111) sample, respectively. The photon flux at the sample position was calculated from the diode current, accounting for the quantum efficiency of the diode, the beamline transmission, and the beam attenuation. Adapted from [108]

counts is smaller because the field aperture of the spectrometer is acting as a virtual exit slit of the monochromator. The aperture selects only a small part of the footprint of the dispersed HHG beam.

The combination of highly efficient 3D photoemission intensity $I(E,k_x,k_y)$ imaging with the multispectral HHG source gives us the unique opportunity to perform k_z-dependent trARPES. Fermi surface maps of graphene/Ir(111) taken with all wavelengths of the eight harmonics are presented Figure 4.8. These 2D intensity maps are extracted from the full 3D data cubes that were originally measured. Depending on the count rate, the data acquisition times varied from 2 h to 12 h. The multispectral Fermi surface maps reflect a superposition of the k_z-independent Fermi surface of graphene and the 3D Fermi surface of Ir(111). There is no photon energy-dependent change in the shape of the graphene Dirac points, whereas the variation in the shape of the Ir 5d intensity pattern, i.e., k_z dispersion, is pronounced. Another observation is that the relative contribution of the Ir 5d signal to the total photoemission intensity at E_{F} is continuously suppressed upon increasing the photon energy from 23.6 eV to 45.5 eV. We attribute this effect to a decrease in the electron escape depth upon approaching the minimum of the universal curve of the inelastic mean free path around a kinetic energy of ≈50 eV [63]. With increasing surface sensitivity, the photoemission signal from Ir(111), which

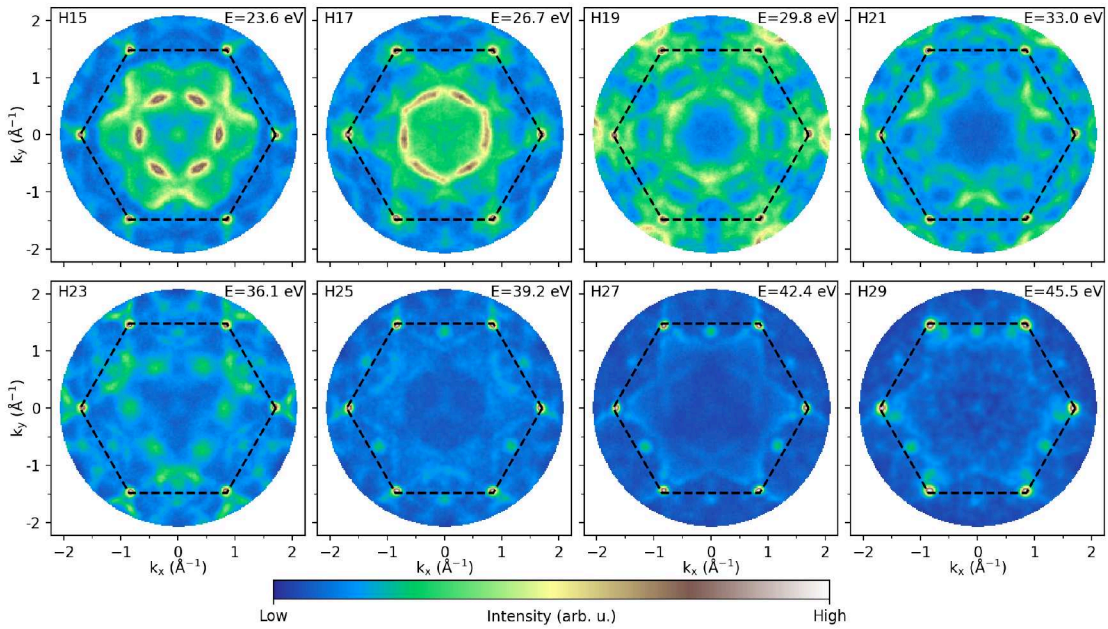

Figure 4.8: Complete series of Fermi surface maps of graphene on Ir(111) recorded over the photon-energy tuning ranges from 23.6 to 45.5 eV (15$^{\text{th}}$ to 29$^{\text{th}}$ harmonic; energy integration window: $\Delta E = \pm 0.1$ eV). Each panel represents a parallel momentum map for the next harmonic. The hexagonal Brillouin zone of graphene is indicated by dashed lines. At higher photon energies, the graphene signal from the Dirac point increases relative to the Ir signal strength. The sample was measured at room temperature. Adapted from [108]

is covered by a graphene monolayer, decreases.

4.6 The three-dimensional Fermi surface of iridium

Each constant-energy map displayed in Figure 4.8 can be mapped onto a spherical surface in 3D momentum space by using Equation 2.4 for the surface-perpendicular momentum component. The empirical parameters for Ir(111) are the effective mass $m^* = 1.07\, m_e$ and the inner potential $V_0^* = 10$ eV [112]. Using the 15^{th} to 29^{th} harmonic allows us to reconstruct the 3D Fermi surface tomogram in the upper half of the second Brillouin zone in a range of k_z from 0.3 Å^{-1} to 1.2 Å^{-1} above Γ. Thus, our tomographic data cover ≈39% of the Brillouin zone volume of Ir(111). Exploiting point symmetry about the center of the Brillouin zone (Γ point), the tomogram of the 3D Fermi surface

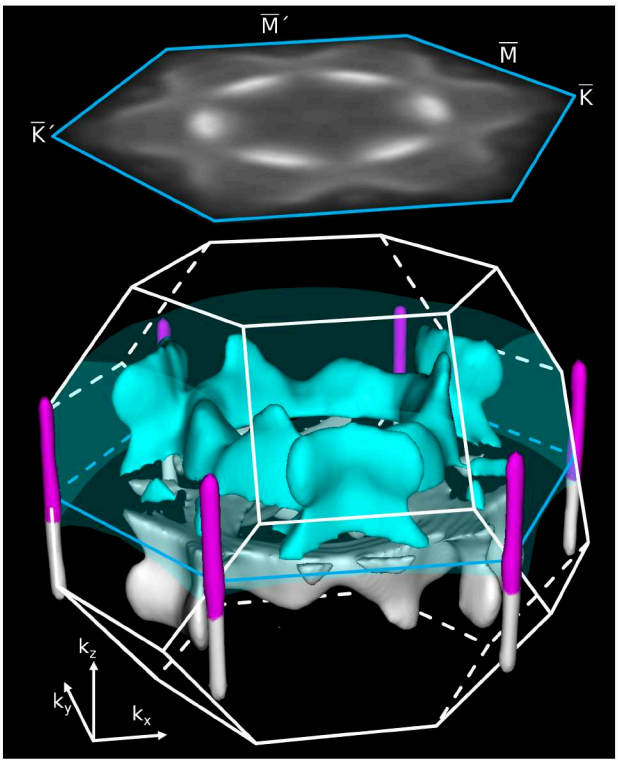

Figure 4.9: Bottom part: 3D Fermi surface tomogram of graphene/Ir(111), reconstructed from the Fermi surface maps shown in Figure 5. The 2D and 3D Brillouin zones of graphene and Ir(111) are indicated by blue and white lines, respectively. The part of the 3D Fermi surface tomograms obtained directly from the measured data are highlighted in magenta and cyan for graphene and Ir(111), respectively. The corresponding 3D Fermi surface tomogram obtained by point reflection around the Γ point are shown in gray. Upper part: Interpolated parallel momentum Fermi surface map of Ir(111) through the Γ point. Reprinted from [108]

can be reconstructed also in the lower half of the Brillouin zone. Figure 4.9 displays the reconstructed portion of the 3D Fermi surface for graphene/Ir(111). Three sets of isosurfaces can be identified: The non-k_z-dispersive graphene Fermi rods, centered at the corners of the hexagonal graphene Brillouin zone are shown in magenta. The Fermi surface of Ir 5*d* bulk is displayed in cyan. The remaining grey isosurface represents the extension of both isosurfaces into lower parts of the Brillouin zone by symmetry arguments. The reconstructed Ir 5*d* Fermi surface is in good agreement with a 3D Fermi surface tomogram obtained from pristine Ir(111) by soft X-ray momentum microscopy [112].

4.7 Summary

The HHG source complements tr-momentum microscopy in the EUV to soft X-ray regime at FLASH, for which the HEXTOF momentum microscope is also used [22]. The combination of the versatile and highly efficient ToF momentum microscope HEXTOF with the tuneable HHG source enables unique PES measurement techniques, which otherwise are only available at large scale facilities. We used a graphene on iridium sample to benchmark the setup. The momentum field of view is large enough to map easily more than the first Brillouin zone with all six Dirac cones at the K points at once. The discrete tuneable wavelength in the range from about 24 eV to 46 eV allows to probe at different k_z values in an interval of $1\,\text{Å}^{-1}$ in the second Brillouin zone of Ir. We demonstrated 3D Fermi surface tomography with a table-top EUV source. Such measurements require usually a synchrotron. The setup has a time resolution of 95 fs. With the settings for a momentum field of view of $\pm 2.4\,\text{Å}^{-1}$ we could estimate an energy resolution of 96 meV and a momentum resolution of $96 \times 10^{-3}\,\text{Å}^{-1}$, which includes the spatial resolution of the eight-segment DLD. The field of view was limited by the acceptance angle of the used settings.

The spatial and temporal resolution of the eight-segment DLD can be improved by a factor of $\sqrt{2}$ if only double counted electrons are taken into account. To achieve this, a modification is required for the data read-out routine. The routine must filter the events of each pulse for pairs. This is a straightforward process for two events per pulse, but it becomes computationally intensive with increasing numbers.

This setup can combine the 3D Fermi surface tomography with ultrafast time resolution. Due to the low intensities for the edges of the spectral range, this probably requires compromises in the pump-probe delay range. Instead of scanning a longer pump-probe delay range, only two or three pump-probe delay steps can be measured in a reasonable measurement time. The missing variable gap undulator at FLASH I and heavily limited measurement time restrict the PG2 beamline to only a few different photon energies per experiment. In the future, full control of the wavelengths and high intensity for all wavelengths will be provided by the upgraded PG2 at FLASH I, the FL 23 beamline at

FLASH II, the SASE3 beamline at XFEL or the soft X-ray beamline of LCLS II.

5 The robustness of the topological surface state of bismuth selenide

In the last years, the field of topological materials gained popularity in the scientific research community. Topological materials are quantum materials whose properties are defined by topology. One of the most prominent representatives is the class of topological insulators, which show an insulating behavior in the bulk, while the surface is electrical conducting. This conducting surface state is protected by time-reversal symmetry, making it robust. This means that even if the surface is subject to destructive changes, the surface state will remain unchanged [113–115]. The spin orientation of the surface state is locked, which suppresses Umklapp scattering and increases conductivity. These properties make topological insulators a promising candidate for spintronics and quantum computing [53, 116, 117]. In this chapter, we will report our findings on the ultrafast dynamics and robustness of the 3D topological insulator bismuth selenide (Bi_2Se_3).

5.1 Topological insulators

The band structure of an insulator has a band gap at the Fermi level. In the ground state occupied and unoccupied states are separated by this gap. Insulators can be classified by the topology of the band structure. The topological classification is linked to different topological invariants. In topological materials with strong spin-orbit coupling like quantum spin Hall materials and 3D topological insulators, the Z_2 invariant protects the topological state [118, 119].

From a mathematical point of view, two objects are topologically equal if there is a continuous deformation to transform one into the other. The analogy in band theory to the continuous transformation is here an adiabatic change of the Hamiltonian. No adiabatic transformation allows for the closing of the band gap. However, a transition from a topological insulator to an ordinary insulator is only possible by closing the band gap. The reason for this lies in the energetic order of the orbitals involved in the band structure. Due to strong spin-orbit coupling in topological insulators, the *s* orbital attracted by the relativistic potential is energetically pulled below the *p* orbitals. The

energetic order of the levels is inverted with respect to their normal order of the related atomic levels at high symmetry points in the Brillouin zone around the Fermi level [120, 121]. At the interface of a topological and an ordinary insulator, the continuity of the Bloch wave functions must be preserved. Therefore, at some point along the surface, the distinct bands from both materials must be connected. As a consequence, the surface state is closing the band gap and enables metallic conductivity [119, 122, 123].

There is a close relationship between 2D topological insulators and the quantum spin Hall effect. In quantum spin Hall materials such as a thin layer of HgTe surrounded by CdTe, a spin-up and a spin-down polarized current flows along the edges in opposite directions. Despite the non-existence of the Hall effect in three dimensions, a generalization of the quantum spin Hall effect has been developed for three dimensions [119, 124, 125]. 3D topological insulators are characterized by the Z_2 topological invariant, which requires time-reversal symmetry of the band structure in 3D materials. Consequently, the surface state is characterized by an odd number of Dirac cone per Brillouin zone. The surface state has spin texture and massless electron dispersion at the Dirac points. Electrons can travel only in one direction along the surface, because the movement of the spin current is attached to the electron spin. This protects the electrons of the surface state against backscattering at non-magnetic defects and strengthens the surface state's robustness. A detailed overview on topological insulators is given in reference [113].

Kastl *et al.* [126] have demonstrated that pumping a topological insulator with circularly polarized light can generate ultrafast charge current pulses originating from the laser-generated spin polarization in combination with the strong spin-orbit coupling. Applying a charge current to a topological insulator allows for current-induced spin polarization [127]. Several time-resolved experiments on topological insulators have been performed in the past [54, 128]. Pumping with circularly polarized light can cause the creation of spin-polarized photocurrents [129, 130]. The carrier excitation and recombination experiments using weak pump pulses show the coupling between the topological surface state and the bulk states [131, 132]. The coupling can be altered by increasing the pump fluence in the range of 0.1–1 $\frac{\mathrm{mJ}}{\mathrm{cm}^2}$. The observed alterations of the coupling between the topological surface state and the bulk states already indicate that the description in a perturbative way is no longer valid. We investigated the electron dynamics of the topological insulator for strong pump excitations. It can be expected that the topological surface state cannot simply be destroyed by the strong pump pulse. The topological surface state must be located somewhere, since the topological properties are not altered by the pump. It has been reported that disorder of the surface can decrease sharpness for the ARPES signal, but the topological surface state is not vanishing [133, 134].

5.2 Bismuth selenide

Bi_2Se_3 is one of the prototypical 3D topological insulators. Its topological insulating character was predicted by Zhang *et al.* [123] and experimentally proven with ARPES measurements by Hsieh *et al.* [120]. Because ARPES probes directly the unique metallic surface state and with it the topological invariants, ARPES is one of the favored methods to investigate 3D topological insulators and their behavior. The surface state of Bi_2Se_3 has one Dirac cone at the Γ point connecting the bulk conduction band with the valence band.

Bi_2Se_3 is a layered material, where the layers are bound together by van der Waals-type binding. Each layer is a quintuple layer of five atomic layers with the order Se-Bi-Se-Bi-Se. Due to the hexagonal growth of each atomic layer, a rhombohedral crystal structure with five atoms per unit cell is formed. This structure has a three-fold rotation symmetry in the plane of the layers and a two-fold rotation symmetry in the vertical direction.

5.3 Mapping the band structure of Bi_2Se_3

To map the band structure of Bi_2Se_3 and its dynamics, the HEXTOF setup was used in combination with the HHG source as well as with FLASH. The HHG source was set up for the 23$^{\text{rd}}$ harmonic with a photon energy of 36.1 eV. The FEL was tuned to a photon energy of 55.5 eV, which is close to the binding energy of the Se 3*d* core levels. Due to the work function of 5.4 eV, the Se 3*d* core level electrons cannot be probed and did not contribute to the space charge, lowering the impact of space-charge effects [135]. At this energy, the measurement is highly surface sensitive. At both photon sources, the fundamental of the pump laser was used to excite the electronic structure of Bi_2Se_3. Under the angle of 22°, 80 % of the incoming *p*-polarized optical pump beam should be absorbed on Bi_2Se_3[136, 137]. The pump fluence was varied from $5.3\frac{\text{mJ}}{\text{cm}^2}$ to $11.9\frac{\text{mJ}}{\text{cm}^2}$.

We also have collected complimentary data at the ARPES endstation of the ASTRID2 synchrotron in Aarhus. The static measurements from ASTRID2 allowed for higher resolution and variable photon energy [138]. The static measurements at different photon energies give a hint of the changes in the photoemission cross-section of the different bands. The dependency of the surface sensitivity was mapped with a photon energy scan. To characterize the impact of the highly intense pump beam, a DektakXT stylus profilometer from the company Bruker was used to measure the depth profile of the sample surface additionally. All measurements were done at room temperature.

5.4 Surface state dynamics at high pump fluences

In the following, the behavior of Bi_2Se_3 at high pump fluences will be presented. An overview of the fluence dependencies on tr-ARPES measurements can be seen in Figure 5.1. Here, pump-probe data from FLASH [Figure 5.1(b1)-h2)], and from the HHG source [Figure 5.1(b3)-h3)], as well as the static measurements from ASTRID2 [Figure 5.1.(a1)-a3)] are combined. The static measurement in the first column of Figure 5.1(a1)-(a3) shows the different contributions of the surface and bulk components to the spectra, depending on the photon energy. At a photon energy of 55.4 eV, the topological surface state is dominant, while the bulk component is barely visible. However, at a photon energy of 36.1 eV, the bulk contribution is much stronger. Hence, the time-resolved measurements at FLASH with the photon energy of 55.4 eV represent mainly the dynamics in the topological surface state. The occupation above the Fermi level shows a similar temporal behavior for both pump fluences of 5.3 $\frac{\text{mJ}}{\text{cm}^2}$ and 10.0 $\frac{\text{mJ}}{\text{cm}^2}$, respectively. At t_0, the population of hot electrons appeared above the Fermi level, which quickly gather in the Dirac cone of the topological surface state and thermalize back to the ground state. At the higher fluence, the population of hot electrons is denser and persists longer. Due to pump-induced space charge, the effective energy resolution, especially for the 10.0 $\frac{\text{mJ}}{\text{cm}^2}$ measurement at FLASH, is significantly lower. The space-charge-induced energy shift is not visible because all energy axes are aligned to the Fermi edge.

For the pump-probe data, acquired in the HHG laboratory, a photon energy of 36.1 eV was selected and the absorbed fluence of pump laser was estimated to 2.8 $\frac{\text{mJ}}{\text{cm}^2}$. Because at this photon energy the measurement is also sensitive to the bulk states, the time-resolved data show also the dynamics of the bulk conduction band. In addition to the filling of the Dirac cone at t_0, there is an increased occupation slightly above the Fermi level that appears with some delay after t_0.

Ultrafast dynamics on a ps time scale have been reported in the topological surface state as well as in the bulk states at pump fluences in the $\frac{\mu\text{J}}{\text{cm}^2}$ regime [54, 131, 139]. Sobota *et al.* [54] explained the dynamics for lower fluence with several intermediate steps. The excited electrons first populate, via a direct optical transition, a higher unoccupied bulk state. From there, the electrons scatter into the topological surface state either directly or with a further intermediate step via the bulk conduction band, where they thermalize and then scatter into the topological surface state. The hot electrons in the topological surface state relax back into the initial state.

Looking into the momentum-resolved evolution of the excited electrons, we get a closer inside into the dynamics. Comparing these findings with the ARPES spectra measured with the HHG source (see Figure 5.2), we find a similar behavior at high fluence. First, the electrons are excited by the optical pump pulse into higher unoccupied states (area 1, blue) and scatter from there fast either into the topological surface state

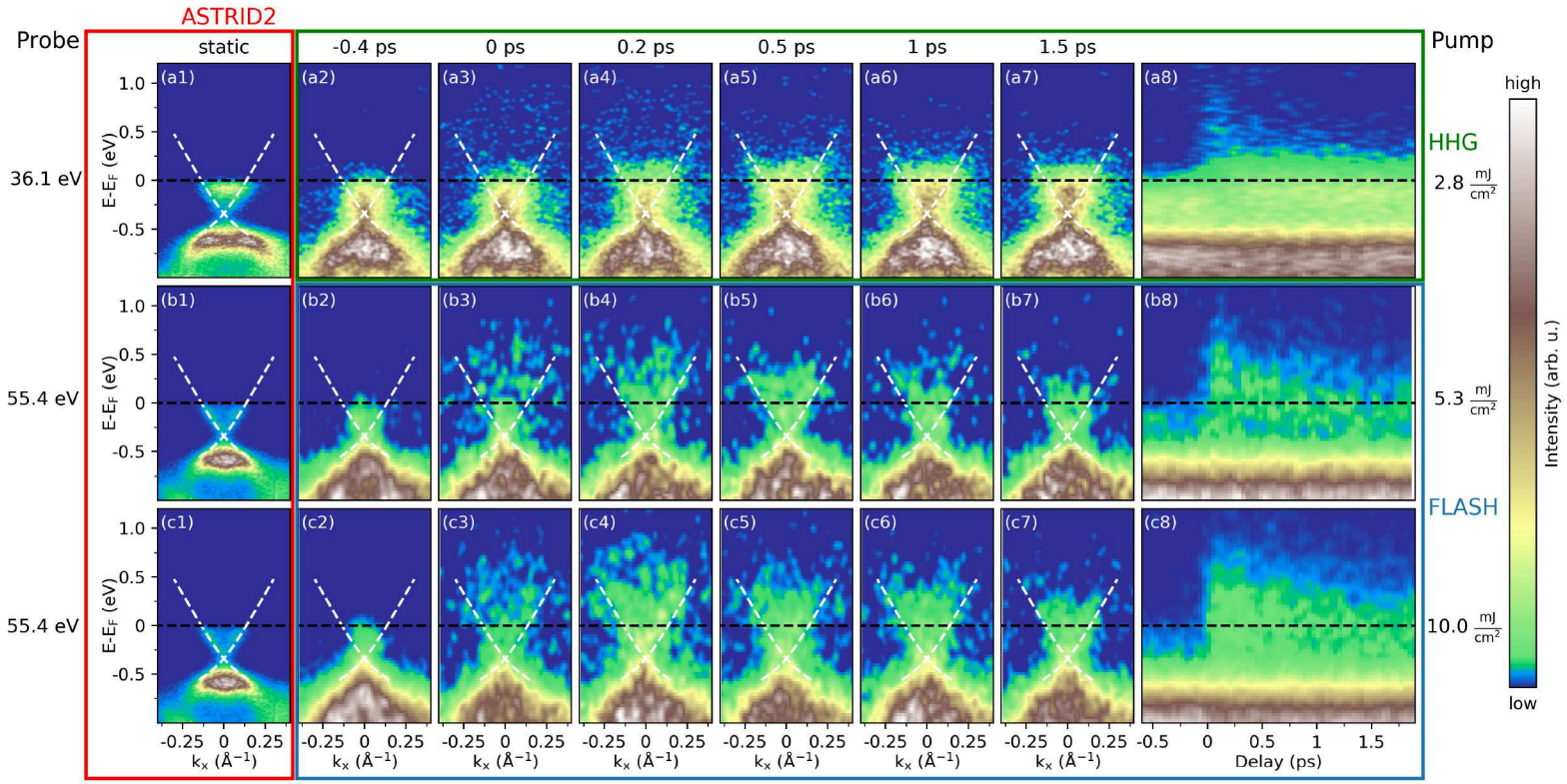

Figure 5.1: Maps of the photoemission intensity distribution of Be_2Se_3 at photon energies of 36.1 and 55.4 eV. This is a combined overview of static (ASTRID2) and time-resolved measurements (HHG and FLASH). Left column (a1-c1) shows the static high-resolution energy-versus-momentum maps of the topological surface state measured at ASTRID2. Columns 2 to 7 display time-resolved results at differnt pump-probe delays from -0.4 ps to 1.5 ps. The upper row (a2-a7) refers to the measurements with the HHG source at the pump fluence of $2.8\,\frac{\mathrm{mJ}}{\mathrm{cm}^2}$. The middle (b2-b7) and bottom (c2-c7) rows refer to time-resolved measurements at FLASH with $5.3\,\frac{\mathrm{mJ}}{\mathrm{cm}^2}$ and $10\,\frac{\mathrm{mJ}}{\mathrm{cm}^2}$ pump fluence, respectively. The right column (a8-c8) shows the corresponding time evolution maps of the momentum-integrated photoemission spectrum. The general trend is the same in all three measurements, where hot electrons appear above the Fermi level. The electrons are gathering in the Dirac cone and relax back to the initial state. At higher pump intensities, the number of hot electrons increases and the relaxation rate slows down sightly. In the data from the HHG source, also the dynamics of the bulk conduction band are notable. The white dashed lines on the ARPES intensity maps serve as a guideline for the Dirac cone.

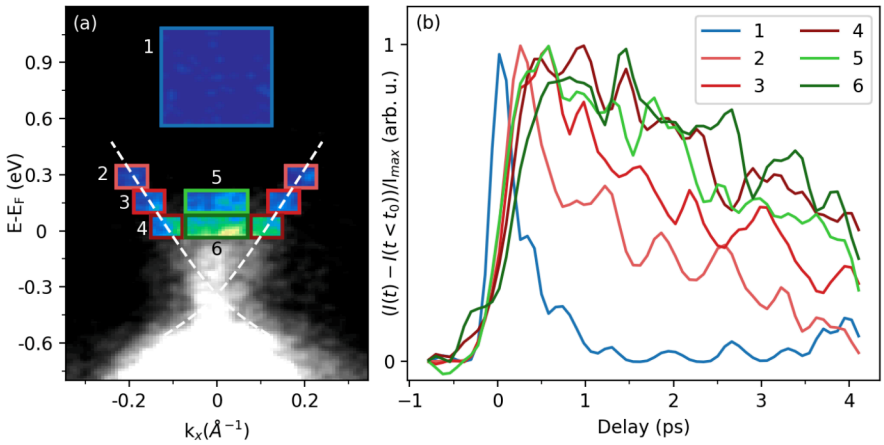

Figure 5.2: Momentum-resolved electron dynamics measured with the HHG source at 36.1 eV photon energy and a pump fluence of 2.8$\frac{\text{mJ}}{\text{cm}^2}$. (a) ARPES measurement of the Dirac cone with the indication of different regions of interest. (b) Temporal evolution of the photoemission intensity in different regions of interest. Area 1 (blue): Region of the higher unoccupied bulk state. Areas 2-4 (red): Regions along the topological surface state. Areas 5 and 6 (green): Regions of bulk conduction band.

or the bulk conduction band. The population in the topological surface state (areas 2-4, red) decays quickly to the ground state, especially the occupation of area 2. The scattering into the bulk conduction band is slower. The electrons in the bulk conduction band decay slowly via the topological surface state back to the ground state, which feeds the topological surface state at lower binding energies for some time (areas 3 and 4). The overall dynamics are faster than described by Sobota *et al.* [54], because of the doping of the sample. The dynamics in a p-type sample are slower than in an n-type sample [139]. In our case for an n-type sample, it takes about 0.6 ps to get the maximum occupation of the bulk conduction band, instead of 2 ps for the p-type sample as reported by Sobota *et al.* [54]. The momentum-selected data at higher fluence from FLASH are not shown here, but the dynamics of the electrons in the topological surface state show a similar behavior. Due to the low cross-section, the dynamics in the bulk bands are not directly visible and the lower resolution allows only for a rougher momentum selection.

Using the 3^{rd} harmonic of FLASH allows us also to inspect the dynamics of the core levels. HEXTOF was set up to get the Se 3*d* level into momentum focus. With these settings also the faster electrons from the Bi 5*d* core levels and the valence band are detected, but with the following compromises. For the faster electrons, the energy resolution is reduced, and the momentum information fully gone. A comparison of the temporal behavior is shown in Figure 5.3. Figure 5.3(a) presents the momentum-integrated EDC of the unpumped sample before t_0 and the EDC at t_0. At temporal

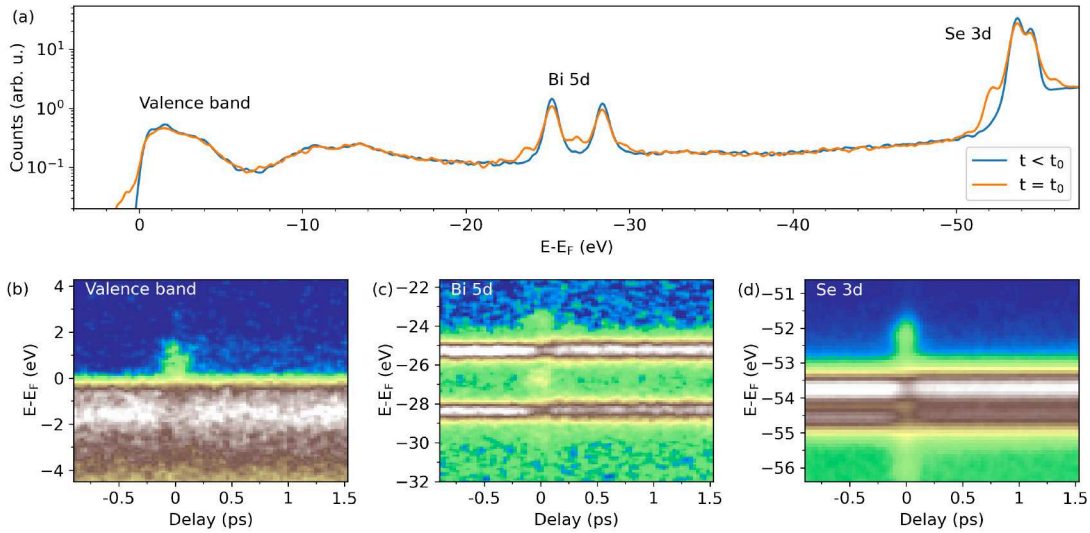

Figure 5.3: Comparison of the pump-probe dynamics in the valence band and in the Bi 5*d* and Se 3*d* core levels, recorded with the third harmonic of the FEL at a photon energy of 188.2 eV. The sample was pumped with fluence of 7.4 $\frac{\text{mJ}}{\text{cm}^2}$. (a) Overview of momentum-integrated EDC of Bi_2Se_3 before t_0 (blue) and at t_0 (orange) over a binding energy range from 5 eV to −58 eV. Bottom row (b-d): Time evolution of PES spectra for the valence band, the Bi 5*d* and Se 3*d* peaks, respectively. In all three regions, the LAPE effect is noticeable at t_0, and afterwards some longer lasting dynamics, as depicted in Figure 5.2.

overlap, additional peaks next to the core level can be found as well as above the Fermi level. The additional peaks are separated from the original peaks by about 1.5 eV. On the other hand, the intensity of the original peak decreases slightly. All of this is pointing to the laser-assisted photoemission (LAPE) effect. A more detailed view of the temporal evolution can be found in Figures 5.3(b-d) for the valence band, the Bi 5*d*, and Se 3*d* core levels, respectively. In the valence band, besides the LAPE signal, we also see some remaining intensity of the persistent excited states after t_0. The core levels shift to lower binding energies and also broaden. For a quantitative analysis, the spectrum of each time slice is fitted. A Voigt profile is used to fit each core level, and additional peaks are included around t_0 to account for the LAPE effect. As shown in Figure 5.4, the result is, first, in general a persistent broadening of about 100 meV and, second, an energy shift of about 50 meV to lower binding energies after t_0. This is valid for all core levels, except of the broadening for the Se $3d_{3/2}$, which is only half the size with 50 meV. A deeper analysis of the core-level dynamics, including tr-X-ray photoelectron diffraction (XPD) of this sample, was performed by Curcio *et al.* [140].

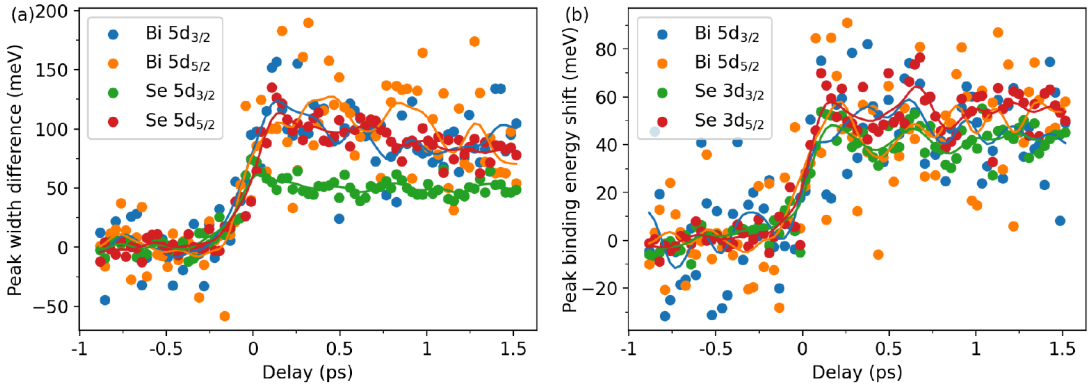

Figure 5.4: Dynamic of the core-level emission. The line shape of both pairs of *d* core levels are fitted for each time delay. The temporal change in peak width is represented in (a) and the shift of the peaks in binding energy in (b).

5.5 Robustness of the surface state

The surface of the sample was monitored using the PEEM mode of the momentum microscope both prior to and after each change in pump fluence. As a result of the pump-probe measurements at the highest fluence of 11.9 $\frac{\text{mJ}}{\text{cm}^2}$, the surface showed some structural changes, as can be seen in the PEEM image [see Figure 5.5 a)]. This image was acquired by using the Hg lamp to illuminate the sample surface. The intensity variation corresponds to a variation in the work function. A larger elliptic area with several small spots, which all were not visible before the measurements, result from the high-fluence laser excitation. The position, orientation and the size of the damaged region fits well to the photon footprint of the pump beam [see Figure 5.5 b)] acquired on the flat sample surface. The damage on the sample appeared after 4 hours of measurement with the laser fluence of 11.9 $\frac{\text{mJ}}{\text{cm}^2}$.

To determine the character of the damaged area, a freshly cleaved sample was investigated using the pump branch of the HHG source. For this, the pump beam was focused down to a size of $95 \times 155\ \mu m^2$ and the pump fluence was gradually increased from 14.1 $\frac{\text{mJ}}{\text{cm}^2}$ up to 46.4 $\frac{\text{mJ}}{\text{cm}^2}$ in eight steps, exposing the sample for 5 minutes per step. The surface of the sample was monitored using the PEEM mode of the momentum microscope prior and after each change of the pump fluence. The first change of the surface appears at 29.3 $\frac{\text{mJ}}{\text{cm}^2}$. The damaged area was still slightly smaller in diameter, but at 33.5 $\frac{\text{mJ}}{\text{cm}^2}$ grown to full size. The resulting damage on the sample is presented in Figure 5.6. It is visible on the sample surface in the PEEM mode under Hg-lamp illumination [see Figure 5.6(a)], as well as with an optical microscope [see Figure 5.6(b)]. The vertical profile of the surface, measured with the stylus profilometer, confirms the partial removal of the material after the laser excitation. A hole with a depth of 2.5 µm and

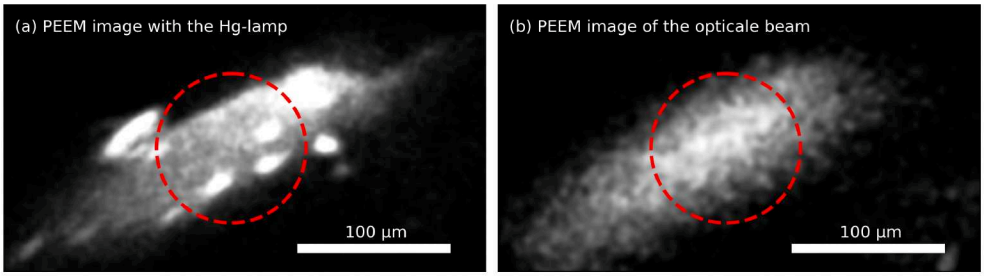

Figure 5.5: (a) PEEM image of the structural changes which appeared on the surface after the high fluence measurement at FLASH. The sample is illuminated homogeneously with a Hg lamp. The spatial intensity distribution is related to the variation of the work function on the surface of the sample. (b) PEEM image with the optical spot illuminating the flat sample. Its position is overlaying well with the structure on the surface. The red dashed circles indicate the position and size of the region of interest on the sample, defined by the field aperture of the momentum microscope used during the ARPES measurements, selecting only electrons from this area.

$120 \times 200\,\mu m^2$ was created. The profile measurement shows also an increased roughness in the damaged region, which explains the homogeneous brightness of this area in the optical microscope by diffuse reflection of the light.

In comparison, the maximum fluence at FLASH was much lower than that of the Ti:Sa laser used in the HHG source. The damage at FLASH also exhibits more structured features. The longer exposure time at FLASH may have compensated for the lower fluence, resulting in conditions that were only slightly above the damage threshold. Therefore, we observe damage occurring at various positions. For high fluence, the spot is saturated, resulting in a more uniform change in the surface.

It is interesting to note that apart from obvious changes in the surface structure, the ARPES measurements do not show any significant change in the electronic structure, not even in the surface compound. As seen in Figure 5.7, all three measurements of the Dirac cone show similarities. The first and the last one, which were measured before and after the hole appeared, were taken under the same conditions. Beyond statistical noise, these two measurements show no significant differences. Only the middle measurement with higher fluence is more blurred. This variation can be explained by broadening caused by the space charge. The fact that, after the hole appeared, the momentum distribution curve neither was shifted in momentum nor the background had increased, meant that the crystal orientation is preserved, because the emission angle of the Γ point remained unchanged. From this, we can exclude reordering of the crystal structure by melting and strong surface disorder. It seems to be more likely that the laser is creating

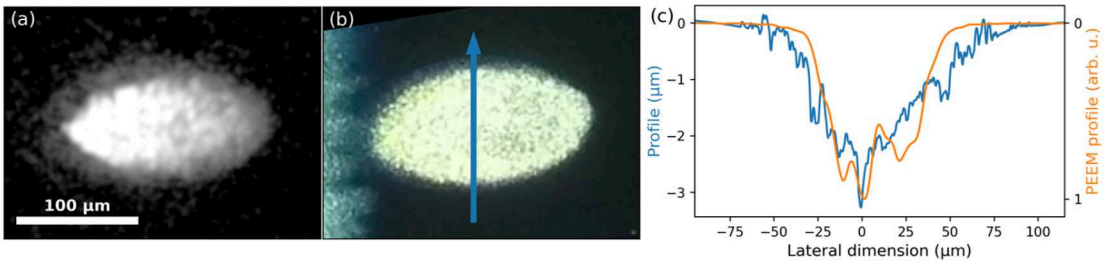

Figure 5.6: Characterization of the damaged sample area suffering from the very high fluence of the pump beam. (a) PEEM image of the surface. (b) Optical microscope image of the same area. The bright vertical structure along the left edge on the sample was exposed to the intense beam after the PEEM image was taken to find the damaged region. (c) Vertical profile (blue) measured with the stylus profilometer along the direction of the arrow indicated in (b) and the corresponding intensity (orange) taken from the PEEM image.

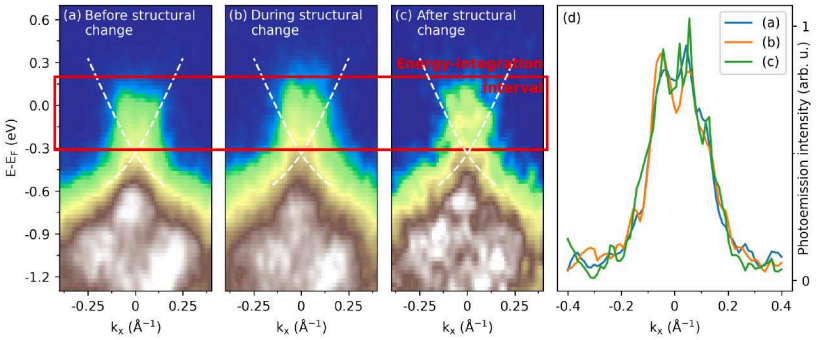

Figure 5.7: Three consecutive ARPES measurements of the Dirac cone. Presented are photoemission energy-versus-momentum intensity maps integrated over a few 100 fs before t_0. (a) First measurement with a pump fluence of 10 $\frac{\text{mJ}}{\text{cm}^2}$, before the sample surface structure changed. (b) High fluence measurement with 11.9 $\frac{\text{mJ}}{\text{cm}^2}$, during which the sample surface structure changed. (c) Second measurement with a pump fluence of 10 $\frac{\text{mJ}}{\text{cm}^2}$, after the sample surface structure changed. Due to the shorter measurement time and an intensity decrease of the FEL, the total number of detected electrons is more than five times lower compared to any of the other two. (d) Corresponding MDC of the Dirac cone for the three measurements integrated in energy over the area indicated in (a-c).

a hole by removing layer by layer, while preserving the topological surface state.

5.6 Summary

In conclusion, the high pump fluence trARPES measurement on Bi_2Se_3 showed a dynamics on the several hundred fs to few ps time scale in the bulk conduction band and in the Dirac cone of the topological surface state, which connects the bulk conduction band with the bulk valence band. In comparison to the low fluence measurement, the dynamics of the electrons in the surface state and the bulk conduction band did not change their character. The core-level dynamics of the Se 3*d* and Bi 5*d* peaks appeared to be slower. We could show that an absorbed fluence of 11.9 $\frac{\mathrm{mJ}}{\mathrm{cm}^2}$ is sufficient to damage the surface of Bi_2Se_3 and material was removed. Even at high fluences beyond the damage threshold, the surface state stayed intact. The laser removed Bi_2Se_3 layer by layer and did not melt or reorder the crystal structure.

6 Ultrafast electron dynamics of the mixed-valence system thulium selenide

When the Coulomb interaction between electrons in the outermost shell in many-body systems can no longer be considered weak, our intuitive single-particle picture of free electrons in Fermi gas theory will deviate from our observations. However, Landau proved that the complex problems of many electrons can be simplified into a quasiparticle picture with heavy mass when the low-energy excitations happen in the vicinity of the Fermi surface [141]. Thus, we can keep a single-particle perspective to some extent. One such heavy-fermion system is the homogeneous mixed-valence system, which has continued to challenge condensed matter physics with intriguing problems [142, 143].

Furthermore, rare-earth compounds can be even more intricate as two distinct electron states coexist within their outermost shell. One state resembles nearly free-electron like conduction $5d6s$ states, while the other state derives from the strongly correlated $4f$ states. These two electronic states interact strongly in the homogeneous mixed-valence system, which will be discussed in detail in this chapter. Exotic composite quasiparticles, including neutrally charged excitons and Majorana fermions, have been proposed in these systems due to the interaction of opposite characters [55–59]. Subsequently, the $4f$ dynamics of the distinctive mixed-valence thulium selenide (TmSe) will be discussed.

6.1 Heavy Fermions

The best known heavy-fermion systems belong mainly to the Kondo regime of the Anderson model [144], which describes interactions between itinerant and localized electron states (see Equation 6.1). This localized state can be approximated by an impurity state in which an isolated electron can barely hop to neighboring sites. Such an environment is described by the Anderson impurity model shown below. This Hamiltonian can be transformed into the Kondo model when the spin fluctuation is dominant and the

charge fluctuation is frozen in the low energy scale [145]:

$$H^{And} = \underbrace{\sum_{k\sigma} \varepsilon_k c^\dagger_{k\sigma} c_{k\sigma}}_{\text{creation and annihilation}} + \underbrace{\sum_{kl\sigma} V_{kl}(c^\dagger_{k\sigma} f_{kl\sigma} + f^\dagger_{kl\sigma} c_{k\sigma})}_{\text{hybridization}} + \underbrace{H_{imp}}_{\text{impurity}} + h.c., \tag{6.1}$$

where $c^\dagger_{k\sigma}$ and $c_{k\sigma}$ are the second quantization fermionic creator and annihilator operators in the momentum representation for a conduction band electron, and $f^\dagger_{k\sigma}$ and $f_{k\sigma}$ represent the $k\sigma$ creator and annihilator for the f-electrons, whose spherical harmonic function of the l quantum number is projected onto the momentum k-basis. This basis has the same symmetry as the conduction states. Thus, there will be a remaining part of l^{th} spherical harmonic functions which are not hybridized with conduction bands, which are usually ignored in the Anderson model in general. D. Haldane and C. Varma claim that the standard Anderson model does not satisfy the Friedel sum rule. As a solution, the Anderson model was extended by an additional screening term [146], $H = H^{And} + H^{scr}$. However, the extent of the influence of this term on the physical properties is still debated.

The impurity term H_{imp} of the Hamiltonian describes the Coulomb interaction among f-electrons in a single impurity. It can be classified into interorbital (U) and intraorbital (U') interactions. The impurity term combines an orthogonal f-orbital term and additional electron-electron interactions. The magnetic impurity with multiple $4f$ electrons can be expressed in the following format:

$$H_{imp} = \sum_{i\mu} \varepsilon_f f^\dagger_{i\mu} f_{i\mu} + \frac{1}{2} \sum_{i\mu\nu} U_{\mu\nu} n^f_{i\mu} n^f_{i\nu}, \qquad U_{\mu\nu} = \begin{cases} U & \text{for } \mu = \nu \\ U' & \text{for } \mu \neq \nu \end{cases} \tag{6.2}$$

where i is the site index and μ, ν are the spin orbital indices. $f_{i\mu}$ is the creation operator for an electron in the f-orbital, ε_f is the energy of adding an electron to the f^{n-1} state, $n^f_{i\mu,\nu}$ is the number operator, and $U_{\mu\nu}$ is the interaction energy.

This model adequately describes rare-earth or actinide compounds with partially filled $4f$ or $5f$ localized orbitals, as well as broad $5d6s$ and $6d7s$ conduction bands. In the Kondo regime, the screening of the magnetic moments of the f-electrons is induced by the hybridization of the conduction band electrons with f-levels [147].

The Kondo effect discovered in the early 1960s refers to this screening mechanism [148, 149]. The f-electron's local magnetic moment polarizes the conduction band electrons. Below a material-specific temperature T_K, known as the Kondo temperature, the local moment is completely screened. If the local magnetic moments are closely packed in a crystalline lattice, the screening effect from different sites may overlap and result in the formation of a heavy-fermion band [147].

In the Anderson model, the hybridized bands are composed of the conduction d-states and the f-states, which are the origin of the quasiparticles. As a result of the hybridization, the bandwidth of the conduction band is reduced, thereby leading to a significant

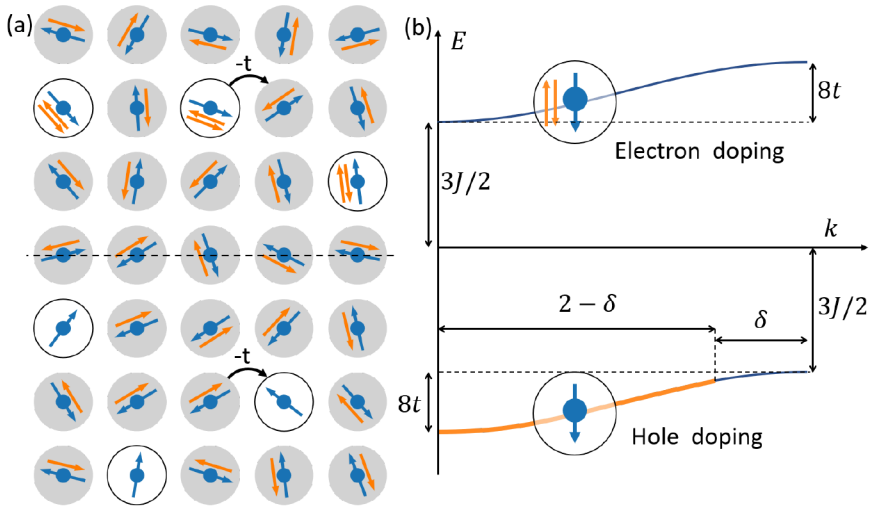

Figure 6.1: (a) Simplified electron configuration of a strong-coupling Kondo insulator. The localized f-electrons (blue arrow) and the conduction-band electrons (orange arrow) create a quasiparticle. Electron doping is illustrated in the upper half and hole doping in the lower half. (b) The dispersion of strong-coupling Kondo insulator is depends on the Kondo coupling J and the hopping integral t. A small amount of hole doping δ gives rise to a large Fermi surface containing $2-\delta$ heavy electrons. Adapted from [145]

increase in the effective mass of the conduction-band electron states. The effective mass is several orders of magnitude larger than m_e. When each free electron is paired with an f-electron, i.e., the Fermi level lies between two hybridized bands, the system becomes a Kondo insulator. A schematic illustration is given in Figure 6.1. Many-body systems have a distinct feature where the energy gap is defined by the sum of the ionization energy and the electron affinity energy, i.e., the lowest energy it costs to add or remove an electron from the ground state. As shown for Bi_2Se_3 (see Section 5.2), where the one-electron picture holds, the energy gap can be defined by the energy separation between the valence band maximum and the conduction band minimum. This assumes that any missing or additional electrons resulting from the PES or inverse photoemission spectroscopy (IPES) processes do not intervene with the electronic ground state. These electrons are barely correlated with other electrons because free electrons in the solid will screen the additional hole and electron. However, for the strongly correlated systems, removed and added electrons change the correlation energy because the N-electron system becomes $N-1$ and $N+1$ (see section 6.2 for more details).

Figure 6.2 represents the importance of the one-electron removal and addition spectral functions when dealing with the strongly correlated $4f$ electron systems such as the Kondo insulator. A Kondo insulator is a very peculiar state that appears only when

each conduction electron is paired with each local moment and can be considered as the mother compound of the heavy-fermion systems. When an excess or deficiency of conduction band electrons occurs, as shown in Figure 6.1(a), the Fermi level shifts and can cross either the single-particle removal or addition spectral functions, which can be considered as an excess of electron or hole carriers. Since the d-electrons contribute to the conduction band, they can hop from one site to the neighboring site as defined in the Kondo model [145]. As the localized $4f$ states are hybridized with the conduction electrons, it can be imagined that the paired electrons show a dispersion similar to the conduction bands. However, the bandwidth is significantly reduced, as shown in Figure 6.1(b). It is not the simple dispersive conduction electron band, but the group of electrons composed of two conduction electrons and one $4f$ electron has dispersion as shown in (b) with the additional electron case, thereby exhibiting heavy effective mass.

6.2 Spectral function of correlated electrons in a rare-earth atom

For strongly correlated electron systems, the photoemission and inverse photoemission processes lead to the excitation of the electron system with various final state configurations with total electron number of $N-1$ or $N+1$, respectively. Due to strong spin-orbit coupling, as well as different inter- and intraorbital Coulomb interactions among $N-1$ ($N+1$) $4f$ electrons, multiple final states exist at different energies above 10 eV [150]. As a result, the one-electron-removal (addition) spectral function shows a characteristic multiplet structure.

Here, we will briefly revisit the H_{imp} term in the Anderson model, which is basically the same as the Hubbard model. Therefore, there are no separate conduction electrons. Here, as the hopping term is negligible, the impurity term can be considered to be a constant kinetic energy term (ε_f), leading to no band dispersion. It is worth noting that $|\varepsilon_f| < U$ typically ranges from approximately -2 eV to $+7$ eV.

As depicted in Figure 6.2, we consider as an example only three $4f$ electrons per site with two energy levels each. According to H_{imp}, we have zero energy when there are no electrons. Note that here the Fermi level is not the energy reference and that the Fermi level is not at zero energy. In this model, the Fermi level is defined as the point between the PES and IPES peaks that are closest to each other. When the number of electrons increases, the total energy of the system increases as well. For example, with one electron per site, the total energy is $E_{tot}(=E^N_{GS}) = Z*\varepsilon_f$, where Z is the number of sites and N is the total number of electrons. This energy scale changes dramatically when the occupation number per site is greater than 1. If $n_f = 2$, $E_{tot} = Z*(2*\varepsilon_f + U)$, and if $n_f = 3, E_{tot} = Z*(2*\varepsilon_f + U + U')$.

By the definition of the single-particle Green functions [151], the peak position in

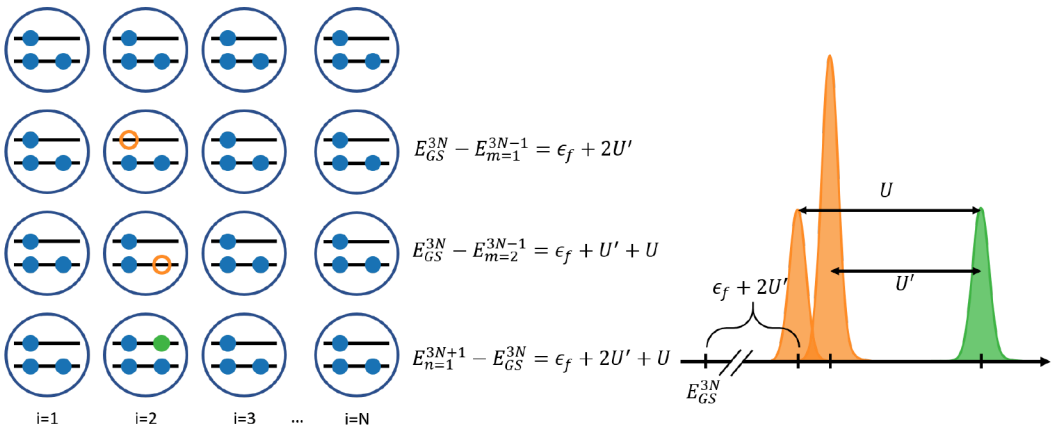

Figure 6.2: Example of a partially filled f-level system with three electrons in two orbitals per site. The ground state is depicted in the first row. A photoelectron can be removed either from the single-occupied orbital (2^{nd} row) or from the double-occupied orbital (3^{rd} row). The corresponding final states differ in energy, resulting in two peaks (orange) in the PES spectrum as illustrated on the right. The bottom row shows the option of inverse photoemission spectroscopy, where an electron is added.

PES spectra lies at $E_N - E_{N-1}$ and $E_{N+1} - E_N$. Thus, with PES (IPES), we are observing the transition from ground states to excited states for strongly correlated electron systems, whereas the static PES of band materials, such as Bi_2Se_3, gives the band structure at the ground state. So, in the ground state of our example in Figure 6.2, one level is fully occupied with two electrons, while the other one is occupied by a single electron. By the PES process, two different PES final states can be reached: In the first case, the electron from the half-occupied level is removed, which costs us the kinetic energy of the removed electron and two interorbital interactions. In the second case, an electron is removed from the full-occupied level. Therefore, besides the kinetic energy, both an intra- and an interorbital interactions are required. However, in our example for the IPES process, there is only the option per site to add an electron to a half-occupied level. This electron will interact with the three other electrons at that site. After the IPES process, we end up with a total energy of $E_{tot} = E_{GS}^{n} + \varepsilon_f + U + 2U'$. The peak intensity is proportional to the number of possibilities to reach the same final states. In our example, the second case is more likely because there are two possibilities to remove an electron resulting in the same final state.

As shown in this simple model, the energy difference between two PES peaks represent the origin of the multiplet, which originates from different Coulomb interactions among $4f$ electrons. This model does not consider spin-orbit interaction, but each peak should be separated into spin-orbit-split peaks if we consider the interaction. With this

study, we also confirm that each PES peak represents a different final state, e.g., for the PES case, it is equivalent to a specific photohole. Thus, we can expect different dynamics for each multiplet peak if pumping induces different decay processes of the photohole states. In our study using NIR pump and FEL probe pulses, we basically observe how these photohole states decay differently from other multiplet states.

6.3 Homogenous mixed valence

Some rare-earth compounds, such as Sm, Eu, Tm, and Yb compounds, have shown a non-integer valence or intermediate valence [152, 153]. These rare-earth elements have in common nearly half-filled ($4f^6$) or full-filled ($4f^{13}$) $4f$ states. The term "homogeneous mixed valence" lacks a consistent definition in the literature. However, for the purpose of this thesis, we will limit it to the $4f$ occupation number of near half-integer values, meaning the valence falls between two integer values.

Based on the Anderson model, there are two ways to get such a half-integer value for the valence. Firstly, high hybridization strength can induce such a valence, but the strength is proportional to the distance between two rare-earth ions, which is typically in the order of magnitude of less than 0.1 eV in a solid. The conduction $5d6s$ bands usually have strong d-orbital character due to discrete lattice symmetries. Hence, in the following, the $5d$ states represent the conduction states. Since the wavefunction of the $4f$ and $5d$ orbitals are orthogonal at the same site, these orbitals cannot hybridize. However, the $4f$ orbitals can weakly hybridize with the extended $5d$ wave function of the neighboring rare-earth atoms [154]. Therefore, we can only expect a small hybridization strength in a natural single crystalline system unless high hydrostatic pressure is applied. Secondly, the half-integer occupation can be realized when the spectral functions of PES and IPES lie at the Fermi level. This suggests that removing one $4f$ electron and inserting one $4f$ electron results in almost zero energy cost in mixed-valence compounds, leading to zero-energy gaps. However, considering the large energy scale of the Coulomb interaction U(U'), it will be hard to establish it. One possible solution is that the ground states should consist of two different occupation sets, i.e., f^n and f^{n-1}. This requirement can be met theoretically even in the absence of hybridization ($V_{kl} = 0$).

As discussed in the previous section, also the hybridized $4f$-$5d$ bands are flat, which emphasizes their localized character. Consequently, the $4f$ PES or IPES spectra appear as atomic multiplet structures. Since the occupation number has non-integer value, the multiplet spectrum should show two atomic spectra corresponding to the $4f^{n-1}$ final states ($4f^n + h\nu \rightarrow 4f^{n-1}$ + photoelectron) and to the $4f^{n-2}$ final states ($4f^{n-1} + h\nu \rightarrow 4f^{n-2}$ + photoelectron) [155, 156]. Similarly, inverse photoemission also shows two corresponding final states [157]. The photoemission final state $4f^n \rightarrow 4f^{n-1}$ and the inverse photoemission final state $4f^{n-1} \rightarrow 4f^n$ are situated close to the Fermi level [158]. Thus, two opposing excitations are present on either side of the

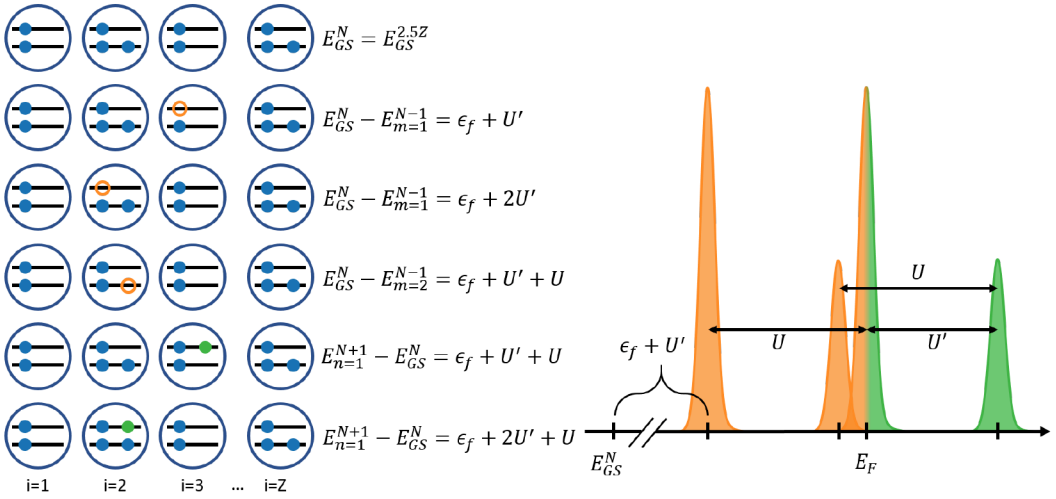

Figure 6.3: In a mixed-valence system, the $4f$ multiplet shows character of two atomic spectra. The given example has either two or three electrons per site, which results in three possible PES final states and two IPES final states.

Fermi level, resulting in no energy cost for the charge fluctuations of both $4f^n \rightarrow 4f^{n-1}$ and $4f^{n-1} \rightarrow 4f^n$. In other words, the ground state must ensure the presence of both electronic configurations, namely, the $4f^n$ and the $4f^{n-1}5d^1$ states.

With the simple H_{imp} model, the mixed-valence ground state is like a situation where the number of electrons at each side alternates between two values. As example, the cases with two or three electrons per site are depicted in Figure 6.3. This picture captures the inhomogeneous mixed-valence case since $4f$ occupancies vary at each site, but it is sufficient to describe the general spectral features due to the probabilistic quantum nature. One distinct characteristic of homogeneous mixed valence is the coherent peak, which appears only when the lattice coherence is established among rare-earth $4f$ states. In the homogeneous mixed-valence state, the $4f$ occupation number sites are identical at all sites. As a consequence, the phase of the $4f$ wavefunctions at neighboring sites can form a Bloch wave. Since the hybridization strength is relatively low-energy scale, the $4f$ states hybridizing with the $5d$ states of the neighbors can become coherent at low temperatures. As a result, the PES spectrum will show a sharp peak close to the Fermi level. However, above the coherent temperature T_{coh}, thermal perturbations become stronger than hybridization, and at a temperature $T > T_{coh}$ the $4f$ sites behave independently, which is basically identical to the incoherent mixed-valence systems.

6.4 The Tm monochalcogenides (TmS, TmSe, TmTe)

Tm monochalcogenides have very beneficial characteristics for investigating the interaction between the $4f$ and $5d$ states. Substituting chalcogen ions with S or Te, we can induce a change in the lattice constant, while keeping the fcc crystal structure.

TmS is an antiferromagnetic metal with nearly trivalent Tm ions, while TmTe is an antiferromagnetic semiconductor with nearly divalent Tm. TmSe shows an intermediate state, the mixed valence, composed of $4f^{13}$ and $4f^{12}$ configurations. TmSe has been proven to be a homogeneous mixed-valence system by showing two different multiplet structures in PES and IPES spectra [159]. Both contributions are confirmed: one from $4f^{12} \rightarrow 4f^{11}$ or $4f^{12} \rightarrow 4f^{13}$ (trivalent state) and the other from $4f^{13} \rightarrow 4f^{12}$ or $4f^{13} \rightarrow 4f^{14}$ (divalent state). While other mixed-valence compounds with Sm, Eu, and Yb are paramagnetic, the ground states are uniquely magnetic [158, 160, 161]. Namely, the total angular momenta of both divalent and trivalent $4f$ configurations of thulium compounds are non-zero. The outermost shell of anions corresponds to p bands, which are mostly fully occupied by two additional electrons from cations. Thus, the contribution of the different anions in the electronic structure is minimal since the p bands lie at least 2 eV below E_F. Moreover, the total number of electrons per unit cell stays $n_{tot} = 13$.

In the following, we will focus on Te-substituted TmSe. Te substitution will mainly expand the lattice parameter and drive the system from semimetallic to semiconducting. It has been shown in the thermal power measurement, that TmTe shows similar behaviors as TmSe when hydrostatic pressure is applied, until the lattice parameter reaches a similar value, while pressure is applied TmSe becomes similar to TmS [162–165]. Thus, replacing Se with Te induces almost only lattice expansion without disturbing the periodicity of the Tm ions or the total number of electrons per unit cell. Substituting Te for Se in TmSe acts like adjusting the lattice constant by applying static pressure inversely related to the Te concentration x. To study the evolution of the $4f$ dynamic properties while crossing the semimetal-semiconductor transition, $TmSe_{1-x}Te_x$ compounds are investigated for various concentrations x.

6.5 Previous static PES results on $TmSe_{1-x}Te_x$

For our experiments, single crystalline $TmSe_{1-x}Te_x$ samples were grown with the Bridgman method by collaborators in the group of Prof. Y. S. Kwon at DGIST, Republic of Korea. Hereby, the melt of Tm, Se and Te is solidified in a tungsten crucible at a temperature of 2500 K. To obtain a clean (001)-surface for PES measurements, the samples were cleaved at low temperature $T \leq 100$ K under UHV conditions. To

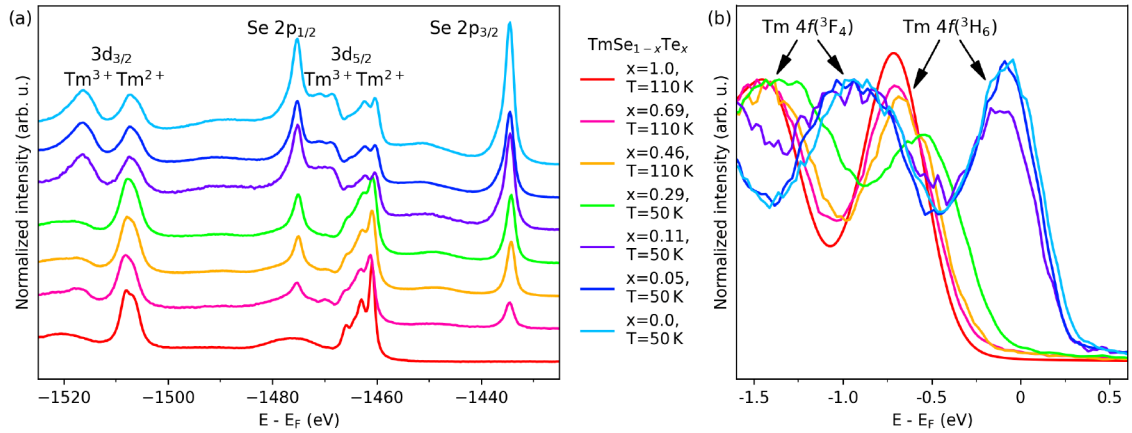

Figure 6.4: XPS spectra of $TmSe_{1-x}Te_x$ with varying Te concentration. (a) Tm $3d$ and Se $2p$ core levels and (b) the $4f$ multiplet at the Fermi level E_F. The Tm^{3+} core-level peaks in (a) vanish with the transition to the insulating phase at a Te concentration x of above 15 %. At this transition also the multiplet level shifts in (b). The $^3H_6$ peak shifts from close to the Fermi level ($E \approx E_F$) to $E - E_F = 0.7$ eV with the transition to the insulating phase.

this end, a post attached to the top of the sample was knocked off when the sample has already cooled down. Static XPS measurements were performed at the hard X-ray beamline P22 of PETRA III in Hamburg, Germany, and at the EUV beamline MERLIN of the ALS in Berkeley, California. [1]

To understand the impact of the Te concentration x on the electronic structure of the mixed-valence system, samples with different substitution values were investigated by static XPS measurements. Figure 6.4 depicts (a) the Tm $3d$ and Se $2p$ core levels and (b) the $4f$ multiplet near the Fermi level for varying Te concentration x. The spectra were recorded at PETRA III at a photon energy of 6 keV in order to be sensitive to the bulk properties. Figure 6.4(a) shows representative core-level spectra of $TmSe_{1-x}Te_x$, normalized with respect to the spectral weights of the $3d_{3/2}$ peak. Due to the mixed valence, the Tm $3d_{5/2}$ and $3d_{3/2}$ core levels of pure TmSe show a strong contribution of the Tm^{3+} valence in addition to the Tm^{2+} valence. These two valence states can be observed up to a Te concentration of $x = 0.11$. However, at $x = 0.29$, only the Tm^{2+} valence is strongly noticeable. Obviously, the Se $2p$ peak decreases with increasing the Te concentration, but it is always present in a single valence state.

The $4f$ multiplet lines $^3H_6$ and $^3F_4$ can be found near the Fermi level, as illustrated in the spectra of Figure 6.4(b). Each spectrum is normalized with respect to the $^3F_4$

[1] The static measurement campaigns were carried out by Chul-Hee Min before I joined the project for time-resolved measurements at FLASH.

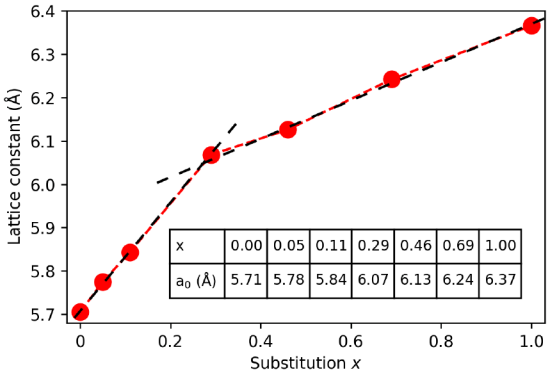

Figure 6.5: Lattice constant of $TmSe_{1-x}Te_x$ as a function of the substitution x. The lattice expands with increasing substitution x. The rate of the lattice expansion changes at a substitution of 29 %, which indicates the semimetallic to insulating phase transition.

peak. These multiplet peaks originate from the transition from the ground state to the one-electron-removal final state, i.e., the $f^{13} \rightarrow f^{12}$ transition as explained in Section 6.2. As the Te concentration x increases, the multiplet peaks shift to higher binding energies. The $^3H_6$ state appears for the samples with low x ($0.0 \leq x \leq 0.11$) slightly below the Fermi level ($E - E_F \approx -50$ meV), while the peak shifts below -0.5 eV for those samples with $x \geq 0.29$. Between TmSe ($x = 0$) and TmTe ($x = 1$), the energy difference in $^3H_6$ reaches a maximum (≈ 0.7 eV), which can be considered as a gap region. In strongly correlated electron systems, the energy gap can be defined by the energy difference between the lowest energy one-electron removal and the lowest single-electron-addition peaks, which are closest to the Fermi level. We note that the $^3H_6$ peak for $x \leq 0.29$ lies in the gap region. Moreover, the $^3H_6$ peak becomes broader up to $x = 0.29$, and gets narrower with increasing substitution ($x > 0.29$). As a result, the spectral weight of $x = 0.29$ is mostly in the gap region, indicating that it is indeed close to the transition point, which is also supported by the plot of lattice parameter versus Te concentration x in Figure 6.5.

To study the $4f$ multiplet in more detail, angle-integrated PES measurements with high energy resolution were performed at the high-resolution EUV beamline MERLIN of the ALS in Berkeley, California. In this experiment, a much lower photon energy of 110 eV was chosen because it not only gives much stronger surface sensitivity than at 6 keV photon energy, but has also the highest $4f$ photoionization cross-section [166]. To illustrate the presence of the coherent $4f$ states, which is the crucial evidence for the homogeneous mixed-valence state, temperature-dependent studies were performed.

Figure 6.6 shows the $4f$ multiplet spectra of the semimetallic sample ($x = 0.05$) at different temperatures. An overview of the $4f^{12}$ final state multiplet up to a binding energy

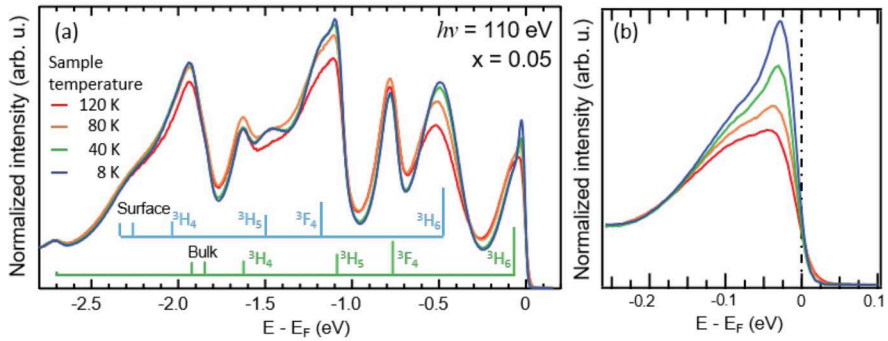

Figure 6.6: Temperature-dependent PES sepectra of the semimetallic ($x = 0.05$) sample close to the Fermi level E_F, measured at a photon energy of 110 eV. (a) Wide-range spectra of multiplet lines for the $4f^{12}$ final states including bulk and surface components. Surface peaks are shifted to lower binding energies. (b) Close-up of the $^3H_6$ peak at the Fermi level. At lower temperatures, a sharp peak rises next to the Fermi level. Courtesy of C.-H. Min.

of $E - E_F = -3$ eV is depicted in Figure 6.6(a). The spectra have been normalized to the intensity at the lowest binding energy. With the calculated multiplet positions [150], two sets corresponding to the f^{12} final states are observed with an energy difference of 0.5 eV. They are assigned as bulk and surface multiplet peaks, which is a very common feature in rare-earth compounds [167]. In Figure 6.6(a), they are marked with green and light blue bars, respectively.

With decreasing temperature, the $^3H_6$ bulk peak increases significantly in intensity and the peak width becomes narrower. It is still unclear why the $^3H_6$ surface peaks also narrow in this system. For a closer look at the $^3H_6$ peak, Figure 6.6(b) presents the spectra in the energy range from -0.25 to $+0.1$ eV. The $^3H_6$ feature clearly shows two peak components, a sharper peak from the coherent state near the Fermi level and a broader peak below $E - E_F \approx -0.4$ eV. High energy resolution ARPES studies demonstrate that the sharp peak arises from hybridization of the coherent $4f$ states with the $5d$ states of the conduction bands. In our investigation, the broader peak, the surface peak, and the $^3H_6$ peak in the insulating phase have similar peak widths, which might indicate similar origins. The influence of these different $4f$ peaks on the dynamics will be explored in the following section.

6.6 Picosecond $4f$ electron dynamics

To investigate the dynamics of the $4f$ multiplet, pump-probe measurements were conducted at the PG2 beamline at FLASH. The photon energy of the FEL was tuned to 112.6 eV to keep the measurements comparable to the high-resolution static data. The

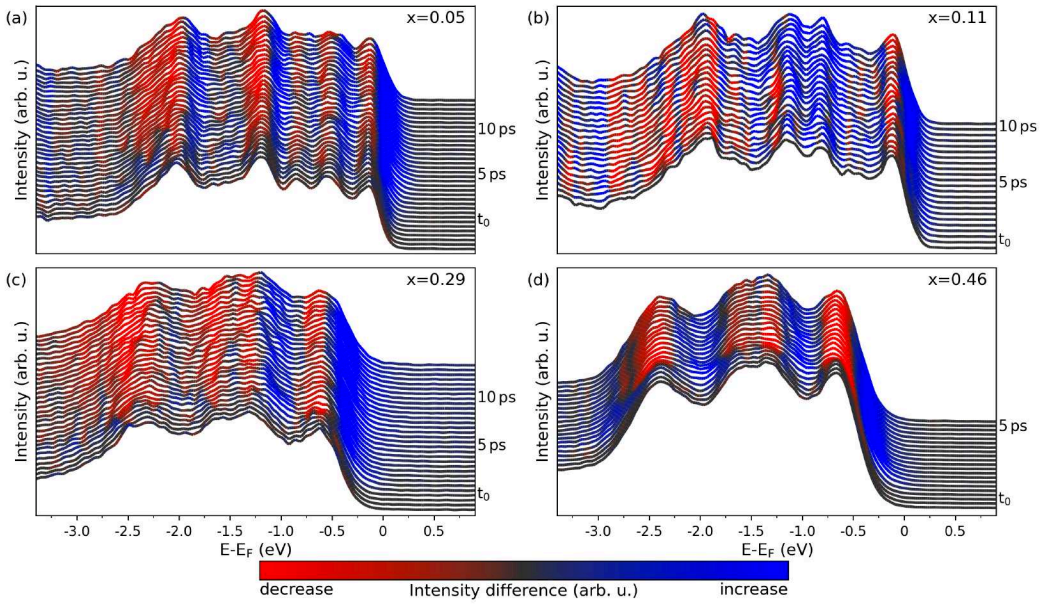

Figure 6.7: Time evolution of momentum-integrated EDCs of the $4f^{12}$ muliplet for samples with different substitutions x. From (a) to (d), the substitution x is increasing (0.05 - 0.11 - 0.29 - 0.46). The intensity difference to the spectrum before t_0 is color coded. Areas of intensity gains are blue and intensity losses are red.

WESPE setup was used due to its superior cooling capabilities. To reach sample temperatures in the range of 10 K to 20 K, the sample was cooled with liquid helium. The electronic structure was excited with the fundamental of the pump laser at a wavelength of 800 nm. The pump fluence was adjusted in the range of several hundred of $\frac{\mu J}{cm^2}$ to avoid strong space-charge effects.

An overview of the tr-PES measurements is shown in Figure 6.7. Each panel (a) to (d) represents a different Te concentration x of $TmSe_{1-x}Te_x$. The angle-integrated PES spectra of different pump-probe delays are plotted as a waterfall map. The temporal overlap of both pulses is marked as t_0. The absolute intensity changes of each spectrum with respect to the average spectrum before t_0 are coded in the line color.

In general, the peaks are broadened and depleted in intensity for all Te concentrations x at t_0. There is also an energy shift of the peaks to higher $E - E_F$. A direct optical excitation is not observed, since no spectral weight appears at t_0 or shortly after around several hundred meV above the Fermi level. The dynamics show a rather slow behavior. The depletion of the peak intensity lasts for several ps. At the base of the $^3H_6$ peak, a slight pedestal may develop in certain instances. For $x = 0.46$, the pedestal is observed right at t_0, whereas the $x = 0.05$ case shows a delayed pedestal at about 5 ps.

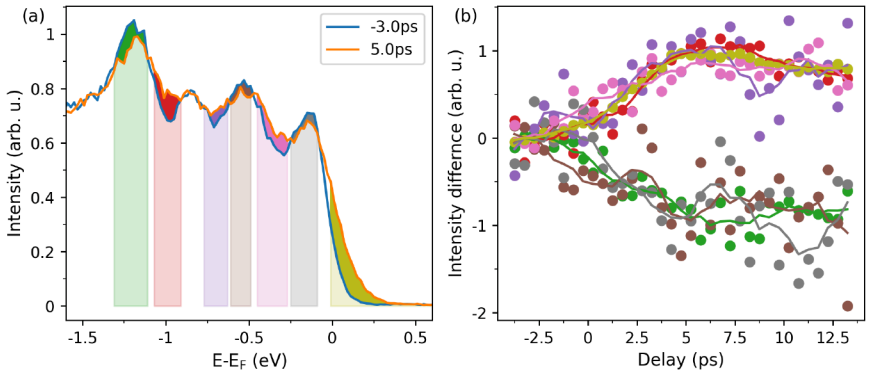

Figure 6.8: (a) Photoemission spectra of the semimetallic sample with a Te substitution of x=0.05 before t_0 (blue) and after (orange). The areas of intensity loss and gain are marked. (b) Intensity evolution of the peaks and inter-peak areas as marked in (a). The signal is normalized to absolute value of its intensity at $t = 5 \pm 1$ ps. The dynamics of all areas show a similar behavior. All the peaks are depleting, while the signal in the valleys in between the peaks increases in the first 5 ps and than flattens out.

In Figure 6.8, we take a closer look at the multiplet peaks of the semimetallic sample with a substitution of $x = 0.05$. Here the intensity evolution is presented for each peak and the valley between them. For comparison, the EDCs of the unpumped (blue line) and at 5 ps after excitation (orange line) are shown in Figure 6.8(a). In Figure 6.8(b), the temporal intensity evolution of the peaks and valleys is presented as a function of pump-probe delay. The intensity of each peak (valley) is given by integration over a peak (valley). The corresponding areas of integration are marked in Figure 6.8(a). The intensity evolution is represented by the intensity difference at each delay to the average unpumped ($t < t_0$) intensity. For better comparison, the difference is then also normalized to the total average absolute value. The rolling average of five data points is used as a guide to the eye. The intensity of all valleys increases as a function of the delay time, while the peak intensity decreases. The rise and fall take about 5 ps. Afterwards, the peak intensity levels out for at least 7 ps, while the off-peak intensity starts to drop on a longer time scale.

The dynamics of $TmSe_{1-x}Te_x$ near E_F are shown in Figure 6.9. Selected EDCs for different time delays are presented in the top row in Figures 6.9(a-c) for $x = 0.05$, $x = 0.29$, and $x = 0.46$, respectively. The EDC for $x = 0.05$ at 4 ps indicates the presence of a weak pedestal at the base of the $^3H_6$ peak, which disappears at 10 ps. In order to clearly analyze the amount of spectral weight transferring to other regions, the spectrum at each delay is normalized to the spectral weight of the $^3H_6$ peak (area D) before t_0. The bottom row depicts the evolution of the spectral weight of area D and area E for dif-

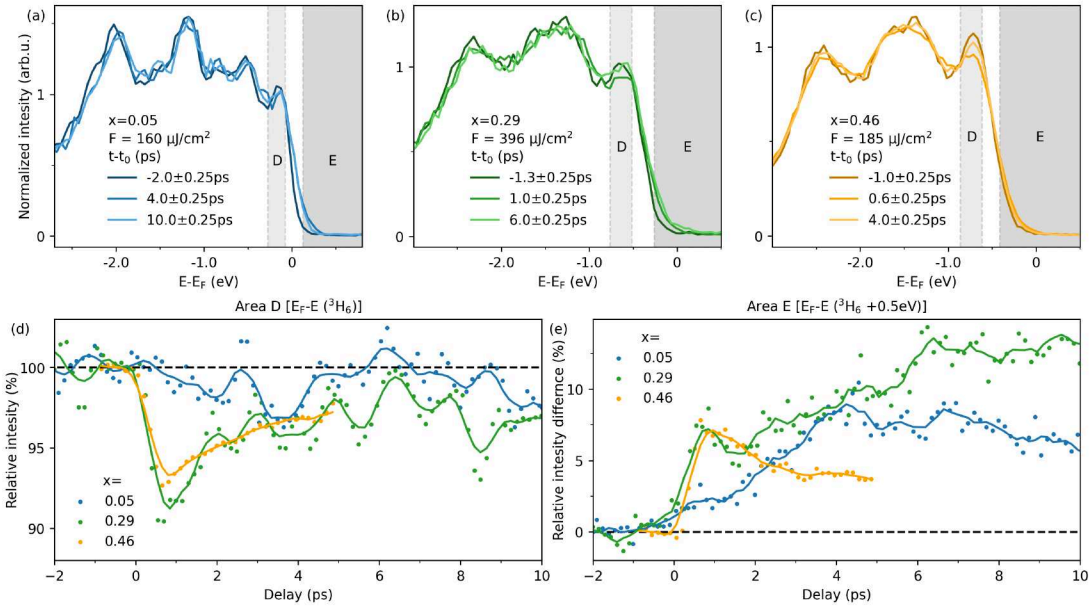

Figure 6.9: Dynamic of the $^3H_6$ peak for different substitutions. (a-c) $4f$ multiplet spectrum close to the Fermi level for three different Te substitutions. The spectra are normalized to their intensity before t_0. (d) Peak intensity evolution of the $^3H_6$ peak for the three samples. (e) The signal integrated in the area above the $^3H_6$ peak as a function of pump-probe delay.

ferent substitutions x. The intensity evolution of the $^3H_6$ peak is shown in Figure 6.9(d). The $^3H_6$ peak intensity for $x > 0.29$ shows a decrease of about -7% and -9% in the first 400 fs after t_0. Afterwards, the peak intensity recovers over several ps. For the semimetallic sample ($x = 0.05$), the peak intensity decrease is barely visible (only -3% and the background noise is much stronger), and no sudden increase is observed at t_0.

Figure 6.9(e) demonstrates the intensity evolution of the region E, 0.5 eV above the $^3H_6$ peak, by using the difference of each spectrum with respect to the normalized spectra before t_0. The intensity of the sample with $x = 0.46$ in the region E shows an inverted behavior to the intensity evolution of the $^3H_6$ peak shown in Figure 6.9(d). The intensity increases within 400 fs to 7% with respect to the $^3H_6$ peak intensity before t_0. Afterwards, the intensity slowly drops with a lifetime of about 5 ps. The semimetallic sample ($x = 0.05$) shows only a slow increase in intensity over 4.5 ps and 9% of the peak intensity. The sample with $x = 0.29$ again shows characteristics of both the semimetallic and insulating phases. Its intensity evolution also has a similar rapid increase at t_0 like the insulating sample, but the intensity continues to increase over the next 6 ps to 14% of the peak intensity.

To further investigate the slow dynamics, the delay range in the measurement of the semimetallic sample was extended up to 54 ps after t_0. The additional 40 ps are covered by fixed delay measurements with 5 ps steps in between. So, the measurement is split into two parts, the frist 3 hours of continuous delay scan followed by 1.5 hours of fixed delay measurements. Because the fixed-delay measurements are taken sequentially, not all delays are affected equally by the aging of the sample. Due to the conventional aging process of mixed-valence compounds [168], the total spectral weight may no longer be a good normalization for intensity fluctuations.

In order to understand the influence of sample aging on the dynamics of the $^3H_6$ peak, the first part of the measurements, which involves the continuous delay stage movement, is analyzed by measurement time. For this purpose, the detector events are binned by energy, pump-probe delay, and measurement time. Measurement time refers to the actual time of day when an event was recorded. A comparison of the dynamics in the energy window E for the first, second, and third hour of measurement is shown in Figure 6.10(a). The dynamics do not change their general behavior. In other words, the same tendency of slow intensity evolution can be seen, while the total intensity decreases from hour to hour. In good approximation, the drop in intensity over the measurement time is linear as presented in Figure 6.10(b), where the intensity difference is shown as a function of measurement time.

The states above the Fermi level are populated for more than 20 ps after the NIR pump excitation. Because the rise time of 4.5 ps is much longer than our time resolution of 200 fs of the pump pulse, the population obviously cannot be described by a direct optical transition followed by exponential decay. It indicates that the $4f$ probe spectra do not reflect instantaneous excitations at t_0. Namely, the 800 nm pump pulses must excite

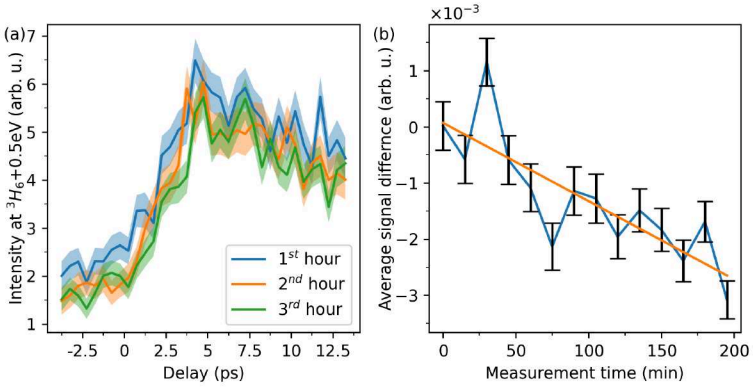

Figure 6.10: Long-term behavior of the dynamics above the Fermi level in the semimetallic sample. (a) The signal above the $^3H_6$ peak as a function of pump-probe delay similar to Figure 6.9(e). Each curve is related to another hour of measurement time. The statistical uncertainty is represented by the shaded area (b) Signal intensity over measurement time.

some states that cannot disturb the $4f$ photohole states. Thus, we can suspect that at least two different excitation levels exist in this ps dynamics: undetectable and detectable states within our probe $4f$ spectra. As the fit result in Figure 6.11 (orange dashed line) demonstrates, the dynamics can be well described by a sequential exponential decay process. We assume that the electrons are excited instantaneously to an unidentified higher state N_1. This state is not detectable under our measurement conditions, which probe mostly $4f$ character. Afterwards, from the N_1 level, the second state N_2 gets populated, which can be probed by photons with a photon energy of 110 eV. The state N_2 decays back to the ground state. The population N_2 can be described by

$$N_2(t) = \begin{cases} N_0 \frac{\tau_2}{\tau_1 - \tau_2} (e^{\frac{-(t-t_0)}{\tau_1}} - e^{\frac{-(t-t_0)}{\tau_2}}), & t > t_0 \\ 0, & t < t_0 \end{cases}, \tag{6.3}$$

where N_0 is the total number of excited electrons, τ_1 describes the decay rate from the highest excited state to the second state, and τ_2 the decay rate from the second state to the ground state. For $\tau_1 = \tau_2$ the function 6.3 has a removable singularity. In this case, the population N_2 is described by

$$N_2(t) = \begin{cases} N_0 \frac{t-t_0}{\tau_1} e^{\frac{-(t-t_0)}{\tau_1}}, & t > t_0 \\ 0, & t < t_0 \end{cases}. \tag{6.4}$$

Interestingly, the best fit is obtained when both decay channels have the same lifetime $\tau_1 = \tau_2 = 5.63$ ps, which corresponds to an energy of 0.12 meV. Such a small energy

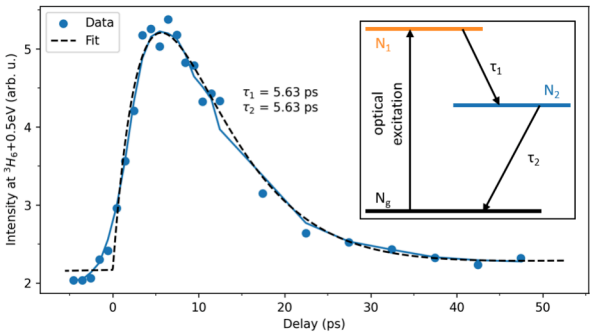

Figure 6.11: Overall temporal evolution of the PES intensity above the coherent peak next to the Fermi level. A direct optical excitation is not visible and the population is delayed by about 6 ps. The decay process afterwards continues for more than 20 ps. With the simple two-step exponential decay model, the time-evolution can be reproduced quite well (black-dashed line). The data could be fitted best, with both decay rates being identical, using $\tau_1 = \tau_2 = 5.63$ ps.

excitation is consistent with early results of inelastic neutron scattering measurements [169].

tr-ARPES data, measured with the new Ytterbium fiber laser for PG2 on the same $x = 0.05$ sample in the most resent beamtime, showed in the preliminary data evaluation no dynamics at all. The pump wavelengths were 1030 nm and 515 nm. This may suggest the presence of wavelength-dependent dynamics. According to literature, the transition from $^3H_6$ to $^3H_6$ in Tm^{3+} requires a pump wavelength of 800 nm (1.55 eV) [170]. This might indicate that the pump excites Tm resonantly.

Due to the FEL photon energy of $h\nu = 110$ eV, the $4f$ character is mainly probed. Thus, the pump-probe data can be interpreted as the temporal evolution of the excited $4f$ photohole states. Assuming that such ps dynamics in the semimetallic phase originate purely from the presence of the $4f5d$ hybridized band, one would expect similar dynamics in other heavy-fermion systems. However, such behavior has not yet been reported for other rare-earth systems [171–176]. Thus, it is likely that some potentially unique properties of these semimetallic Tm systems are responsible for the slow dynamics of the $^3H_6$ state.

6.7 Summary

The static ARPES data reveal for $TmSe_{1-x}Te_x$ a semimetallic mixed-valence phase for a Te substitution of $x = 0.11$ and below. For higher substitution $x > 0.29$, an insulating phase is established. In the semimetallic mixed-valence phase ($x = 0.05$), the sharp $^3H_6$

peak is located close to the Fermin level. The temperature dependence of the sharp $^3H_6$ peak reveals the coherent nature of the $4f5d$ hybridized state. In the insulating phase, the $^3H_6$ peak is shifted by 0.6 eV to higher binding energies and shows no evidence of coherence at low temperatures.

The pump-probe measurements on the insulating sample revealed a sudden response of the $^3H_6$ peak to the pump pulse. The $^3H_6$ peak lost intensity at t_0 in the same way as the area 0.5 eV above the peak gained intensity. The electronic structure then relaxes back to the ground state within a few ps. In contrast, the tr-PES data on the semimetallic sample show a slower dynamic of $^3H_6$ on a few *ps* time scale, which includes a slow rise and a long decay. This unique temporal evolution appeared only for a substitution of $x = 0.05$, but its origin still remains unclear.

7 Summary and outlook

We investigated the ultrafast dynamics of three different quantum materials, graphene, the topological insulator Bismuth selenide and the heavy-fermionic mixed-valence system Thulium selenide, with tr-PES. Therefore, we employed two ToF based PES spectrometer setups paired with different EUV and X-ray light sources in a pump-probe scheme.

Graphene, which has been extensively researched, was utilized as a reference to benchmark the state-of-the-art ToF momentum microscope HEXTOF. In the frequent usage for tr-ARPES measurements with soft X-ray photons at FLASH, the HEXTOF setup proves to be highly versatile and efficient [22, 140, 177–180]. Furthermore, the setup can be seamlessly integrated with a laboratory-based HHG source [108]. The spectrometer allows for simultaneous recording of 2D momentum information and the kinetic energy of electrons. We were able to demonstrate a wide field of view of $\pm 2.4\,\text{Å}^{-1}$ in momentum space, which is sufficient for easily mapping more than the first Brillouin zone of most crystalline structures. However, the acceptable field of view was limited by the angle of acceptance of the used electron optics settings. The energy resolution of the HEXTOF setup is approximately 100 meV and, depending on the photon source, the time resolution falls within the range of 90 fs to 150 fs. By selecting different harmonics, the HHG source allows for ARPES measurements at different k_z values. This is a unique capability for laboratory-based experiments and is otherwise only available at large-scale facilities. Our research showcased successful 3D Fermi surface tomography of Graphene on Iridium.

The study on Bi_2Se_3 utilized the HEXTOF setup to examine the electron dynamics at high pump fluence. The results revealed dynamics on a time scale of a few ps in the bulk conduction band and the Dirac cone of the topological surface state that connect the bulk conduction band with the bulk valence band. Comparatively, the electron dynamics of the surface state and bulk conduction band keep their original characteristics when measured at low fluence levels. Additionally, we demonstrated that an absorbed fluence of $11.9\,\frac{\text{mJ}}{\text{cm}^2}$ or higher causes damage to the surface of Bi_2Se_3, resulting in material removal. This observation led to the conclusion that the laser does not melt Bi_2Se_3 nor rearrange the crystal structure.

$TmSe_{1-x}Te_x$ is a heavy-fermion system that shows a semimetallic mixed-valence phase when the Te substitution x is at a value of 0.11 or below. In the semimetallic mixed-valence phase with a substitution of $x = 0.05$, the sharp $^3H_6$ peak is located in close proximity to the Fermi level. The coherent nature of the $4f5d$ hybridized state is

highlighted by the temperature dependence of the sharp $^3H_6$ Tm $4f$ peak. The tr-PES results of the semimetallic sample demonstrate a slow time evolution of the $^3H_6$ state, which is characterized by a slow increase in intensity and a long decay over a time scale of several ps. For higher substitution levels $x > 0.29$, an insulating phase is established in which the $^3H_6$ peak is shifted by 0.6 eV to higher binding energies and shows no evidence of coherence at low temperatures. In contrast, the pump-probe measurements on the insulating sample depicted a sudden response of the $^3H_6$ peak to the pump pulse. The $^3H_6$ peak lost intensity at t_0 in the same way as the area 0.5 eV above the peak gained intensity. The electronic structure then relaxes to the ground state within a several ps.

Due to the moderate repetition rate of current photon sources for time-resolved experiments, the high detection efficiency of the ToF photoelectron spectrometer is essential for most tr-ARPES experiments. Improved photon sources will enhance the rate of repetition, tunability, and intensity stability. Regardless of the relaxation time of the sample, pump-probe measurements are limited to a repetition rate of a few MHz, which necessitates an efficient detection scheme. In the coming months and years, novel and improved ultrafast EUV and X-ray sources are expected to become operational.

These sources are expected to have a superior repetition rate and extend the measurement range to higher photon energies. The LCLS II upgrade and the new high-repetition HHG source for HEXTOF, with a planned repetition rate of 1 MHz, will provide sufficient pulses to perform time- and spin-resolved ARPES measurements. This would, for instance, allow the direct measurement of magnetic phase evolution and the mapping of surface state spin dynamics in topological insulators. The higher photon energies, which are available for the new momentum microscopes at the SASE3 beamline of the European XFEL and at LCLS II, will allow us to look at more strongly bound core levels. Due to the possibility of higher kinetic energies of the photoelectrons, forward scattering processes are dominant in XPD measurements. This simplifies measurement interpretation. The upcoming upgrades for FLASH will be tailored towards improving the time resolution of PES experiments. The forthcoming FL23 Beamline at FLASH II offers a time-compensated monochromator to mitigate pulse elongation caused by dispersion of the EUV beam. The seeding project for FLASH I aims to achieve ultrashort pulses at the diffraction limit with no SASE fluctuation. This will improve the time resolution of PES in the soft X-ray regime and stabilize the measurement conditions, which makes for example space charge more controllable.

Acknowledgement

Finally, I would like to thank everyone who supported me during my doctorate.

I would especially like to thank Prof. Kai Rossnagel. Thank you for taking over the supervision of the doctorate and thus giving me the opportunity to continue my doctorate. The scientific discussions about the data, future measurement periods and the other projects at the HEXTOF meeting were very helpful.

Thanks also to Prof. Franz Kärtner for taking the time to review this thesis as a second reviewer.

Thanks to Dima and Nils for their cooperation with all the tasks in the lab and the beam times. Thank you for sharing all the work in the lab so well as a team and not following the motto: "Ihr macht eure Experimente, ich mache meine."[The guy from the Restaurant Samarkand, 2018].

Thank you, Chul-Hee, for introducing me to mixed-valence systems in general and thulium selenides in particular. Thank you for taking the time to discuss the data and its analysis in detail.

Many thanks to Markus and my father for "dismantling" this work. Thank you for the helpful corrections.

Thanks to Hannah and Marlis for their administrative support. Thank you for the daily fight against the administrative bureaucracy.

Without the FLASH team, especially Lukas, Federico, Siarhei and Günter, all the beam times would not have been possible. Thank you for your time and your work.

I would also like to thank the former AG Wurth for their support and the good atmosphere in the group. Without Sven and Holger and their technical support, some projects, such as the new frame for the Refocus chamber in the HHG lab, would not have been possible. Thank you very much.

I would also like to thank everyone who was not directly involved in the work. Thanks to Timo, Gabriel, Lea and Lauritz, who have been my flatmates over the years and we got on well, especially during the coronavirus period. As an example, I would like to mention Timo's "support" in the first Corona lookdown, which could start with the words "Bier?" at almost any time of the day.

Thanks also to my student friends David, Ryan, Calvin and Kai. Thanks for the time to think differently and distract me from work, for example with stories by, with or about David.

After the mental balance, I now come to the physical. I would like to thank Svenja, Alexander, Thomas, Marc and Jens. I spent a large part of the estimated 6000 kilometers

rowing together with you in the boat. I should probably also take this opportunity to thank Christine for torturing me with the Core stabilization exercises.

I would also like to thank my parents for their support during the whole time.

I don't want to forget Wilfried, who started this project. It was with him in the group that I also laid the foundation for this work with my Bachelor's and Master's theses.

List of Abbreviations

2D	two-dimensional
3D	three-dimensional
ARPES	angle-resolved photoemission spectroscopy
DAQ	data acquisition server
DLD	delay line detector
EDC	energy distribution curve
EUV	extreme ultraviolet
FEL	free-electron laser
FWHM	full width at half maximum
HHG	higher harmonic generation
IPES	inverse photoemission spectroscopy
LAPE	laser-assisted photoemission
LEED	low energy electron diffraction
MCP	microchannel plate
MDC	momentum distribution curve
NIR	near infrared
PEEM	photoemission electron microscopy
PES	photoemission spectroscopy
SASE	self-amplified spontaneous emission
ToF	time-of-flight
tr-	time-resolved
XPD	X-ray photoelectron diffraction

List of Publications

Parts of the findings in the chapter 4 "Graphene on iridium as a performance benchmark" are published in:

“Multispectral time-resolved energy-momentum microscopy using high-harmonic extreme ultraviolet radiation”, M. Heber, N. Wind, D. Kutnyakhov, F. Pressacco, T. Arion, F. Roth, W. Eberhardt, and K. Rossnagel, *Review of Scientific Instruments*, vol. **93**, p. 083905, 08 2022.

For this publication, I was involved in all measurements and analyzed the data of the graphene on Ir(111) as well as the HHG spectrum. I significantly contributed to writing and illustrating the results, particularly in the sections “Multispectral photon source”, “Experimental resolutions”, and “Multispectral energy–momentum mapping”.

Parts of findings in the chapter 5 "The robustness of the topological surface state of bismuth selenide" are considered to be published:

“Robustness of topologically protected surface state of Bi_2Se_3”, M. Heber, K. Bühlmann, N. Wind, D. Kutnyakhov, D. Curcio, K. Volckaert, M. Bianchi, F. Pressacco, L. Wenthaus, G. Brenner, P. Hofmann, Y. Acremann, and K. Rossnagel; In preparation, Draft
The draft was written by me. I was involved in all measurements and analyzed the data.

Parts of findings in the chapter 6 "Ultrafast electron dynamics of the mixed-valence system thulium selenide" are considered to be published in two parts. The static measurements are summarized in the draft:

“Emergence of the $4f$ fine structure in $TmSe_{1-x}Te_x$ across the insulator-to-semimetal phase transition”, C.-H. Min, S. Müller, W. J. Choi, V. Zabolotnyy, M. Heber, L. Dudy, J. D. Denlinger, C.-J. Kang, M. Kalläne, N. Wind, M. Scholz, T. L. Lee, C. Schlueter, A. Gloskovskii, E. D. L. Rienks, V. Hinkov, H. Bentmann, Y. S. Kwon, F. Reinert, and K. Rossnagel; In preparation

The static PES data were measured by Chul-Hee Min. My involvement was here limited to the analysis of the P22@PETRA III data.

The time-resolved data are summarized in the second part: “Neutrally charged many-body states in the unique mixed-valence $TmSe_{1-x}Te_x$”, C.-H. Min, M. Heber, S. Müller, L. Wenthaus, S. Palutke, D. Kutnyakhov, F. Pressacco, L. Dudy, M. Scholz, W. J. Choi, Y.-S. Kwon, J. D. Denlinger, T. K. Kim, C. Cacho, M. Kalläne, H. Bentmann, J. D. Denlinger, C.-J. Kang, F. Reinert, and K. Rossnagel; In preparation

Here I was involved in all measurements at FLASH and analyzed the time-resolved data.

Publications which are not directly related to this work:

- “Observation of an excitonic mott transition through ultrafast core-cum-conduction photoemission spectroscopy”, M. Dendzik, R. P. Xian, E. Perfetto, D. Sangalli, D. Kutnyakhov, S. Dong, S. Beaulieu, T. Pincelli, F. Pressacco, D. Curcio, S. Y. Agustsson, M. Heber, J. Hauer, W. Wurth, G. Brenner, Y. Acremann, P. Hofmann, M. Wolf, A. Marini, G. Stefanucci, L. Rettig, and R. Ernstorfer; *Phys. Rev. Lett.*, vol. **125**, p. 096401, 8 2020.

- “Time- and momentum-resolved photoemission studies using time-of-flight momentum microscopy at a free-electron laser”, D. Kutnyakhov, R. P. Xian, M. Dendzik, M. Heber, F. Pressacco, S. Y. Agustsson, L. Wenthaus, H. Meyer, S. Gieschen, G. Mercurio, A. Benz, K. Bühlman, S. Daster, R. Gort, D. Curcio, K. Volckaert, M. Bianchi, C. Sanders, J. A. Miwa, S. Ulstrup, A. Oelsner, C. Tusche, Y.-J. Chen, D. Vasilyev, K. Medjanik, G. Brenner, S. Dziarzhytski, H. Redlin, B. Manschwetus, S. Dong, J. Hauer, L. Rettig, F. Diekmann, K. Rossnagel, J. Demsar, H.-J. Elmers, P. Hofmann, R. Ernstorfer, G. Schönhense, Y. Acremann, and W. Wurth; *Review of Scientific Instruments*, vol. **91**, no. 1, p. 013109, 2020.

- “An open-source, end-to-end workflow for multidimensional photoemission spectroscopy”, R. P. Xian, Y. Acremann, S. Y. Agustsson, M. Dendzik, K. Bühlmann, D. Curcio, D. Kutnyakhov, F. Pressacco, M. Heber, S. Dong, T. Pincelli, J. Demsar, W. Wurth, P. Hofmann, M. Wolf, M. Scheidgen, L. Rettig, and R. Ernstorfer; *Scientific Data*, vol. **7**, p. 442, 12 2020.

- “Suppression of the vacuum space-charge effect in fs-photoemission by a retarding electrostatic front lens”, G. Schönhense, D. Kutnyakhov, F. Pressacco, M. Heber, N. Wind, S. Y. Agustsson, S. Babenkov, D. Vasilyev, O. Fedchenko, S. Chernov, L. Rettig, B. Schönhense, L. Wenthaus, G. Brenner, S. Dziarzhytski, S. Palutke, S. K. Mahatha, N. Schirmel, H. Redlin, B. Manschwetus, I. Hartl, Y.

Matveyev, A. Gloskovskii, C. Schlueter, V. Shokeen, H. Duerr, T. K. Allison, M. Beye, K. Rossnagel, H. J. Elmers, and K. Medjanik; *Review of Scientific Instruments*, vol. **92**, no. 5, p. 053703, 2021.

- "Tracking the surface atomic motion in a coherent phonon oscillation", D. Curcio, K. Volckaert, D. Kutnyakhov, S. Y. Agustsson, K. Bühlmann, F. Pressacco, M. Heber, S. Dziarzhytski, Y. Acremann, J. Demsar, W. Wurth, C. E. Sanders, and P. Hofmann; *Phys. Rev. B*, vol. 106, p. L201409, 11 2022.

- "Ultrafast orbital tomography of a pentacene film using time-resolved momentum microscopy at a FEL", K. Baumgärtner, M. Reuner, C. Metzger, D. Kutnyakhov, M. Heber, F. Pressacco, C.-H. Min, T. R. F. Peixoto, M. Reiser, C. Kim, W. Lu, R. Shayduk, M. Izquierdo, G. Brenner, F. Roth, A. Schöll, S. Molodtsov, W. Wurth, F. Reinert, A. Madsen, D. Popova-Gorelova, and M. Scholz; *Nature Communications*, vol. **13**, p. 2741, 5 2022.

- "Ultrafast mhz-rate burst-mode pump–probe laser for the flash fel facility based on nonlinear compression of ps-level pulses from an yb-amplifier chain", M. Seidel, F. Pressacco, O. Akcaalan, T. Binhammer, J. Darvill, N. Ekanayake, M. Frede, U. Grosse-Wortmann, M. Heber, C. M. Heyl, D. Kutnyakhov, C. Li, C. Mohr, J. Müller, O. Puncken, H. Redlin, N. Schirmel, S. Schulz, A. Swiderski, H. Tavakol, H. Tünnermann, C. Vidoli, L. Wenthaus, N. Wind, L. Winkelmann, B. Manschwetus, and I. Hartl; *Laser & Photonics Reviews*, vol. **16**, no. 3, p. 2100268, 2022.

- "Real-time observation of non-equilibrium phonon-electron energy flow in laser-heated nickel", V. Shokeen, M. Heber, D. Kutnyakhov, X. Wang, A. Yaroslavtsev, P. Maldonado, M. Berritta, N. Wind, L. Wenthaus, F. Pressacco, C.-H. Min, M. Nissen, S. K. Mahatha, S. Dziarzhytski, P. M. Oppeneer, K. Rossnagel, H. J. Elmers, G. Schönhense, and H. Dürr; *Science Advances*, vol. **10**, no. 5, 2024

- "Out-of-equilibrium charge redistribution in a copper-oxide based superconductor by time-resolved X-ray photoelectron spectroscopy", D. Puntel, D. Kutnyakhov, L. Wenthaus, M. Scholz, N. Wind, M. Heber, G. Brenner, G. Gu, R. J. Cava, W. Bronsch, F. Cilento, F. Parmigiani, and F. Pressacco; In preparation

- "Multiplex movie of concerted rotation of molecules on a 2D material", K. Baumgärtner, M. Nozaki, M. Reuner, N. Wind, M. Haniuda, C. Metzger, M. Heber, D. Kutnyakhov, F. Pressacco, L. Wenthaus, K. Hara, C.-H. Min, M. Beye, F. Reinert, F. Roth, S. K. Mahatha, A. Madsen, T. Wehling, K. Niki, D. Popova-Gorelova, K. Rossnagel, and M. Scholz; In preparation

Bibliography

1. Keimer, B. & Moore, J. E. The physics of quantum materials. *Nature Physics* **13,** 1045–1055. ISSN: 1745-2481. https://doi.org/10.1038/nphys4302 (Nov. 2017).
2. Damascelli, A. Probing the Electronic Structure of Complex Systems by ARPES. *Physica Scripta* **T109,** 61. https://doi.org/10.1238/physica.topical.109a00061 (2004).
3. Lv, B., Qian, T. & Ding, H. Angle-resolved photoemission spectroscopy and its application to topological materials. *Nature Reviews Physics* **1,** 609–626. https://doi.org/10.1038/s42254-019-0088-5 (2019).
4. King, P. D. C., Picozzi, S., Egdell, R. G. & Panaccione, G. Angle, Spin, and Depth Resolved Photoelectron Spectroscopy on Quantum Materials. *Chemical Reviews* **121.** PMID: 33346644, 2816–2856. eprint: https://doi.org/10.1021/acs.chemrev.0c00616. https://doi.org/10.1021/acs.chemrev.0c00616 (2021).
5. Sobota, J. A., He, Y. & Shen, Z.-X. Angle-resolved photoemission studies of quantum materials. *Rev. Mod. Phys.* **93,** 025006. https://link.aps.org/doi/10.1103/RevModPhys.93.025006 (2 May 2021).
6. Chiang, T.-C., Knapp, J. A., Aono, M. & Eastman, D. E. Angle-resolved photoemission, valence-band dispersions $E(\vec{k})$, and electron and hole lifetimes for GaAs. *Phys. Rev. B* **21,** 3513–3522. https://link.aps.org/doi/10.1103/PhysRevB.21.3513 (8 Apr. 1980).
7. Medjanik, K. *et al.* Direct 3D mapping of the Fermi surface and Fermi velocity. *Nature Materials* **16,** 615–621. ISSN: 1476-4660. https://doi.org/10.1038/nmat4875 (2017).
8. Hüfner, S. *et al.* Photoemission spectroscopy in metals:: band structure-Fermi surface–spectral function. *Journal of Electron Spectroscopy and Related Phenomena* **100,** 191–213. ISSN: 0368-2048. https://www.sciencedirect.com/science/article/pii/S036820489900047X (1999).

9. Valla, T., Fedorov, A. V., Johnson, P. D. & Hulbert, S. L. Many-Body Effects in Angle-Resolved Photoemission: Quasiparticle Energy and Lifetime of a Mo(110) Surface State. *Phys. Rev. Lett.* **83,** 2085–2088. https://link.aps.org/doi/10.1103/PhysRevLett.83.2085 (10 Sept. 1999).

10. Krasovskii, E. E., Rossnagel, K., Fedorov, A., Schattke, W. & Kipp, L. Determination of the Hole Lifetime from Photoemission: Ti 3*d* States in $TiTe_2$. *Phys. Rev. Lett.* **98,** 217604. https://link.aps.org/doi/10.1103/PhysRevLett.98.217604 (21 May 2007).

11. Watson, M. D. *et al.* Orbital- and k_z-Selective Hybridization of Se 4*p* and Ti 3*d* States in the Charge Density Wave Phase of $TiSe_2$. *Phys. Rev. Lett.* **122,** 076404. https://link.aps.org/doi/10.1103/PhysRevLett.122.076404 (7 Feb. 2019).

12. Puschnig, P. *et al.* Reconstruction of Molecular Orbital Densities from Photoemission Data. *Science* **326,** 702–706. eprint: https://www.science.org/doi/pdf/10.1126/science.1176105. https://www.science.org/doi/abs/10.1126/science.1176105 (2009).

13. Graus, M. *et al.* Three-dimensional tomographic imaging of molecular orbitals by photoelectron momentum microscopy. *The European Physical Journal B* **92,** 80. https://doi.org/10.1140/epjb/e2019-100015-x (2019).

14. Wannberg, B. Electron optics development for photo-electron spectrometers. *Nuclear Instruments and Methods in Physics Research Section A: Accelerators, Spectrometers, Detectors and Associated Equipment* **601.** Special issue in honour of Prof. Kai Siegbahn, 182–194. ISSN: 0168-9002. https://www.sciencedirect.com/science/article/pii/S0168900208020238 (2009).

15. Kotsugi, M., Kuch, W., Offi, F., Chelaru, L. I. & Kirschner, J. Microspectroscopic two-dimensional Fermi surface mapping using a photoelectron emission microscope. *Review of Scientific Instruments* **74,** 2754–2758. eprint: https://doi.org/10.1063/1.1569404. https://doi.org/10.1063/1.1569404 (2003).

16. Schönhense, G., Medjanik, K. & Elmers, H.-J. Space-, time- and spin-resolved photoemission. *Journal of Electron Spectroscopy and Related Phenomena* **200.** Special Anniversary Issue: Volume 200, 94–118. ISSN: 0368-2048 (2015).

17. Babenkov, S. *et al.* High-accuracy bulk electronic bandmapping with eliminated diffraction effects using hard X-ray photoelectron momentum microscopy. *Communications Physics* **2,** 107. ISSN: 2399-3650. https://doi.org/10.1038/s42005-019-0208-7 (Sept. 2019).

18. Rossnagel, K. *et al.* Three-dimensional Fermi surface determination by angle-resolved photoelectron spectroscopy. *Phys. Rev. B* **63,** 125104. https://link.aps.org/doi/10.1103/PhysRevB.63.125104 (12 Mar. 2001).

19. Nielsen, M. B., Li, Z., Lizzit, S., Goldoni, A. & Hofmann, P. Bulk Fermi surface mapping with high-energy angle-resolved photoemission. *Journal of Physics: Condensed Matter* **15,** 6919–6930. https://doi.org/10.1088/0953-8984/15/41/002 (Oct. 2003).

20. Strocov, V. N. *et al.* Soft-X-ray ARPES at the Swiss Light Source: From 3D Materials to Buried Interfaces and Impurities. *Synchrotron Radiation News* **27,** 31–40. eprint: https://doi.org/10.1080/08940886.2014.889550. https://doi.org/10.1080/08940886.2014.889550 (2014).

21. Moser, S. An experimentalist's guide to the matrix element in angle resolved photoemission. *Journal of Electron Spectroscopy and Related Phenomena* **214,** 29–52. ISSN: 0368-2048. https://www.sciencedirect.com/science/article/pii/S0368204816301724 (2017).

22. Kutnyakhov, D. *et al.* Time- and momentum-resolved photoemission studies using time-of-flight momentum microscopy at a free-electron laser. *Review of Scientific Instruments* **91,** 013109. eprint: https://doi.org/10.1063/1.5118777. https://doi.org/10.1063/1.5118777 (2020).

23. Maklar, J. *et al.* A quantitative comparison of time-of-flight momentum microscopes and hemispherical analyzers for time- and angle-resolved photoemission spectroscopy experiments. *Review of Scientific Instruments* **91,** 123112. eprint: https://doi.org/10.1063/5.0024493. https://doi.org/10.1063/5.0024493 (2020).

24. Keunecke, M. *et al.* Time-resolved momentum microscopy with a 1 MHz high-harmonic extreme ultraviolet beamline. *Review of Scientific Instruments* **91,** 063905. eprint: https://doi.org/10.1063/5.0006531. https://doi.org/10.1063/5.0006531 (2020).

25. Perfetti, L. *et al.* Time Evolution of the Electronic Structure of $1T-TaS_2$ through the Insulator-Metal Transition. *Phys. Rev. Lett.* **97,** 067402. https://link.aps.org/doi/10.1103/PhysRevLett.97.067402 (6 Aug. 2006).

26. Schmitt, F. *et al.* Transient Electronic Structure and Melting of a Charge Density Wave in $TbTe_3$. *Science* **321,** 1649–1652. eprint: https://www.science.org/doi/pdf/10.1126/science.1160778. https://www.science.org/doi/abs/10.1126/science.1160778 (2008).

27. Rohwer, T. *et al.* Collapse of long-range charge order tracked by time-resolved photoemission at high momenta. *Nature* **471,** 490–493. https://doi.org/10.1038/nature09829 (2011).

28. Smallwood, C. L. *et al.* Tracking Cooper Pairs in a Cuprate Superconductor by Ultrafast Angle-Resolved Photoemission. *Science* **336,** 1137–1139. eprint: https://www.science.org/doi/pdf/10.1126/science.1217423. https://www.science.org/doi/abs/10.1126/science.1217423 (2012).

29. Gierz, I. *et al.* Snapshots of non-equilibrium Dirac carrier distributions in graphene. *Nature Materials* **12,** 1119–1124. https://doi.org/10.1038/nmat3757 (2013).

30. Wang, Y. H., Steinberg, H., Jarillo-Herrero, P. & Gedik, N. Observation of Floquet-Bloch States on the Surface of a Topological Insulator. *Science* **342,** 453–457. eprint: https://www.science.org/doi/pdf/10.1126/science.1239834. https://www.science.org/doi/abs/10.1126/science.1239834 (2013).

31. Mahmood, F. *et al.* Selective scattering between Floquet–Bloch and Volkov states in a topological insulator. *Nature Physics* **12,** 306–310. https://doi.org/10.1038/nphys3609 (2016).

32. Nicholson, C. W. *et al.* Beyond the molecular movie: Dynamics of bands and bonds during a photoinduced phase transition. *Science* **362,** 821–825. eprint: https://www.science.org/doi/pdf/10.1126/science.aar4183. https://www.science.org/doi/abs/10.1126/science.aar4183 (2018).

33. Na, M. X. *et al.* Direct determination of mode-projected electron-phonon coupling in the time domain. *Science* **366,** 1231–1236. eprint: https://www.science.org/doi/pdf/10.1126/science.aaw1662. https://www.science.org/doi/abs/10.1126/science.aaw1662 (2019).

34. Wallauer, R. *et al.* Tracing orbital images on ultrafast time scales. *Science.* ISSN: 0036-8075. https://science.sciencemag.org/content/early/2021/02/17/science.abf3286 (2021).

35. Gauthier, A. *et al.* Tuning time and energy resolution in time-resolved photoemission spectroscopy with nonlinear crystals. *Journal of Applied Physics* **128,** 093101. eprint: https://doi.org/10.1063/5.0018834. https://doi.org/10.1063/5.0018834 (2020).

36. Bao, C. *et al.* Ultrafast time- and angle-resolved photoemission spectroscopy with widely tunable probe photon energy of 5.3–7.0 eV for investigating dynamics of three-dimensional materials. *Review of Scientific Instruments* **93,** 013902. eprint: https://doi.org/10.1063/5.0070004. https://doi.org/10.1063/5.0070004 (2022).

37. Dakovski, G. L., Li, Y., Durakiewicz, T. & Rodriguez, G. Tunable ultrafast extreme ultraviolet source for time- and angle-resolved photoemission spectroscopy. *Review of Scientific Instruments* **81,** 073108. eprint: https://doi.org/10.1063/1.3460267. https://doi.org/10.1063/1.3460267 (2010).

38. Frietsch, B. *et al.* A high-order harmonic generation apparatus for time- and angle-resolved photoelectron spectroscopy. *Review of Scientific Instruments* **84,** 075106. eprint: https://doi.org/10.1063/1.4812992. https://doi.org/10.1063/1.4812992 (2013).

39. Eich, S. *et al.* Time- and angle-resolved photoemission spectroscopy with optimized high-harmonic pulses using frequency-doubled Ti:Sapphire lasers. *Journal of Electron Spectroscopy and Related Phenomena* **195,** 231–236. ISSN: 0368-2048. https://www.sciencedirect.com/science/article/pii/S036820481400108X (2014).

40. Cilento, F. *et al.* Advancing non-equilibrium ARPES experiments by a 9.3eV coherent ultrafast photon source. *Journal of Electron Spectroscopy and Related Phenomena* **207,** 7–13. ISSN: 0368-2048. https://www.sciencedirect.com/science/article/pii/S0368204815002881 (2016).

41. Rohde, G. *et al.* Time-resolved ARPES with sub-15 fs temporal and near Fourier-limited spectral resolution. *Review of Scientific Instruments* **87,** 103102. eprint: https://doi.org/10.1063/1.4963668. https://doi.org/10.1063/1.4963668 (2016).

42. Corder, C. *et al.* Ultrafast extreme ultraviolet photoemission without space charge. *Structural Dynamics* **5,** 054301. eprint: https://doi.org/10.1063/1.5045578. https://doi.org/10.1063/1.5045578 (2018).

43. Puppin, M. *et al.* Time- and angle-resolved photoemission spectroscopy of solids in the extreme ultraviolet at 500 kHz repetition rate. *Review of Scientific Instruments* **90,** 023104. eprint: https://doi.org/10.1063/1.5081938. https://doi.org/10.1063/1.5081938 (2019).

44. Buss, J. H. *et al.* A setup for extreme-ultraviolet ultrafast angle-resolved photoelectron spectroscopy at 50-kHz repetition rate. *Review of Scientific Instruments* **90,** 023105. eprint: https://doi.org/10.1063/1.5079677. https://doi.org/10.1063/1.5079677 (2019).

45. Sie, E. J., Rohwer, T., Lee, C. & Gedik, N. Time-resolved XUV ARPES with tunable 24-33 eV laser pulses at 30 meV resolution. *Nature Communications* **10,** 3535–. ISSN: 2041-1723. https://doi.org/10.1038/s41467-019-11492-3 (2019).

46. Mills, A. K. *et al.* Cavity-enhanced high harmonic generation for extreme ultraviolet time- and angle-resolved photoemission spectroscopy. *Review of Scientific Instruments* **90,** 083001. eprint: https://doi.org/10.1063/1.5090507. https://doi.org/10.1063/1.5090507 (2019).

47. Liu, Y. *et al.* Extreme ultraviolet time- and angle-resolved photoemission setup with 21.5 meV resolution using high-order harmonic generation from a turn-key Yb:KGW amplifier. *Review of Scientific Instruments* **91,** 013102. eprint: https://doi.org/10.1063/1.5121425. https://doi.org/10.1063/1.5121425 (2020).

48. Cucini, R. *et al.* Coherent narrowband light source for ultrafast photoelectron spectroscopy in the 17–31 eV photon energy range. *Structural Dynamics* **7,** 014303. eprint: https://doi.org/10.1063/1.5131216. https://doi.org/10.1063/1.5131216 (2020).

49. Lee, C. *et al.* High resolution time- and angle-resolved photoemission spectroscopy with 11 eV laser pulses. *Review of Scientific Instruments* **91,** 043102. eprint: https://doi.org/10.1063/1.5139556. https://doi.org/10.1063/1.5139556 (2020).

50. Peli, S. *et al.* Time-resolved VUV ARPES at 10.8 eV photon energy and MHz repetition rate. *Journal of Electron Spectroscopy and Related Phenomena* **243,** 146978. ISSN: 0368-2048. https://www.sciencedirect.com/science/article/pii/S0368204820300463 (2020).

51. Guo, Q. *et al.* A narrow bandwidth extreme ultra-violet light source for time- and angle-resolved photoemission spectroscopy. *Structural Dynamics* **9,** 024304. ISSN: 2329-7778. eprint: https://pubs.aip.org/aca/sdy/article-pdf/doi/10.1063/4.0000149/16569000/024304_1_online.pdf. https://doi.org/10.1063/4.0000149 (Apr. 2022).

52. Gilbert, M. J. Topological electronics. *Communications Physics* **4,** 70. ISSN: 2399-3650. https://doi.org/10.1038/s42005-021-00569-5 (Apr. 2021).

53. Wang, K. L., Lang, M. & Kou, X. in *Handbook of Spintronics* (eds Xu, Y., Awschalom, D. D. & Nitta, J.) 431–462 (Springer Netherlands, Dordrecht, 2016). ISBN: 978-94-007-6892-5. https://doi.org/10.1007/978-94-007-6892-5_56.

54. Sobota, J. A. *et al.* Ultrafast Optical Excitation of a Persistent Surface-State Population in the Topological Insulator Bi_2Se_3. *Phys. Rev. Lett.* **108,** 117403. https://link.aps.org/doi/10.1103/PhysRevLett.108.117403 (11 Mar. 2012).

55. Baskaran, G. Majorana Fermi Sea in Insulating SmB_6: A proposal and a Theory of Quantum Oscillations in Kondo Insulators. *arXiv:1507.03477 [cond-mat].* arXiv: 1507.03477. http://arxiv.org/abs/1507.03477 (2021) (July 2015).

56. Knolle, J. & Cooper, N. R. Excitons in topological Kondo insulators: Theory of thermodynamic and transport anomalies in SmB_6. *Phys. Rev. Lett.* **118,** 096604. https://link.aps.org/doi/10.1103/PhysRevLett.118.096604 (9 Mar. 2017).

57. Erten, O., Chang, P.-Y., Coleman, P. & Tsvelik, A. M. Skyrme Insulators: Insulators at the Brink of Superconductivity. *Phys. Rev. Lett.* **119,** 057603. https://link.aps.org/doi/10.1103/PhysRevLett.119.057603 (5 Aug. 2017).

58. Chowdhury, D., Sodemann, I. & Senthil, T. Mixed-valence insulators with neutral Fermi surfaces. *Nature Communications* **9,** 1766. ISSN: 2041-1723. https://doi.org/10.1038/s41467-018-04163-2 (May 2018).

59. Varma, C. M. Majoranas in mixed-valence insulators. *Phys. Rev. B* **102,** 155145. https://link.aps.org/doi/10.1103/PhysRevB.102.155145 (15 Oct. 2020).

60. Hertz, H. Ueber einen Einfluss des ultravioletten Lichtes auf die electrische Entladung. *Annalen der Physik* **267,** 983–1000. eprint: https://onlinelibrary.wiley.com/doi/pdf/10.1002/andp.18872670827. https://onlinelibrary.wiley.com/doi/abs/10.1002/andp.18872670827 (1887).

61. Einstein, A. Über einen die Erzeugung und Verwandlung des Lichtes betreffenden heuristischen Gesichtspunkt. *Annalen der Physik* **322,** 132–148. eprint: https://onlinelibrary.wiley.com/doi/pdf/10.1002/andp.19053220607. https://onlinelibrary.wiley.com/doi/abs/10.1002/andp.19053220607 (1905).

62. Seah, M. P. & Dench, W. A. Quantitative electron spectroscopy of surfaces: A standard data base for electron inelastic mean free paths in solids. *Surface and Interface Analysis* **1,** 2–11. eprint: https://analyticalsciencejournals.onlinelibrary.wiley.com/doi/pdf/10.1002/sia.740010103. https://analyticalsciencejournals.onlinelibrary.wiley.com/doi/abs/10.1002/sia.740010103 (1979).

63. Tanuma, S., Powell, C. J. & Penn, D. R. Calculations of electron inelastic mean free paths. IX. Data for 41 elemental solids over the 50 eV to 30 keV range. *Surface and Interface Analysis* **43,** 689–713. eprint: https://onlinelibrary.wiley.com/doi/pdf/10.1002/sia.3522. https://onlinelibrary.wiley.com/doi/abs/10.1002/sia.3522 (2011).

64. Hüfner, S. *Photoelectron Spectroscopy* https://doi.org/10.1007/978-3-662-03209-1 (Springer Berlin Heidelberg, 1996).

65. Woodruff, D. P. & Bradshaw, A. M. Adsorbate structure determination on surfaces using photoelectron diffraction. *Reports on Progress in Physics* **57,** 1029. https://dx.doi.org/10.1088/0034-4885/57/10/003 (Oct. 1994).

66. Schönhense, G. *et al.* Momentum-transfer model of valence-band photoelectron diffraction. *Communications Physics* **3,** 45. ISSN: 2399-3650. https://doi.org/10.1038/s42005-020-0311-9 (Mar. 2020).

67. Pendry, J. B. The application of pseudopotentials to low-energy electron diffraction I. Calculation of the potential and 'inner potential'. *Journal of Physics C: Solid State Physics* **2,** 1215. https://dx.doi.org/10.1088/0022-3719/2/7/314 (July 1969).

68. Himpsel, F. J. & Eastman, D. E. Experimental energy dispersions for valence and conduction bands of palladium. *Phys. Rev. B* **18,** 5236–5239. https://link.aps.org/doi/10.1103/PhysRevB.18.5236 (10 Nov. 1978).

69. Hellmann, S., Ott, T., Kipp, L. & Rossnagel, K. Vacuum space-charge effects in nano-ARPES. *Phys. Rev. B* **85,** 075109. https://link.aps.org/doi/10.1103/PhysRevB.85.075109 (7 Feb. 2012).

70. Schönhense, B. *et al.* Multidimensional photoemission spectroscopy—the space-charge limit. *New Journal of Physics* **20,** 033004. https://dx.doi.org/10.1088/1367-2630/aaa262 (Mar. 2018).

71. Pietzsch, A. *et al.* Towards time resolved core level photoelectron spectroscopy with femtosecond x-ray free-electron lasers. *New Journal of Physics* **10,** 033004. https://dx.doi.org/10.1088/1367-2630/10/3/033004 (Mar. 2008).

72. Hellmann, S. *et al.* Time-resolved x-ray photoelectron spectroscopy at FLASH. *New Journal of Physics* **14,** 013062. https://dx.doi.org/10.1088/1367-2630/14/1/013062 (Jan. 2012).

73. Schönhense, G. *et al.* Suppression of the vacuum space-charge effect in fs-photoemission by a retarding electrostatic front lens. *Review of Scientific Instruments* **92,** 053703. eprint: https://doi.org/10.1063/5.0046567. https://doi.org/10.1063/5.0046567 (2021).

74. Schwinger, J. On the Classical Radiation of Accelerated Electrons. *Phys. Rev.* **75,** 1912–1925. https://link.aps.org/doi/10.1103/PhysRev.75.1912 (12 June 1949).

75. Wille, K. Synchrotron radiation sources. *Reports on Progress in Physics* **54,** 1005. https://dx.doi.org/10.1088/0034-4885/54/8/001 (Aug. 1991).

76. Schmüser, P., Dohlus, M. & Rossbach, J. *Ultraviolet and soft X-ray free-electron lasers: introduction to physical principles, experimental results, technological challenges* ISBN: 978-3-540-79572-8 (Springer Berlin, Heidelberg, 2008).

77. Ackermann, W. *et al.* Operation of a free-electron laser from the extreme ultraviolet to the water window. *Nature Photonics* **1,** 336–342. ISSN: 1749-4893. https://doi.org/10.1038/nphoton.2007.76 (June 2007).

78. Martins, M. *et al.* Monochromator beamline for FLASH. *Review of Scientific Instruments* **77,** 115108. eprint: https://doi.org/10.1063/1.2364148. https://doi.org/10.1063/1.2364148 (2006).

79. Gerasimova, N., Dziarzhytski, S. & Feldhaus, J. The monochromator beamline at FLASH: performance, capabilities and upgrade plans. *Journal of Modern Optics* **58,** 1480–1485. eprint: https://doi.org/10.1080/09500340.2011.588344. https://doi.org/10.1080/09500340.2011.588344 (2011).

80. Redlin, H. *et al.* The FLASH pump–probe laser system: Setup, characterization and optical beamlines. *Nuclear Instruments and Methods in Physics Research Section A: Accelerators, Spectrometers, Detectors and Associated Equipment* **635.** PhotonDiag 2010, S88–S93. ISSN: 0168-9002. https://www.sciencedirect.com/science/article/pii/S0168900210021935 (2011).

81. Seidel, M. *et al.* Ultrafast MHz-Rate Burst-Mode Pump–Probe Laser for the FLASH FEL Facility Based on Nonlinear Compression of ps-Level Pulses from an Yb-Amplifier Chain. *Laser & Photonics Reviews* **16,** 2100268. eprint: https://onlinelibrary.wiley.com/doi/pdf/10.1002/lpor.202100268. https://onlinelibrary.wiley.com/doi/abs/10.1002/lpor.202100268 (2022).

82. Dell'Angela, M., Parmigiani, F. & Malvestuto, M. Time resolved X-ray absorption spectroscopy in condensed matter: A road map to the future. *Journal of Electron Spectroscopy and Related Phenomena* **200.** Special Anniversary Issue: Volume 200, 22–30. ISSN: 0368-2048. https://www.sciencedirect.com/science/article/pii/S0368204815001449 (2015).

83. Seres, J. *et al.* Source of coherent kiloelectronvolt X-rays. *Nature* **433,** 596–596. ISSN: 1476-4687. https://doi.org/10.1038/433596a (Feb. 2005).

84. Krause, J. L., Schafer, K. J. & Kulander, K. C. Calculation of photoemission from atoms subject to intense laser fields. *Phys. Rev. A* **45,** 4998–5010. https://link.aps.org/doi/10.1103/PhysRevA.45.4998 (7 Apr. 1992).

85. Ferray, M. *et al.* Multiple-harmonic conversion of 1064 nm radiation in rare gases. *Journal of Physics B: Atomic, Molecular and Optical Physics* **21,** L31. https://dx.doi.org/10.1088/0953-4075/21/3/001 (Feb. 1988).

86. McPherson, A. *et al.* Studies of multiphoton production of vacuum-ultraviolet radiation in the rare gases. *J. Opt. Soc. Am. B* **4,** 595–601. https://opg.optica.org/josab/abstract.cfm?URI=josab-4-4-595 (Apr. 1987).

87. Krause, J. L., Schafer, K. J. & Kulander, K. C. High-order harmonic generation from atoms and ions in the high intensity regime. *Phys. Rev. Lett.* **68,** 3535–3538. https://link.aps.org/doi/10.1103/PhysRevLett.68.3535 (24 June 1992).

88. Corkum, P. B. Plasma perspective on strong field multiphoton ionization. *Phys. Rev. Lett.* **71,** 1994–1997. https://link.aps.org/doi/10.1103/PhysRevLett.71.1994 (13 Sept. 1993).

89. Lewenstein, M., Balcou, P., Ivanov, M. Y., L'Huillier, A. & Corkum, P. B. Theory of high-harmonic generation by low-frequency laser fields. *Phys. Rev. A* **49,** 2117–2132. https://link.aps.org/doi/10.1103/PhysRevA.49.2117 (3 Mar. 1994).

90. Zouros, T. & Benis, E. The hemispherical deflector analyser revisited. I. Motion in the ideal 1/r potential, generalized entry conditions, Kepler orbits and spectrometer basic equation. *Journal of Electron Spectroscopy and Related Phenomena* **125,** 221–248. ISSN: 0368-2048. https://www.sciencedirect.com/science/article/pii/S0368204802001378 (2002).

91. Oelsner, A. *et al.* Microspectroscopy and imaging using a delay line detector in time-of-flight photoemission microscopy. *Review of Scientific Instruments* **72,** 3968–3974. eprint: https://doi.org/10.1063/1.1405781. https://doi.org/10.1063/1.1405781 (2001).

92. Wenthaus, L. *Laser-Assisted Photoemission from Solids with Free Electron Lasers* ISBN: 978-3-8439-3803-7 (Verlag Dr. Hut, 2018).

93. *Momentoscope/HEXTOF-processor: Code for preprocessing data from the HEXTOF instrument at FLASH, DESY in Hamburg (DE)* 2018. https://github.com/momentoscope/hextof-processor.

94. Xian, R. P. *et al.* An open-source, end-to-end workflow for multidimensional photoemission spectroscopy. *Scientific Data* **7,** 442. ISSN: 2052-4463. https://doi.org/10.1038/s41597-020-00769-8 (Dec. 2020).

95. *Mpes-kit/mpes: Distributed data processing routines for multidimensional photoemission spectroscopy (MPES)* 2019. https://github.com/mpes-kit/mpes.

96. Xian, R. P., Rettig, L. & Ernstorfer, R. Symmetry-guided nonrigid registration: The case for distortion correction in multidimensional photoemission spectroscopy. *Ultramicroscopy* **202,** 133–139. ISSN: 0304-3991. https://www.sciencedirect.com/science/article/pii/S0304399118303474 (2019).

97. Landau, L. D. Zur Theorie der Phasenumwandlungen II. *Phys. Z. Sowjetunion* **11,** 26–35 (1937).

98. Wallace, P. R. The Band Theory of Graphite. *Phys. Rev.* **71,** 622–634. https://link.aps.org/doi/10.1103/PhysRev.71.622 (9 May 1947).

99. Slonczewski, J. C. & Weiss, P. R. Band Structure of Graphite. *Phys. Rev.* **109,** 272–279. https://link.aps.org/doi/10.1103/PhysRev.109.272 (2 Jan. 1958).

100. Novoselov, K. S. *et al.* Electric Field Effect in Atomically Thin Carbon Films. *Science* **306,** 666–669. eprint: https://www.science.org/doi/pdf/10.1126/science.1102896. https://www.science.org/doi/abs/10.1126/science.1102896 (2004).

101. Geim, A. K. & Novoselov, K. S. The rise of graphene. *Nature Materials* **6,** 183–191. ISSN: 1476-4660. https://doi.org/10.1038/nmat1849 (Mar. 2007).

102. Semenoff, G. W. Condensed-Matter Simulation of a Three-Dimensional Anomaly. *Phys. Rev. Lett.* **53,** 2449–2452. https://link.aps.org/doi/10.1103/PhysRevLett.53.2449 (26 Dec. 1984).

103. Castro Neto, A. H., Guinea, F., Peres, N. M. R., Novoselov, K. S. & Geim, A. K. The electronic properties of graphene. *Rev. Mod. Phys.* **81,** 109–162. https://link.aps.org/doi/10.1103/RevModPhys.81.109 (1 Jan. 2009).

104. Lamas, C. A., Cabra, D. C. & Grandi, N. Generalized Pomeranchuk instabilities in graphene. *Phys. Rev. B* **80,** 075108. https://link.aps.org/doi/10.1103/PhysRevB.80.075108 (7 Aug. 2009).

105. Land, T., Michely, T., Behm, R., Hemminger, J. & Comsa, G. STM investigation of single layer graphite structures produced on Pt(111) by hydrocarbon decomposition. *Surface Science* **264,** 261–270. ISSN: 0039-6028. https://www.sciencedirect.com/science/article/pii/0039602892901837 (1992).

106. Berger, C. *et al.* Electronic Confinement and Coherence in Patterned Epitaxial Graphene. *Science* **312,** 1191–1196. eprint: https://www.science.org/doi/pdf/10.1126/science.1125925. https://www.science.org/doi/abs/10.1126/science.1125925 (2006).

107. N'Diaye, A. T., Coraux, J., Plasa, T. N., Busse, C. & Michely, T. Structure of epitaxial graphene on Ir(111). *New Journal of Physics* **10,** 043033. https://doi.org/10.1088/1367-2630/10/4/043033 (Apr. 2008).

108. Heber, M. *et al.* Multispectral time-resolved energy–momentum microscopy using high-harmonic extreme ultraviolet radiation. *Review of Scientific Instruments* **93,** 083905. ISSN: 0034-6748. eprint: https://pubs.aip.org/aip/rsi/article-pdf/doi/10.1063/5.0091003/16615061/083905_1_online.pdf. https://doi.org/10.1063/5.0091003 (Aug. 2022).

109. Ulstrup, S., Johannsen, J. C., Grioni, M. & Hofmann, P. Extracting the temperature of hot carriers in time- and angle-resolved photoemission. *Review of Scientific Instruments* **85,** 013907. eprint: https://doi.org/10.1063/1.4863322. https://doi.org/10.1063/1.4863322 (2014).

110. Kralj, M. *et al.* Graphene on Ir(111) characterized by angle-resolved photoemission. *Phys. Rev. B* **84,** 075427. https://link.aps.org/doi/10.1103/PhysRevB.84.075427 (7 Aug. 2011).

111. Johannsen, J. C. *et al.* Electron–phonon coupling in quasi-free-standing graphene. *Journal of Physics: Condensed Matter* **25,** 094001. https://doi.org/10.1088/0953-8984/25/9/094001 (Feb. 2013).

112. Elmers, H. J. *et al.* Hosting of surface states in spin–orbit induced projected bulk band gaps of W(1 1 0) and Ir(1 1 1). *Journal of Physics: Condensed Matter* **29,** 255001. https://doi.org/10.1088/1361-648x/aa7173 (May 2017).

113. Hasan, M. Z. & Kane, C. L. Colloquium: Topological insulators. *Rev. Mod. Phys.* **82,** 3045–3067. https://link.aps.org/doi/10.1103/RevModPhys.82.3045 (4 Nov. 2010).

114. Hasan, M. Z. & Moore, J. E. Three-Dimensional Topological Insulators. *Annual Review of Condensed Matter Physics* **2,** 55–78. eprint: https://doi.org/10.1146/annurev-conmatphys-062910-140432. https://doi.org/10.1146/annurev-conmatphys-062910-140432 (2011).

115. Bansil, A., Lin, H. & Das, T. Colloquium: Topological band theory. *Rev. Mod. Phys.* **88,** 021004. https://link.aps.org/doi/10.1103/RevModPhys.88.021004 (2 June 2016).

116. Das Sarma, S., Freedman, M. & Nayak, C. Topologically Protected Qubits from a Possible Non-Abelian Fractional Quantum Hall State. *Phys. Rev. Lett.* **94,** 166802. https://link.aps.org/doi/10.1103/PhysRevLett.94.166802 (16 Apr. 2005).

117. Nayak, C., Simon, S. H., Stern, A., Freedman, M. & Das Sarma, S. Non-Abelian anyons and topological quantum computation. *Rev. Mod. Phys.* **80,** 1083–1159. https://link.aps.org/doi/10.1103/RevModPhys.80.1083 (3 Sept. 2008).

118. Kane, C. L. & Mele, E. J. Z_2 Topological Order and the Quantum Spin Hall Effect. *Phys. Rev. Lett.* **95,** 146802. https://link.aps.org/doi/10.1103/PhysRevLett.95.146802 (14 Sept. 2005).

119. Fu, L., Kane, C. L. & Mele, E. J. Topological Insulators in Three Dimensions. *Phys. Rev. Lett.* **98,** 106803. https://link.aps.org/doi/10.1103/PhysRevLett.98.106803 (10 Mar. 2007).

120. Hsieh, D. *et al.* A tunable topological insulator in the spin helical Dirac transport regime. *Nature* **460,** 1101–1105. ISSN: 1476-4687. https://doi.org/10.1038/nature08234 (Aug. 2009).

121. Zhu, Z., Cheng, Y. & Schwingenschlögl, U. Band inversion mechanism in topological insulators: A guideline for materials design. *Phys. Rev. B* **85,** 235401. https://link.aps.org/doi/10.1103/PhysRevB.85.235401 (23 June 2012).

122. Xia, Y. *et al.* Observation of a large-gap topological-insulator class with a single Dirac cone on the surface. *Nature Physics* **5,** 398–402. ISSN: 1745-2481. https://doi.org/10.1038/nphys1274 (June 2009).

123. Zhang, H. *et al.* Topological insulators in Bi_2Se_3, Bi_2Te_3 and Sb_2Te_3 with a single Dirac cone on the surface. *Nature Physics* **5,** 438–442. ISSN: 1745-2481. https://doi.org/10.1038/nphys1270 (June 2009).

124. Moore, J. E. & Balents, L. Topological invariants of time-reversal-invariant band structures. *Phys. Rev. B* **75,** 121306. https://link.aps.org/doi/10.1103/PhysRevB.75.121306 (12 Mar. 2007).

125. Roy, R. Topological phases and the quantum spin Hall effect in three dimensions. *Phys. Rev. B* **79,** 195322. https://link.aps.org/doi/10.1103/PhysRevB.79.195322 (19 May 2009).

126. Kastl, C., Karnetzky, C., Karl, H. & Holleitner, A. W. Ultrafast helicity control of surface currents in topological insulators with near-unity fidelity. *Nature Communications* **6,** 6617. ISSN: 2041-1723. https://doi.org/10.1038/ncomms7617 (Mar. 2015).

127. Tian, J., Şahin, C., Miotkowski, I., Flatté, M. E. & Chen, Y. P. Opposite current-induced spin polarizations in bulk-metallic Bi_2Se_3 and bulk-insulating Bi_2Te_2Se topological insulator thin flakes. *Phys. Rev. B* **103,** 035412. https://link.aps.org/doi/10.1103/PhysRevB.103.035412 (3 Jan. 2021).

128. Cheng, L. *et al.* Temperature-dependent ultrafast carrier and phonon dynamics of topological insulator $Bi_{1.5}Sb_{0.5}Te_{1.8}Se_{1.2}$. *Applied Physics Letters* **104,** 211906. eprint: https://doi.org/10.1063/1.4879831. https://doi.org/10.1063/1.4879831 (2014).

129. McIver, J. W., Hsieh, D., Steinberg, H., Jarillo-Herrero, P. & Gedik, N. Control over topological insulator photocurrents with light polarization. *Nature Nanotechnology* **7,** 96–100. ISSN: 1748-3395. https://doi.org/10.1038/nnano.2011.214 (Feb. 2012).

130. Kuroda, K., Reimann, J., Güdde, J. & Höfer, U. Generation of Transient Photocurrents in the Topological Surface State of Sb_2Te_3 by Direct Optical Excitation with Midinfrared Pulses. *Phys. Rev. Lett.* **116,** 076801. https://link.aps.org/doi/10.1103/PhysRevLett.116.076801 (7 Feb. 2016).

131. Sobota, J. A. *et al.* Distinguishing Bulk and Surface Electron-Phonon Coupling in the Topological Insulator Bi_2Se_3 Using Time-Resolved Photoemission Spectroscopy. *Phys. Rev. Lett.* **113,** 157401. https://link.aps.org/doi/10.1103/PhysRevLett.113.157401 (15 Oct. 2014).

132. Glinka, Y. D., Babakiray, S., Johnson, T. A., Holcomb, M. B. & Lederman, D. Effect of carrier recombination on ultrafast carrier dynamics in thin films of the topological insulator Bi_2Se_3. *Applied Physics Letters* **105,** 171905. eprint: https://doi.org/10.1063/1.4901052. https://doi.org/10.1063/1.4901052 (2014).

133. Hatch, R. C. *et al.* Stability of the Bi_2Se_3(111) topological state: Electron-phonon and electron-defect scattering. *Phys. Rev. B* **83,** 241303. https://link.aps.org/doi/10.1103/PhysRevB.83.241303 (24 June 2011).

134. Queiroz, R. *et al.* Sputtering-induced reemergence of the topological surface state in Bi_2Se_3. *Phys. Rev. B* **93,** 165409. https://link.aps.org/doi/10.1103/PhysRevB.93.165409 (16 Apr. 2016).

135. Edmonds, M. T. *et al.* Air-Stable Electron Depletion of Bi_2Se_3 Using Molybdenum Trioxide into the Topological Regime. *ACS Nano* **8.** PMID: 24911767, 6400–6406. eprint: https://doi.org/10.1021/nn502031k. https://doi.org/10.1021/nn502031k (2014).

136. Fang, M. *et al.* Layer-dependent dielectric permittivity of topological insulator Bi_2Se_3 thin films. *Applied Surface Science* **509,** 144822. ISSN: 0169-4332. https://www.sciencedirect.com/science/article/pii/S0169433219336396 (2020).

137. Polyanskiy, M. N. *Refractive index database* https://refractiveindex.info/?shelf=main&book=Bi2Se3&page=Fang-10L. Accessed on 2022-03-30. 2022.

138. Hoffmann, S., Søndergaard, C., Schultz, C., Li, Z. & Hofmann, P. An undulator-based spherical grating monochromator beamline for angle-resolved photoemission spectroscopy. *Nuclear Instruments and Methods in Physics Research Section A: Accelerators, Spectrometers, Detectors and Associated Equipment* **523,** 441–453. ISSN: 0168-9002. https://www.sciencedirect.com/science/article/pii/S0168900204000695 (2004).

139. Luo, C. W. *et al.* Snapshots of Dirac Fermions near the Dirac Point in Topological Insulators. *Nano Letters* **13.** PMID: 24228733, 5797–5802. eprint: https://doi.org/10.1021/nl4021842. https://doi.org/10.1021/nl4021842 (2013).

140. Curcio, D. *et al.* Tracking the surface atomic motion in a coherent phonon oscillation. *Phys. Rev. B* **106,** L201409. https://link.aps.org/doi/10.1103/PhysRevB.106.L201409 (20 Nov. 2022).

141. Landau, L. On the theory of the Fermi liquid. *Sov. Phys. JETP* **8,** 70 (1959).

142. Dzero, M., Sun, K., Galitski, V. & Coleman, P. Topological Kondo Insulators. *Phys. Rev. Lett.* **104,** 106408. http://link.aps.org/doi/10.1103/PhysRevLett.104.106408 (2013) (Mar. 2010).

143. Laurita, N. J. *et al.* Anomalous three-dimensional bulk ac conduction within the Kondo gap of ${\mathrm{SmB}}_{6}$ single crystals. *Phys. Rev. B* **94.** Publisher: American Physical Society, 165154. https://link.aps.org/doi/10.1103/PhysRevB.94.165154 (2021) (Oct. 2016).

144. Schrieffer, J. R. & Wolff, P. A. Relation between the Anderson and Kondo Hamiltonians. *Phys. Rev.* **149,** 491–492. https://link.aps.org/doi/10.1103/PhysRev.149.491 (2 Sept. 1966).

145. Coleman, P. *Heavy Fermions and the Kondo Lattice: a 21st Century Perspective* 2015. arXiv: 1509.05769 [cond-mat.str-el].

146. Haldane, F. D. M. New model for the mixed-valence phenomenon in rare-earth materials. *Phys. Rev. B* **15,** 2477–2484. https://link.aps.org/doi/10.1103/PhysRevB.15.2477 (5 Mar. 1977).

147. Hewson, A. C. *The Kondo Problem to Heavy Fermions* (Cambridge University Press, 1993).

148. Kondo, J. Resistance Minimum in Dilute Magnetic Alloys. *Progress of Theoretical Physics* **32,** 37–49. ISSN: 0033-068X. eprint: https://academic.oup.com/ptp/article-pdf/32/1/37/5193092/32-1-37.pdf. https://doi.org/10.1143/PTP.32.37 (July 1964).

149. Knapp, G. S. & Sarachik, M. P. Resistivity and Susceptibility of Rh–Ru Alloys Containing Fe. *Journal of Applied Physics* **40,** 1474–1475. ISSN: 0021-8979. eprint: https://pubs.aip.org/aip/jap/article-pdf/40/3/1474/10557949/1474_1_online.pdf. https://doi.org/10.1063/1.1657727 (Mar. 1969).

150. Gerken, F. Calculated photoemission spectra of the 4f states in the rare-earth metals. *Journal of Physics F: Metal Physics* **13,** 703. https://dx.doi.org/10.1088/0305-4608/13/3/021 (Mar. 1983).

151. Coleman, P. *Introduction to Many-Body Physics* (Cambridge University Press, 2015).

152. Lawrence, J. M., Riseborough, P. S. & Parks, R. D. Valence fluctuation phenomena. *Reports on Progress in Physics* **44,** 1. https://dx.doi.org/10.1088/0034-4885/44/1/001 (Jan. 1981).

153. Neuenschwander, J. & Wachter, P. A high pressure low temperature study on rare earth compounds: Semiconductor to metal transition. *Physica B: Condensed Matter* **160,** 231–270. ISSN: 0921-4526. https://www.sciencedirect.com/science/article/pii/092145269090327Q (1989).

154. Varma, C. M. Mixed-valence compounds. *Rev. Mod. Phys.* **48,** 219–238. https://link.aps.org/doi/10.1103/RevModPhys.48.219 (2 Apr. 1976).

155. Campagna, M., Bucher, E., Wertheim, G. K., Buchanan, D. N. E. & Longinotti, L. D. Spontaneous Interconfiguration Fluctuations in the Tm Monochalcogenides. *Phys. Rev. Lett.* **32,** 885–889. https://link.aps.org/doi/10.1103/PhysRevLett.32.885 (16 Apr. 1974).

156. Wertheim, G. K., Eib, W., Kaldis, E. & Campagna, M. Mixed valency of TmSe. *Phys. Rev. B* **22,** 6240–6246. https://link.aps.org/doi/10.1103/PhysRevB.22.6240 (12 Dec. 1980).

157. Wachter, P., Kamba, S. & Grioni, M. Empty 4f states in TmS. *Physica B: Condensed Matter* **252,** 178–185. ISSN: 0921-4526. https://www.sciencedirect.com/science/article/pii/S0921452698000544 (1998).

158. Batlogg, B., Ott, H. R., Kaldis, E., Thöni, W. & Wachter, P. Magnetic mixed valent TmSe. *Phys. Rev. B* **19,** 247–259. https://link.aps.org/doi/10.1103/PhysRevB.19.247 (1 Jan. 1979).

159. Oh, S.-J. & Allen, J. W. Inverse photoemission of mixed-valence compounds and $4f$ inner-well stability. *Phys. Rev. B* **29,** 589–592. https://link.aps.org/doi/10.1103/PhysRevB.29.589 (2 Jan. 1984).

160. Ward, R., Clayman, B. & Rice, T. Far-infrared reflectivity of the mixed-valence compounds TmTe and TmSe. *Solid State Communications* **17,** 1297–1300. ISSN: 0038-1098. https://www.sciencedirect.com/science/article/pii/0038109875906900 (1975).

161. Møller, H. B., Shapiro, S. M. & Birgeneau, R. J. Field-Dependent Magnetic Phase Transitions in Mixed-Valent TmSe. *Phys. Rev. Lett.* **39,** 1021–1025. https://link.aps.org/doi/10.1103/PhysRevLett.39.1021 (16 Oct. 1977).

162. Boppart, H. The semiconductor-metal transition in Tm-compounds. *Journal of Magnetism and Magnetic Materials* **47-48,** 436–442. ISSN: 0304-8853. https://www.sciencedirect.com/science/article/pii/0304885385904597 (1985).

163. Link, P., Goncharenko, I., Mignot, J., Matsumura, T. & Suzuki, T. Ferromagnetic mixed-valence and kondo-lattice state in TmTe at high pressure. *Physical review letters* **80,** 173 (1998).

164. Tsiok, O. B., Khvostantsev, L. G., Golubkov, A. V., Smirnov, I. A. & Brazhkin, V. V. General behavior of chalcogenides of rare-earth metals in transition to the intermediate valence state under high pressures. *Phys. Rev. B* **90,** 165141. https://link.aps.org/doi/10.1103/PhysRevB.90.165141 (16 Oct. 2014).

165. Derr, J. *et al.* Valence and magnetic ordering in intermediate valence compounds: TmSe versus SmB6. *Journal of Physics: Condensed Matter* **18,** 2089. https://dx.doi.org/10.1088/0953-8984/18/6/021 (Jan. 2006).

166. Yeh, J. & Lindau, I. Atomic subshell photoionization cross sections and asymmetry parameters: $1 \leq Z \leq 103$. *Atomic Data and Nuclear Data Tables* **32,** 1–155. ISSN: 0092-640X. https://www.sciencedirect.com/science/article/pii/0092640X85900166 (1985).

167. Min, C.-H. *et al.* Importance of Charge Fluctuations for the Topological Phase in SmB_6. *Phys. Rev. Lett.* **112,** 226402. https://link.aps.org/doi/10.1103/PhysRevLett.112.226402 (22 June 2014).

168. Lutz, P. *et al.* Valence characterisation of the subsurface region in. *Philosophical Magazine* **96,** 3307–3321. eprint: https://doi.org/10.1080/14786435.2016.1192724. https://doi.org/10.1080/14786435.2016.1192724 (2016).

169. Furrer, A., Bührer, W. & Wachter, P. A comparison of the dynamical susceptibility of trivalent and intermediate valent TmSe studied by inelastic neutron scattering. *Solid State Communications* **40,** 1011–1014. ISSN: 0038-1098. https://www.sciencedirect.com/science/article/pii/0038109881900569 (1981).

170. Higuchi, M. *et al.* Growth of RE:LuVO4 (RE=Nd, Tm, Yb) single crystals by the floating zone method and their spectroscopic properties. *Journal of Crystal Growth* **283,** 100–107. ISSN: 0022-0248. https://www.sciencedirect.com/science/article/pii/S0022024805006469 (2005).

171. Leuenberger, D. *et al.* Dehybridization of f and d states in the heavy-fermion system $YbRh_2Si_2$. *Phys. Rev. B* **97,** 165108. https://link.aps.org/doi/10.1103/PhysRevB.97.165108 (16 Apr. 2018).

172. Sterzi, A. *et al.* SmB_6 electron-phonon coupling constant from time- and angle-resolved photoelectron spectroscopy. *Phys. Rev. B* **94,** 081111. https://link.aps.org/doi/10.1103/PhysRevB.94.081111 (8 Aug. 2016).

173. Ishida, Y. *et al.* Emergent photovoltage on SmB6 surface upon bulk-gap evolution revealed by pump-and-probe photoemission spectroscopy. *Scientific Reports* **5,** 8160. ISSN: 2045-2322. https://doi.org/10.1038/srep08160 (Feb. 2015).

174. Andres, B., Lee, S. E. & Weinelt, M. The role of spin-lattice coupling for ultrafast changes of the magnetic order in rare earth metals. *Applied Physics Letters* **119,** 182404. ISSN: 0003-6951. eprint: https://pubs.aip.org/aip/apl/article-pdf/doi/10.1063/5.0067397/13762460/182404_1_online.pdf. https://doi.org/10.1063/5.0067397 (Nov. 2021).

175. Wietstruk, M. *et al.* Hot-Electron-Driven Enhancement of Spin-Lattice Coupling in Gd and Tb 4f Ferromagnets Observed by Femtosecond X-Ray Magnetic Circular Dichroism. *Phys. Rev. Lett.* **106,** 127401. https://link.aps.org/doi/10.1103/PhysRevLett.106.127401 (12 Mar. 2011).

176. López-Flores, V. *et al.* Role of critical spin fluctuations in ultrafast demagnetization of transition-metal rare-earth alloys. *Phys. Rev. B* **87,** 214412. https://link.aps.org/doi/10.1103/PhysRevB.87.214412 (21 June 2013).

177. Dendzik, M. *et al.* Observation of an Excitonic Mott Transition through Ultrafast Core-cum-Conduction Photoemission Spectroscopy. *Phys. Rev. Lett.* **125,** 096401. https://link.aps.org/doi/10.1103/PhysRevLett.125.096401 (9 Aug. 2020).

178. Curcio, D. *et al.* Ultrafast electronic linewidth broadening in the C 1s core level of graphene. *Phys. Rev. B* **104,** L161104. https://link.aps.org/doi/10.1103/PhysRevB.104.L161104 (16 Oct. 2021).

179. Pressacco, F. *et al.* Subpicosecond metamagnetic phase transition in FeRh driven by non-equilibrium electron dynamics. *Nature Communications* **12,** 5088. ISSN: 2041-1723. https://doi.org/10.1038/s41467-021-25347-3 (2021).

180. Baumgärtner, K. *et al.* Ultrafast orbital tomography of a pentacene film using time-resolved momentum microscopy at a FEL. *Nature Communications* **13,** 2741. ISSN: 2041-1723. https://doi.org/10.1038/s41467-022-30404-6 (May 2022).